Universidade do Minho
Escola de Engenharia

Cristiana Filipa Almeida Alves

Development of bioactive surfaces
for bone ingrowth on dental implants

Development of bioactive surfaces
for bone ingrowth on dental implants

Cristiana Filipa Almeida Alves

UMinho | 2018

janeiro de 2018

Universidade do Minho
Escola de Engenharia

Cristiana Filipa Almeida Alves

Development of bioactive surfaces
for bone ingrowth on dental implants

Tese de Doutoramento
Programa Doutoral em Engenharia de Materiais

Trabalho efetuado sob a orientação da
Professora Doutora Sandra Maria Fernandes Carvalho

STATEMENT OF INTEGRITY

I hereby declare having conducted my thesis with integrity. I confirm that I have not used plagiarism or any form of falsification of results in the process of the thesis elaboration.

I further declare that I have fully acknowledged the Code of Ethical Conduct of the University of Minho.

University of Minho, January 2018

Full name: Cristiana Filipa Almeida Alves

Signature: _Cristiana Filipa Almeida Alves_

Ao pai João, à mãe Glória, aos sobrinhos João e Gabriel

e ao namorado Adriano, que ao seu jeito possibilitaram que eu chegasse até aqui.

"Em todas as dificuldades, existe uma oportunidade."

Albert Einstein

Acknowledgements

A concretização de um doutoramento não é um processo solitário e como tal não seria possível sem a colaboração e trabalho de equipa entre várias pessoas e instituições às quais manifesto o meu profundo e sincero agradecimento.

Em primeiro lugar quero agradecer à minha orientadora, Professora Sandra Carvalho, não só pelo doutoramento, mas pelos últimos 6 anos de colaboração. Um enorme obrigada por ter acreditado em mim, pela oportunidade de realizar este trabalho, pela liberdade que me confiou, pelas discussões cientificas (e não só ☺), como também pelos sábios conselhos e conhecimento científico transmitido. Agradeço todas as oportunidades que me permitiram crescer enquanto investigadora, a coragem que continua a transmitir para eu evoluir, a paciência e acima de tudo a amizade. Obrigada, obrigada, obrigada!

Ao Professor Albano Cavaleiro do Departamento de Engenharia Mecânica da Universidade de Coimbra, pelo qual manifesto enorme admiração, quero agradecer a disponibilidade e paciência inesgotáveis em todas as horas de discussão cientifica, pela sabedoria e conhecimento cientifico transmitido e por me ter acolhido no SEG-CEMMPRE.

Quero agradecer ao Professor Luís Silvino Marques do Departamento de Física da Universidade do Minho pelos conhecimentos transmitidos e pela ajuda no desenvolvimento das simulações computacionais, bem como pela disponibilidade e paciência na discussão de resultados que se revelaram decisivos no aprofundamento deste trabalho.

Especial agradecimento ao Professor Paulo Ferreira, Diretor do Departamento de Microscopia do Laboratório Ibério Internacional – INL, pela oportunidade de realizar análises de microscopia eletrónica de varrimento e transmissão facilitando o acesso aos equipamentos disponíveis no INL, como também quero agradecer os conhecimentos científicos transmitidos que se revelaram fundamentais na minha evolução cientifica. Quero agradecer ao Doutor Henrique Carbo pelo treinamento e disponibilidade sempre que alguma duvida surgiu.

Ao Professor Luís Pereira do Departamento de Ciência de Materiais da Faculdade de Ciências e Tecnologia da Universidade Nova de Lisboa agradeço por me ter acolhido no

Por último, quero testemunhar o profundo reconhecimento e gratidão para com as pessoas mais importantes da minha vida. Ao pai João pelas conversas e conselhos, pelas muitas madrugadas que cedeste ao meu serviço uber particular. À mãe Glória por me mostrares que é nos momentos mais difíceis da vida que nos redescobrimos e tornamos mais fortes. Aos sobrinhos João Maria e Gabriel pela inocência e tranquilidade que me envolveram nas vossas brincadeiras. Ao namorado Adriano pela paciência e apoio em todas as horas que o bom senso faltou, por me teres ouvido e encorajado, por teres estado sempre presente. Foi contigo que recuperei as minhas forças e a vontade firme de continuar. Aos irmãos Virgínia e João por me ajudarem a ir sempre mais além. Para vós todas as palavras deste mundo não chegariam e como tal resta-me dizer-vos: muito obrigada!

Cristiana Filipa Almeida Alves

Abstract

Dental implants are usually fabricated in titanium (Ti) based materials due to its biocompatibility and good corrosion resistance. However, the low ability to form a strong chemical bond with living tissue, known as bioactivity, is one of the drawbacks of Ti dental implants. Consequently, the use of dental implants is sometimes accompanied by failure due to periimplantitis disease and, subsequently, poor aesthetics when soft-hard tissue margin recedes. On this context, further research is needed for developing new bioactive surfaces able to enhance the osseous growth. Tantalum (Ta) and Ta oxide coatings have been proven to be bioactive materials due to their high wettability and high surface free energy. Therefore, they were recently proposed to enhance the osseointegration and the performance of medical devices, such as dental implants. On the other hand, surface nanostructuring can also play a fundamental role in bone ingrowth since it enhances surface-protein interactions, bioactivity and osteoblast adhesion. The development of highly bioactive surfaces, with enhanced osseointegration and corrosion resistance, can then be achieved through either the deposition of Ta-based coatings by magnetron sputtering or nanopatterning bulk Ta by anodization.

In a first part of this work $Ta_{1-x}O_x$ coatings were deposited by DC magnetron sputtering in an $Ar+O_2$ atmosphere onto SS 316L to study the importance of the oxygen in the bioactivity performance. In a second part, the synergetic effect of anodic TaO_x with surface nanostructuring was analyzed by electrochemical anodization of Ta plates.

Regarding the coatings developed by magnetron sputtering, structural results show that a small increase of oxygen content leads to a change of Ta from the stable bcc phase (α-Ta) to a mixture of nanocrystalline phases. For large amounts of oxygen, oxide phases could be achieved. The combination of the structural and mechanical experimental results with *ab-initio DFT* calculations shows that the increasing addition of oxygen to the Ta phase leads to a decrease of the density and improvement of the elastic properties of the crystal structures. Additionally, a more corrosion protective behavior of the coatings is observed as the oxygen amount increases in the films. Nevertheless, independently of the film composition, higher pitting inhibition in the coated stainless steel is achieved,

allowing, globally, to match the performance of the market reference, the CP Ti Gr2 material.

The development of nanostructured oxide surfaces on bulk Ta, through an anodization process, reveals the formation of a dimple-shaped surface morphology, with an oxide thickness around 5 nm, by using an electrolyte composed by H_2SO_4 and HF and treatment conditions of 15-50 V potential range and runtimes between 5 and 120 s.

Bioactivity evaluation of $Ta_{1-x}O_x$ samples developed by magnetron sputtering show better ability to change and adsorb ions of SBF of these surfaces, comparatively to the commercial control CP Ti Gr2, and an increased affinity for apatite adhesion with higher apatite content formation, which proves that the bioactivity kinetics of $Ta_{1-x}O_x$ surfaces is faster than that of Ti surface favoring a faster osseointegration.

Cristiana Filipa Almeida Alves

Resumo

Atualmente os implantes dentários são produzidos em materiais à base de titânio (Ti) devido à sua biocompatibilidade e boa resistência à corrosão. No entanto, a reduzida capacidade para formar uma ligação química forte com o tecido vivo, conhecida como bioatividade, é uma das maiores limitações dos implantes de Ti. Consequentemente, o uso de implantes dentários algumas vezes induz o aparecimento da doença peri-implantar, que provoca uma regressão no crescimento ósseo, culminando na falha do implante. Neste contexto, é necessário desenvolver novas superfícies que sejam bioativas de modo a exponenciar o crescimento ósseo. Revestimentos de tântalo (Ta) e óxido de Ta têm provado ser materiais bioativos devido à sua elevada molhabilidade e energia livre de superfície. Consequentemente, têm sido propostos para melhorar a osteointegração e o desempenho de dispositivos médicos, tal como implantes dentários. Por outro lado, a nanoestruturação de superfícies também pode desempenhar um papel fundamental no crescimento ósseo visto que exponencia: a interação entre a superfície a as proteínas; a bioatividade; e a adesão de células osteoblásticas. O desenvolvimento de superfícies bioativas, que promovam a osteointegração e tenham boa resistência à corrosão, pode ser alcançado quer pela deposição de revestimentos à base de Ta através de pulverização catódica, quer pela nanoestruturação de Ta através de anodização.

Numa primeira fase deste trabalho foram depositados revestimentos de $Ta_{1-x}O_x$ através de pulverização catódica, numa atmosfera de $Ar + O_2$, depositados sobre SS 316L de forma a estudar a importância do oxigénio na bioatividade. Numa segunda fase, o efeito sinergético de TaO_x anódico com a superfície nanoestruturada foi analisado através da anodização de uma chapa de Ta.

Tendo em conta os revestimentos desenvolvidos por pulverização catódica, a análise estrutural mostra que um pequeno aumento no teor de oxigénio induz a mudança de fases de Ta desde a fase ccc (α-Ta) até uma mistura de fases nanocristalinas. As fases de óxido de Ta são alcançadas com teores elevados de oxigénio. A combinação dos resultados experimentais de estrutura e propriedades mecânicas com simulações *ab-initio* demonstraram que o aumento do teor de oxigénio na fase de Ta induz a diminuição da densidade e o aumento das propriedades elásticas das estruturas cristalinas.

Adicionalmente, com o aumento do teor de oxigénio nos filmes, verificou-se um aumento da proteção à corrosão. Não obstante, foi possível inibir a corrosão por picadas do aço inoxidável independentemente da composição do revestimento, permitindo, de um modo geral, superiorizar o desempenho da referência do mercado, o Ti CP Gr2.

O desenvolvimento de uma superfície oxidada e nanoestruturada numa chapa de Ta, através do processo de anodização, revela a formação de uma topográfica com concavidades, cuja espessura do óxido é aproximadamente 5 nm. Estes resultados são alcançados usando um eletrólito de anodização composto por H_2SO_4 e HF, com potenciais entre 15-50 V, durante 5 a 120 s.

Os testes de bioatividade das amostras $Ta_{1-x}O_x$ depositadas por pulverização catódica revelaram a sua maior habilidade para trocar e adsorver iões do SBF, comparativamente ao controlo comercial, Ti CP Gr2, e uma melhor afinidade para adsorver fosfatos de cálcio com uma formação de apatite superior. Estes resultados provam que as superfícies de $Ta_{1-x}O_x$ têm uma cinética de bioatividade mais rápida do que o Ti, o que por sua vez, favorece a osteointegração.

Table of Contents

List of figures

Cristiana Filipa Almeida Alves

List of tables

Cristiana Filipa Almeida Alves

List of Abbreviations

AC: Alternate Current

at.: atomic

AFM: Atomic Force Microscope

AISI: American Iron and Steel Institute

ASTM: American Society for Testing and Materials

bcc: Body Centered Cubic

BEMA: Bruggemann Effective Model Approximation

CVD: Chemical Vapor Deposition

DC: Direct Current

DFT: Density Functional Theory

E: Elastic modulus

EC: Equivalent Circuit

EBSD: Electron Backscatter Diffraction

EDS: Energy Dispersive X-ray

EIS: Electrochemical Impedance Spectroscopy

EPMA: Electron Probe Micro-Analysis

fcc: Face Centered Cubic

FIB: Focused Ion Beam

FTIR: Fourier Transform Infrared

GL: Gaussian-Lorentzian

HAADF: High-Angle Annular Dark-Field

hFOB: human Fetal Osteoblast

HUVEC: Human Umbilical Vein Endothelial Cells

ISO: International Organization for Standardization

LENS: Laser Engineered Net Shaping

MS: Magnetron Sputtering

OCP: Open Circuit Potential

PVD: Physical Vapor Deposition

RSF: Relative Sensitive Factors

SAW: Surface Acoustic Waves

SBF: Simulated Body Fluid

SCE: Saturated Calomel Electrode

SE: Spectroscopic Ellipsometry

SEEY: Secondary Electron Emission Yield

SEM: Scanning Electron Microscope

SS: Stainless Steel

STEM: Scanning Transmission Electron Microscope

TEM: Transmission Electron Microscope

TL: Tauc-Lorentz

vol.: volume

XRD: X-ray Diffraction

XPS: X-ray Photoelectron Spectroscopy

WDS: Wave Dispersive X-ray

Introduction

The number of dental implants procedures has increased worldwide. According to "***Global Market Study on Dental Implants - Asia Pacific to Witness Fastest Growth by 2020***" published by <u>Persistence Market Research</u>, Europe, the global market of dental implants was evaluated at $ 4 508.9 million in 2014 and is expected to grow at a Compound Annual Growth Rate (CAGR) of 9.7% from 2014 until 2020, reaching an estimated value of $ 7 879.5 million in 2020. Nowadays, dental implants are produced using titanium (Ti) based materials due to its biocompatibility and corrosion resistance [1-6]. However, Ti-based surfaces do not show ability to stimulate the formation of new apatite containing tissue [7] and then, delays the biological integration. Subsequently, the slow osseointegration of Ti dental implants leads to slow loading of the implant by the artificial crown, thus requiring a long non-operational time [7, 8], which increases the probability of microorganisms entrance on the oral environment near to the surgical site. The adhesion and possible microbial colonization may induce the appearance of infections with consequent post-surgical complications [9, 10]. Indeed, the microbial colonization can lead to the regression of soft-hard tissue or peri-implantitis disease with consequent implant removal and debridement combined with an extended duration of treatment and its medical costs [9]. The number of dental implants failures associated to the healing process (osseointegration) is around 47% before artificial crown implantation and 45% during the first year of use [11]. Thus, development of highly bioactive surfaces able to enhance and promote the osseous growth and bone matrix mineralization and then, reduce the frequency of infective complications, is a major challenge to manufacturers and research community worldwide.

Tantalum (Ta) has been considered a good alternative since it is bioactive and presents interesting wettability and surface free energy, which promotes osseointegration and good corrosion resistance [12-15]. Furthermore, the higher surface free energy of

tantalum oxides (TaO$_x$) stimulates the regeneration process in living tissues and thus, increases the osseointegration efficiency [12, 16-18]. Moreover, TaO$_x$ enhances the corrosion resistance due to its high chemical stability [19-21]. In fact, TaO$_x$ surfaces play an important role in the interface between the bone and the implant since TaO$_x$ (mostly the native oxide, tantalum pentoxide - Ta$_2$O$_5$) promotes biomineralization due to its ability to bind with calcium, enhancing bone ingrowth [12]. Undoubtedly, the bioactivity can be controlled by the surface's chemical composition, which determines the type of ions adsorbed on the dental implant surface.

Moreover, another approach related with nano porosities has been gained a lot of attention in the last decades. Considering that the cellular response is assigned to have a compromise with nanostructures due to the biomimetization of bone tissue, it is reported by the literature [22, 23] that surface profiles in nanometer scale enhance the surface-protein interaction. Consequently, the osteoblast adhesion and differentiation is improved, which plays a fundamental role in the bone ingrowth. In short, the nanotopography allows to manipulate the stem cells differentiation in osteoblastic cells that will be determinant to reach a desired osseointegration.

On this concern, this work arises with a new approach. We propose the development of a novel bioactive and osseointegrated surface based on the synergetic effect of an oxide and a nanostructured surface of Ta-based materials.

1.1. Work objectives, methodology and thesis organization

This report is focused on the production and characterization of a novel Ta-based surface. A surface with multifunctional properties able to overcome the bioactivity and osseointegration failures of the dental implants used nowadays will be achieved by two main approaches:

   (i) development of bioactive surfaces through the deposition by magnetron sputtering of Ta-based coatings;

(ii) development of a bioactive and a nanostructured surface through nanopatterning at bulk Ta using anodization process.

In both cases, the surface modification is proposed for enhancing functionalities in terms of bioactivity, osseointegration and corrosion of dental implants. Either the magnetron sputtering deposition or anodization process allow the achievement of a bioactive TaO_x surface. Moreover, anodization method also allows the formation of nanostructures. The nanostructured surface further promotes the interaction between the implant surface and the cells from adjacent tissues and then, enhancing the secondary stabilization (osseointegration). This thesis presents a discussion on the importance of developing such new surface modification to improve materials used in dental implants.

Specifically, the contribution of this project for the state of the art will be:

- An extensive study of the influence of Ta-based coatings deposition conditions on the structure, chemical bonding and morphology with the increase of oxygen content.

- Understand the relationships between anodization conditions such as, the electrolyte concentration, the potential and the time, in the size, shape and distribution of the nanostructures formed on Ta surface;

- Analysis of the surface composition and/or nanostructures influence on the *in-vitro* bone-bonding ability in order to achieve an optimized Ta-based surface, as well as, to evaluate and compare its potential to overcome the state of the art of the dental implants market.

The following chronogram summarizes the work methodology used in this Thesis, which will be describe along the different chapters.
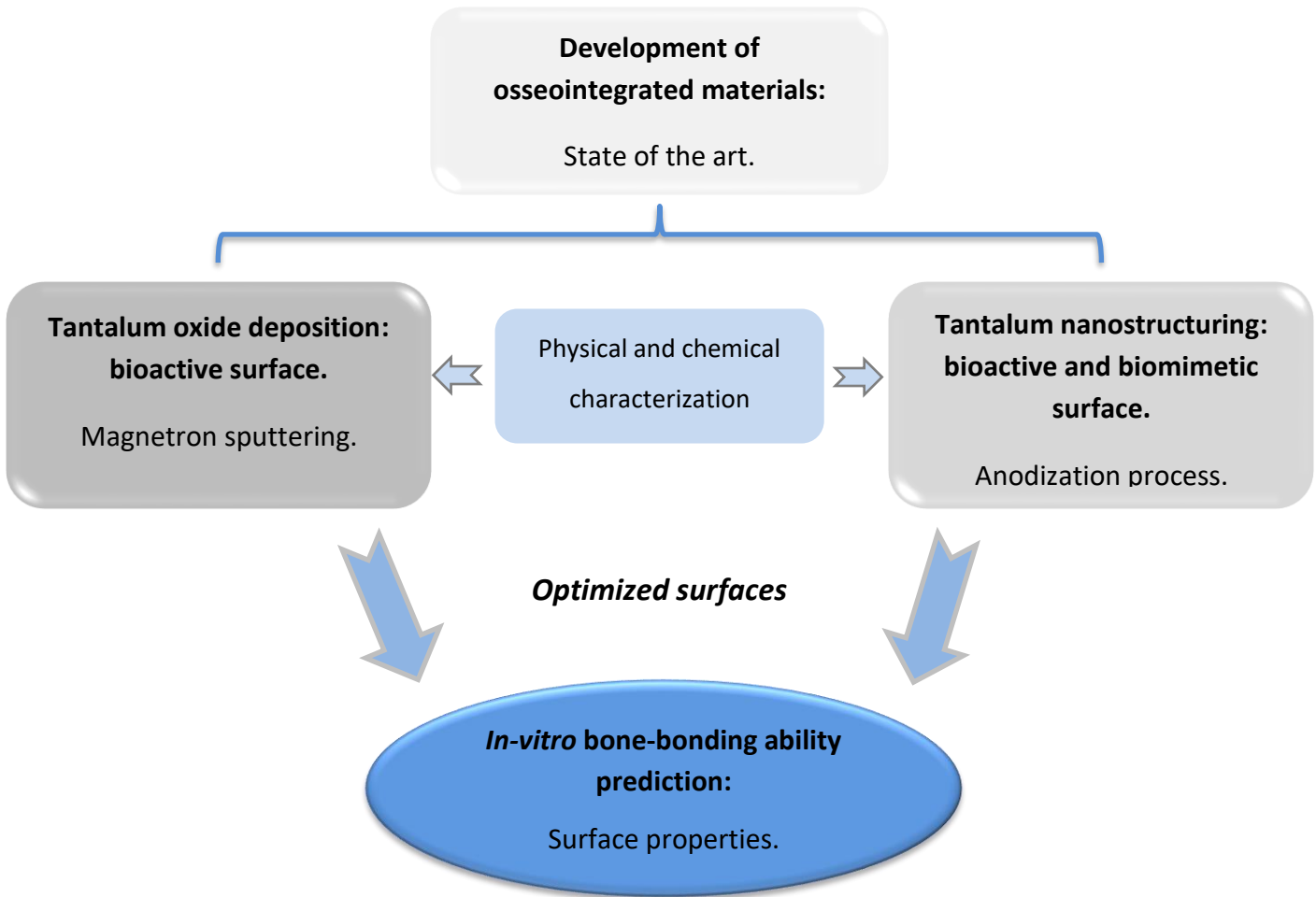
This document is organized in 5 chapters in order to provide a logical sequence to understand the production of $Ta_{1-x}O_x$ either by magnetron sputtering or anodization process and their subsequent characterization. Each chapter is based on papers published in international journals, or in the submission process.

Chapter 1 introduces the topic of the thesis, focused on the main problems that need to be addressed for the development of enhanced surfaces in the field of dental implants. Along the chapter, a detailed review of the literature regarding the development of tantalum oxides by magnetron sputtering or anodization process is provided.

The Chapter 2 includes a brief description of the production methodologies used in this thesis, as well as, a brief description of the characterization techniques. A short explanation of the techniques and the experimental parameters used during the development of the work is given.

The Chapter 3 reports the optimization of the coatings deposition with increasing oxygen content up to the stoichiometric Ta_2O_5, in order to get some insights about the structural and morphological features, which represent a base to analyze and correlate with functional properties studied.

Based on the results obtained in the third chapter, Chapter 4 is dedicated to the coatings validation in what concerns electrochemical response in artificial saliva as a function of immersion time, since commonly the degradation of metallic dental implants is caused by corrosion processes.

Chapter 5 summarizes the surface properties evaluation analyzing the effect of the composition on the *in-vitro* bone-bonding tendency as a final validation of the samples developed by magnetron sputtering regarding the main objective of the proposed work.

The chapter 6 is focused on the nanostructures development and understanding of the relationships between anodization conditions such as, the electrolyte, potential and time, on the size, geometry and distribution of the nanostructures in the anodic layer formed on Ta-based materials.

Lastly, Final remarks and future research presents an overall conclusion of the thesis and discusses possible future research perspectives.

1.2. References

[1]   J. Disegi, "Titanium alloys for fracture fixation implants", *Injury,* vol. 31, pp. D14-D17, 2000.
[2]   O. E. Pohler, "Unalloyed titanium for implants in bone surgery", *Injury,* vol. 31, pp. D7-D13, 2000.
[3]   M. Oliveira, L. Pereira, and C. Cairo, "Porous structure characterization in titanium coating for surgical implants", *Materials Research,* vol. 5, pp. 269-273, 2002.
[4]   H. Rack and J. Qazi, "Titanium alloys for biomedical applications", *Materials Science and Engineering: C,* vol. 26, pp. 1269-1277, 2006.
[5]   X. Ye, Y. Yang, and G. Tang, "Microhardness and corrosion behavior of surface gradient oxide coating on the titanium alloy strips under high energy electro-pulsing treatment", *Surface and Coatings Technology,* vol. 258, pp. 467-484, 2014.
[6]   X. Ye, L. Wang, Z. T. H. Tse, G. Tang, and G. Song, "Effects of high-energy electro-pulsing treatment on microstructure, mechanical properties and corrosion behavior of Ti–6Al–4V alloy", *Materials Science and Engineering: C,* vol. 49, pp. 851-860, 2015.

[7] S. E. Kim, J. H. Lim, S. C. Lee, S.-C. Nam, H.-G. Kang, and J. Choi, "Anodically nanostructured titanium oxides for implant applications", *Electrochimica Acta,* vol. 53, pp. 4846-4851, 2008.

[8] A. Maho, S. Linden, C. Arnould, S. Detriche, J. Delhalle, and Z. Mekhalif, "Tantalum oxide/carbon nanotubes composite coatings on titanium, and their functionalization with organophosphonic molecular films: A high quality scaffold for hydroxyapatite growth", *Journal of Colloid and Interface Science,* vol. 371, pp. 150-158, 2012.

[9] Z. H. Baqain, W. Y. Moqbel, and F. A. Sawair, "Early dental implant failure: risk factors", *British Journal of Oral and Maxillofacial Surgery,* vol. 50, pp. 239-243, 2012.

[10] L. Zhang, C. Ning, T. Zhou, X. Liu, K. W. Yeung, T. Zhang, Z. Xu, X. Wang, S. Wu, and P. K. Chu, "Polymeric Nanoarchitectures on Ti-Based Implants for Antibacterial Applications", *ACS Applied Materials & Interfaces,* vol. 6, pp. 17323-17345, 2014.

[11] M. Esposito, J. Hirsch, U. Lekholm, and P. Thomsen, "Biological factors contributing to failures of osseointegrated oral implants. (I) Sucess criteria and epidemiology", *European Journal Oral Sciences,* vol. 106, pp. 527-551, 1998.

[12] T. Miyazaki, H.-M. Kim, T. Kokubo, C. Ohtsuki, H. Kato, and T. Nakamura, "Mechanism of bonelike apatite formation on bioactive tantalum metal in a simulated body fluid", *Biomaterials,* vol. 23, pp. 827-832, 2002.

[13] B. R. Levine, S. Sporer, R. A. Poggie, C. J. Della Valle, and J. J. Jacobs, "Experimental and clinical performance of porous tantalum in orthopedic surgery", *Biomaterials,* vol. 27, pp. 4671-4681, 2006.

[14] V. K. Balla, S. Banerjee, S. Bose, and A. Bandyopadhyay, "Direct laser processing of a tantalum coating on titanium for bone replacement structures", *Acta Biomaterialia,* vol. 6, pp. 2329-2334, 2010.

[15] C. J. Frandsen, K. S. Brammer, K. Noh, G. Johnston, and S. Jin, "Tantalum coating on TiO2 nanotubes induces superior rate of matrix mineralization and osteofunctionality in human osteoblasts", *Materials Science and Engineering: C,* vol. 37, pp. 332-341, 2014.

[16] Y. Leng, J. Chen, P. Yang, H. Sun, J. Wang, and N. Huang, "The biocompatibility of the tantalum and tantalum oxide films synthesized by pulse metal vacuum arc source deposition", *Nuclear Instruments and Methods in Physics Research Section B: Beam Interactions with Materials and Atoms,* vol. 242, pp. 30-32, 2006.

[17] W. Yang, Y. Liu, Q. Zhang, Y. Leng, H. Zhou, P. Yang, J. Chen, and N. Huang, "Biomedical response of tantalum oxide films deposited by DC reactive unbalanced magnetron sputtering", *Surface and Coatings Technology,* vol. 201, pp. 8062-8065, 2007.

[18] T. Kokubo, T. Matsushita, H. Takadama, and T. Kizuki, "Development of bioactive materials based on surface chemistry", *Journal of the European Ceramic Society,* vol. 29, pp. 1267-1274, 2009.

[19] C. Arnould, T. Korányi, J. Delhalle, and Z. Mekhalif, "Fabrication of tantalum oxide/carbon nanotubes thin film composite on titanium substrate", *Journal of colloid and Interface Science,* vol. 344, pp. 390-394, 2010.

[20] N. Wang, H. Li, J. Wang, S. Chen, Y. Ma, and Z. Zhang, "Study on the anticorrosion, biocompatibility, and osteoinductivity of tantalum decorated with tantalum oxide nanotube array films", *ACS Applied Materials & Interfaces,* vol. 4, pp. 4516-4523, 2012.

[21] Y.-S. Sun, J.-H. Chang, and H.-H. Huang, "Corrosion resistance and biocompatibility of titanium surface coated with amorphous tantalum pentoxide", *Thin Solid Films,* vol. 528, pp. 130-135, 2013.

[22] S. Lavenus, J. Rozé, A. Hoornaert, G. Louarn, and P. Layrolle, "Chapter 5 - Impact of Nanotechnology on Dental Implants," in *Emerging Nanotechnologies in Dentistry*, K. Subramani and W. Ahmed, Eds., ed Boston: William Andrew Publishing, 2012, pp. 71-84.

[23] K. Subramani, D. Tran, and K. Nguyen, "Chapter 8—Cellular Responses to Nanoscale Surface Modifications of Titanium Implants for Dentistry and Bone Tissue Engineering

Applications", *Emerging Nanotechnologies in Dentistry, William Andrew Publishing, Boston, MA,* pp. 113-136, 2012.

Cristiana Filipa Almeida Alves

Chapter 1

State of the art

1.1. Introduction

In this chapter, an overview of tantalum (oxide) surfaces produced by magnetron sputtering or anodization process is provided. The most relevant works in the field are summarized in what concerns the most important issues of the present thesis: development of a novel bioactive and osseointegrated surface based on the synergetic effect of an oxide and a nanostructured surface of Ta-based materials.

1.2. Dental implants problems

Currently, most dental implants are manufactured on commercially pure titanium grade 2 (CP Ti Gr2) or in titanium-6aluminium-4vanadium alloy (Ti6Al4V – Ti Gr5), with threaded geometries with internal connections for the abutments [1]. Conventional implants can be manufactured with a porous microstructure propitiating a more efficient bone tissue ingrowth by the increase of the specific surface in contact with the surrounding media. For instance, some studies show that the micrometer porosity can enhance primary fixation due to the increase of mechanical anchorage by increasing the contact area, compensating in some way the poor bioactivity [2]. However, it is known that the use of titanium (Ti) is not able to eliminate the occurrence of biological complications after their insertion into the human body, mainly due to the slow osseointegration [3, 4].

The slow osseointegration of titanium dental implants leads to loading delay of the implant by the artificial crown, thus requiring a long non-operational time (around 4-6 months, depending on the patient) [5, 3]. However, the most relevant issue is related with the increase in the probability of microorganism's entrance on the oral environment close to the surgical site, specifically to the surface of the dental implant. This adhesion and possible microbial colonization can induce the appearance of infections with consequent post-surgical complications [6, 7]. Infections are the main responsible for the short, medium and long-term failure of the dental implants. Failure due to periimplantis disease, which is related with the late infection of the adjacent bone tissue, makes the bone recede and subsequently a decrease in the mechanical anchorage of the implant is observed, blocking the osseointegration. As a consequence, when the soft-hard tissue

recedes, "grey" Ti is exposed giving poor aesthetics [8, 9]. Additionally, the existence of micro-mobility of dental implant induced by the inefficient healing and slow osseointegration has a negative effect. The micro-movements lead to a tensile and shear stresses on the implant surface that induces the encapsulation of the implant with fibrous tissue, as presented in Figure 1.1a, blocking the contact between the dental implant surface and the bone, which also delays the osseointegration. Additionally, as Ti shows a low tribocorrosion resistance, thus the presence of micro-mobility in an acid oral environment can be critical, which in long term may result in loss of the implant [9, 10].
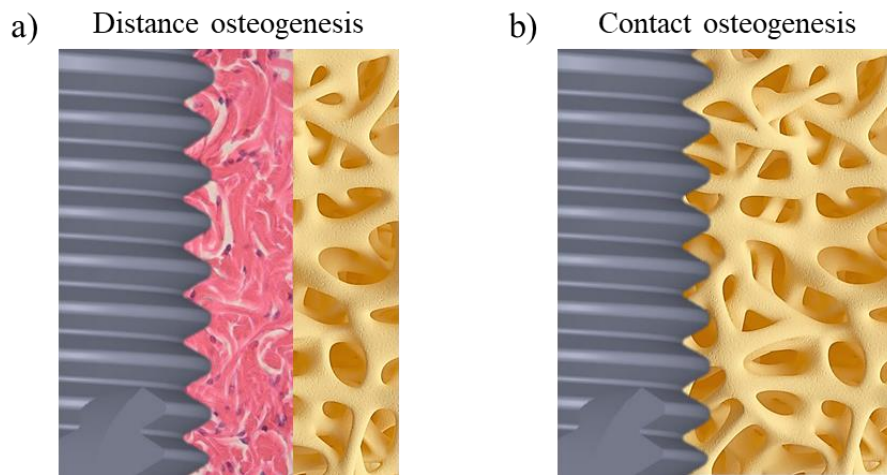
Figure 1.1: Schematic representation of the (a) distance osteogenesis and (b)contact osteogenesis, adapted from [18].

The integration of dental implants is divided in two phases: the first phase is ensured by mechanical anchorage that derives from the design of the implant and the host bone structure. Overtime, the primary mechanical retention decreases towards the biological anchorage (second phase) increases, which is a consequence of the formation of an interface between the implant surface and the bone [10].

The interaction between the bone and the implant surface is dynamic and outcomes from bone anchorage and stability of the biomaterial. The primary stability between the implant and the bone, needed to achieve a successful implantation, is characterized by a rigid fixation and absence of movement [9]. On this regard, metallic materials are still indispensable for load-bearing applications with bone tissue replacement as for

construction of dental implants [11, 12]. This contact is influenced by several factors including the material, the design of the artificial structure and surface finish [9].

For achieving the secondary stability of dental implants, the surface of the implants should be highly bioactive, *i.e.* promote the adhesion, growth and osteogenic differentiation of osteoblasts and then, bone matrix mineralization. Bioactivity arises from a functional and direct contact between the living tissue and the surface of the dental implant (direct osteogenesis) that will subsequently be subjected to functional loads (masticatory load) [9, 10].

In recent years there have been a great interest in the development of bioactive surfaces. In this context, strong activities are focused in the modification of surface characteristics of dental implants in order to enhance the implant healing process [13].

Indeed, the main dental companies have been developing surface treatments to improve osseointegration and offer shorter healing times. For instance, SLA or SLActive Straumann® Dental implant Systems from the Swiss company Straumann, one of the world leaders in dental implantology, has its surface modified with large-grit sandblasting or large-grit sandblasting + acid etching, respectively, creating a microporous and oxidized topography. On the other hand, its business competitor, the countrymate Nobel Biocare, developed a TiUnite surface based on an oxidized and microporous surface obtained by anodization that have been applied to the most recent implant designs, such as NobelActive. Moreover, companies like Neo Biotech, Sweden & Martina and Dio Implant, among others, also have dental implants in which the surface is modified by sandblasting and/or acid etching. Still, these treatments have not been efficient to overcome the poor osseointegration and thus, the failure rate is still too high.

To reach a new surface able to enhance and promote the osseous growth and bone matrix mineralization and then, reduce the frequency of infective complications, it is mandatory to understand how the surface properties control the osseointegration and how they can be manipulated to improve the biological response.

1.3. Importance of surface properties in osseointegration

The dental implants stability depends on the primary anchorage and the biological healing, as was already described. Over time the mechanical retention decreases, while the osseointegration increases (as presented in Figure 1.2). During this transition, a bonding interface is formed between the implant surface and the bone. Depending on the materials surface properties, this transition can be critical and thus, it should be carefully take into consideration in dental applications.
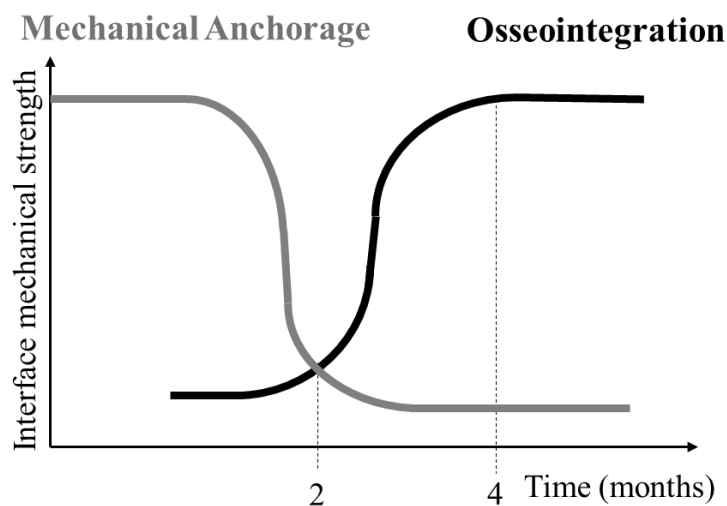
Figure 1.2: Schematic representation of mechanisms regulating the dental implant integration over the time (mechanical anchorage + osseointegration).

It is important to note that a material surface is characterized by three main categories: physicochemical; morphological/topographical; and mechanical properties; as represented in Figure 1.3. All of these properties are correlated and regulate the biological behavior in terms of protein adsorption, cell adhesion, proliferation and differentiation and subsequently, tissue integration [14].
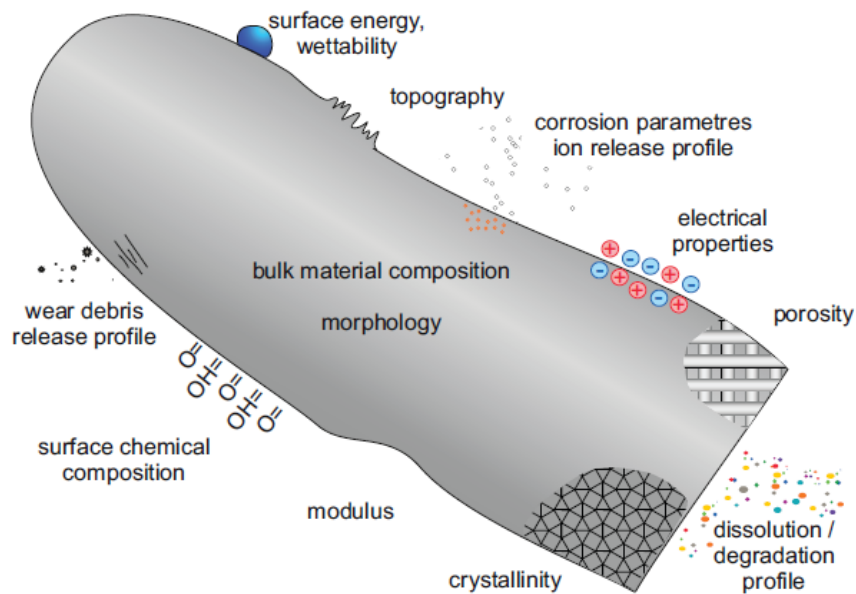
Figure 1.3: Schematic representation of the surface properties [15].

One of the most important parameters that should be taken into account for tissue engineering applications is the materials wettability. Generally, higher wettability (*i.e.* high surface free energy) increases the affinity of the surface to adsorb ions from the medium [15, 16]. Although this physicochemical property does not affect directly the cell response, could regulate significantly the adsorption of the most important proteins from the culture medium, such as fibronectin and vitronectin, that mediates the cell response and improve the cell adhesion. According to the literature [17], moderately hydrophilic surfaces (≈70-60°) tends to adsorb cell adhesion-promoting proteins (fibronectin and vitronectin), which improve the cell attachment.

By the literature [18], it is known that immediately after the dental implantation there is an immune response that induces the interaction between the blood components and the implant surface, as represented in Figure 1.4. The plasma proteins (such as fibronectin and vitronectin) are adsorbed within a minute by the implant surface, which modify the surface chemistry (Figure 1.4.a), while the platelets are responsible for the thrombus formation during blood clothing. Subsequently, a vascular membrane is formed (Figure 1.4. b and c), which is responsible for the interactions between the osseous cells and the implant surface.
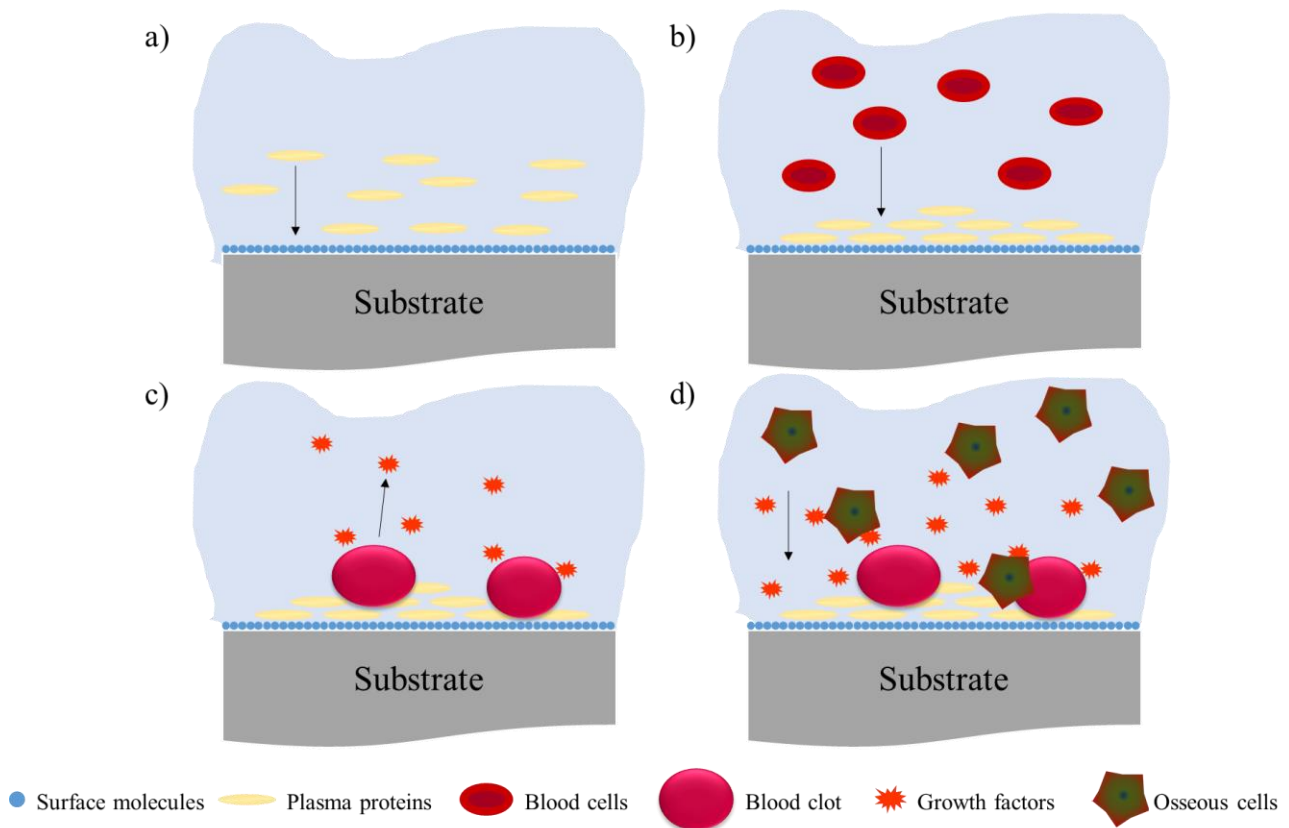
Figure 1.4: Scheme of the immune response caused by the dental implantation: (a) Adsorption of plasma proteins; (b) Blood cells migration; (c) Thrombus formation and blood clotting followed by bioactive factors release; (d) Osseous cells migration.

Furthermore, the blood clotting, caused by the immune response, serves as release system for bioactive factors (such as growth factors) that are determinant to attract and differentiate stem cells (undifferentiated bone narrow cells) into osseous cells (Figure 1.4.d), whereas the platelets will be also responsible for the cell proliferation.

In this context, the interaction of the blood with the implant surface is dependent from the material surface wettability, which, as mentioned, leads to protein adsorption [18]. On its turn, it is well recognized that surface chemical composition and topography affect the surface wettability, which subsequently influences the healing process [17, 19]. Thus, tuning the implant surface properties like chemical composition and topography can produce with extraordinary results for implantology.

Regarding surface chemical composition, implants with oxidized surfaces play an important challenge in implantology considering that the biochemical interaction between the implant and the bone is in part determined by the metal oxide surface properties [20, 21]. The properties of the metal oxides determine the biochemical interactions since bone progenitor cells interact better with the oxide layer because its ability to form a diffusion zone that promotes a stronger chemical bond [22-24]. Besides changing the surface energy, the surface oxides also modify the adhesion kinetics, the type of adsorbed ions and consequently the space ions conformation. All of these phenomena affect the ability that the surface has to connect to neighboring cells [22, 23].

In the case of ceramic materials, such as Ta_2O_5, TiO_2, ZrO_2 among others, immediately after their contact with water-based body fluids a layer of OH^- groups is formed on the surface. Hence, the interactions between the material surface and the cells happen probably due to the electrostatic forces between the positive amino acids from the body fluid with the negatively charged implant surface or between the negative amino acids from the body fluid with the positive ions, previously adsorbed on the implant surface (*e.g.* Ca^+) [15, 16], as represented in Figure 1.5, forming the diffusion zone that promotes a stronger chemical bond [25].
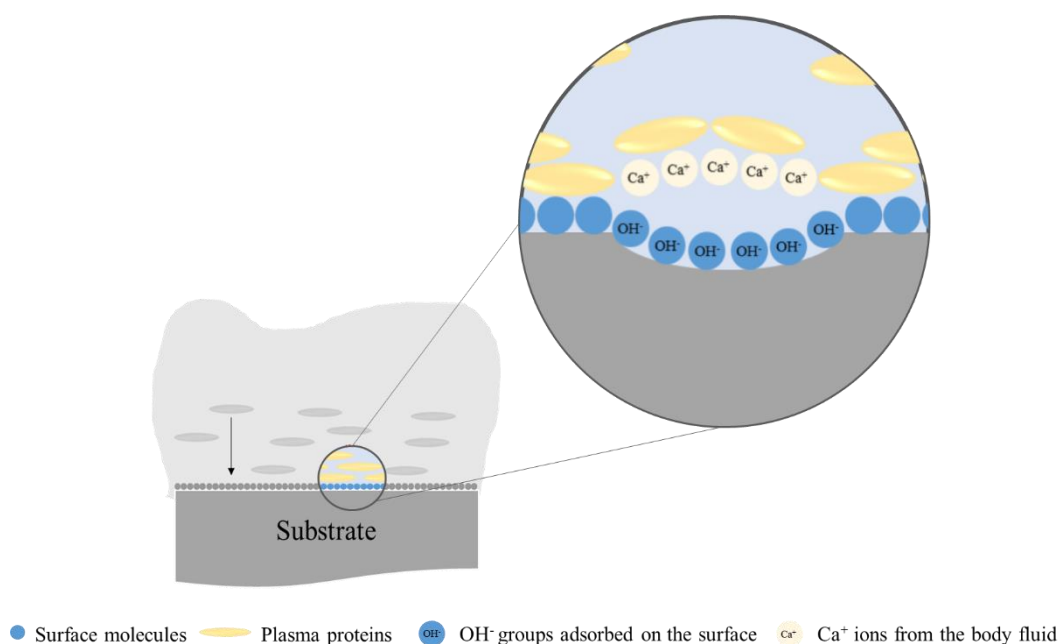
Figure 1.5: Schematic representation of the interactions between the implant surface negatively charged and the positive ions from the body fluid.

On the other hand, the surface topography is related with roughness and the asperities. Several authors claim that the roughness enhances the osseointegration, revealing a better biological response. In fact, it is recognized that relatively high roughness favors the initial stages of cell adhesion during the healing process. *In-vivo* studies have demonstrated that the increase in surface area increases the bone-implant contact improving the connection between them. Commercially, micrometric porous structures are accepted and associated to enhanced osseointegration since improves the mechanical retention, promoting a better fixation between the dental implant and the bone. However, there is no consensus regarding the optimum roughness value for osseointegrated applications, with the discussion being usually in the order of the micrometers (µm) [26]. According to T. Albrektsson and A. Wennerberg [26], low roughness (0.5–1 µm) have no significant effect on osseointegration. On the other hand, rough surfaces (>2 µm) may favor the incidence of tissue inflammation and, consequently, the appearance of diseases in long-term cases. In fact, some studies suggest that very rough surfaces boost the appearance of peri-implantitis. Moderate roughness (1–2 µm) allows a quick healing, due to the trap of blood cells on the surface of the implant in the initial phase without compromise the osseointegration in long-term. Nevertheless, the optimal values for moderate roughness may vary from author to author.

On the other hand, structures with nanometric dimensions are able to biomimetize bone tissue and promote osseointegration. In fact, bone tissue is recognized as nanostructured and osseous cells prefer biomimetic nano-roughness surface [27]. The modification of implant topography at the nanoscale (volume porosity, nanofeature size and shape) results in an increase of the interactions between the dental implant surface and the proteins, ions, biomolecules and bone cells, which influences the adhesion, proliferation and differentiation of osteoblasts, accelerating osseointegration [18, 28]. For instance, the nanopattern topography causes cell elongation, increasing the number of cytoplasmatic extensions (well)attached to the surface (see Figure 1.6), as well as, increase the number of the cells adhered due to the wettability increase [28]. Moreover, for example, a surface covered by nanotubes, depending on the size and spacing between them, may store nutrients needed to the proliferation and differentiation from the cells adhered initially [18].

Cell nucleus   Extracellular matrix   Cytoplasmatic extensions
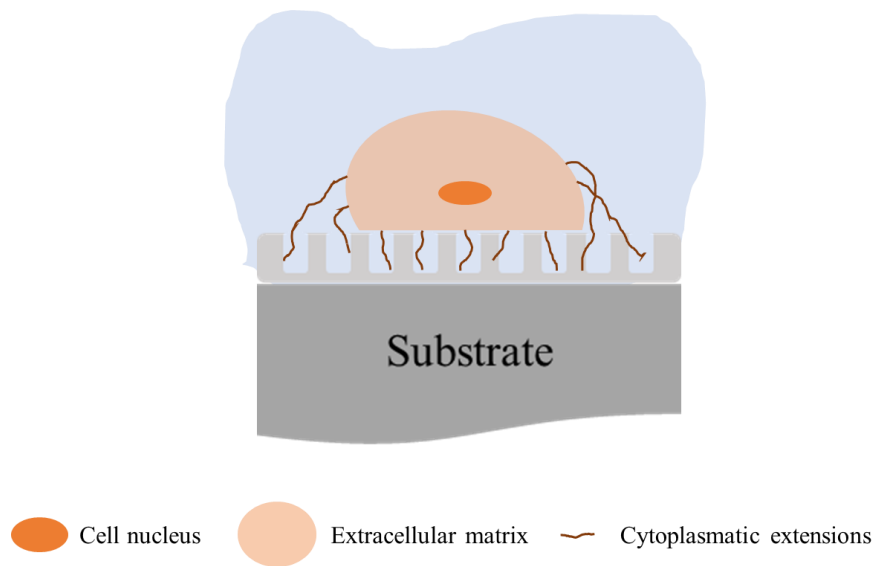
Figure 1.6: Schematic representation of the interaction of the osseous cells with a nanostructured surface.

The differentiation of stem cells is also affected by the roughness at nanoscale level. The contact between the stem cells and the implant surface may promote differentiation of two types of cells: osteoblastic cells, which constitute the bone tissue; and fibroblastic cells, which constitute the gum tissue. In some cases, there is an excessive differentiation of the stem cells into fibroblastic cells. The excessive gum tissue formation can encapsulate the dental implant with gum and thus, the direct osteogenesis is jeopardized, leading to the implant rejection due to the absence of osseointegration [18]. Taking into consideration that the natural bone is nanostructured, it is reported that a smooth surface leads to the encapsulation of the dental implant with fibrous tissue in response to the non-biomimetic surface. This fibrous encapsulation is unwanted since it creates an interface between the implant and bone, jeopardizing the implant attachment [28]. A nanostructured surface, promotes the cells differentiation into osteoblastic cells, integrating the implant directly with bone, as well as, decreasing the fibroblast adhesion and proliferation [18, 28].

Additionally, the nanostructures can produce a bactericidal effect caused by mechanical deformation of microbial cells. Due to the nanostructured surface ability to attract and

force the microbial cells to adapt to the nanotopography, subsequently the deformation stress will cause their death [29].

Optimizing the surface morphology at nanoscale level, it is possible to prevent bone resorption and accelerate/initiate bone growth, thereby decreasing the healing time and risk of bacterial colonization.

According to L. Meirelles [30] although the surface nanostructures enhance the cell activity and cell proliferation in *in-vitro* tests, in *in-vivo* tests there is no evidence of the cell response be affected only by the surface nanostructures but by a compromise between the micro + nano structures presented in the surface.

In summary, surface modification aims to promote bone response favoring osseointegration. The chemistry and topography of the implant surface are determining factors in this process. On this regard, the surface modification intends to improve primary stability by obtaining a higher contact area between the implant and the bone, accelerate the adhesion, growth and maturation of cells and reduce the healing time, by controlling the interactions between the implant surface and the cells, and finally, ensure successful fixation in areas with lower quality of host bone [26].

1.4. Bioactive materials

As previously mentioned, nowadays dental implants are produced using Ti-based materials due to its biocompatibility and corrosion resistance, as well as, do not cause allergic reaction [31, 32, 2, 33-35]. However, Ti-based surfaces do not show ability to stimulate the formation of new apatite containing tissue [7] and then, delays the biological integration. Moreover, Ti-based surfaces show a low tribocorrosion resistance and subsequently in the presence of micro-mobility in an aggressive oral environment can be critical.

Another possibility to reduce the problems associated with the Ti can be the use of highly bioactive ceramic materials, such as synthetic hydroxyapatite (HA), bioglass or ceramic

glass. Notice that it is recognized the faster healing revealed by these materials, as well as, the tolerance to the micro-mobility during the first stages of the implantation, improving bone-bonding response. Still, the low tensile strength and low fatigue resistance, as other mechanical properties, due to the fact that ceramic materials are fragile and brittle, makes impracticable the use of a fully ceramic implant. One way to combine the good mechanical properties of metallic materials with good biological properties of bioactive ceramics could be the use of composite materials. However, it is extremely difficult to obtain a good interface between the bioactive material and the inert matrix, not allowing to have an effective charge transfer during mastication [36].

The new generation of biomaterials used tantalum (Ta) as a promising material since, comparing to CP Ti Gr2, is bioactive due to its interesting chemistry valences, which promotes biomineralization kinetics, thus enhancing the osseointegration [37, 22, 23, 38, 4, 39]. The substitution of commercial Ti dental implants by Ta allows to improve the healing process of the implant in order to overtake the biological limitations that dental implants still present [37, 22, 23, 38]. The high cost and high density of Ta are the major drawbacks, which makes bulk Ta dental implants less cost effective than a dental implant coated with Ta [40].

According to V. K. Balla *et al.* [41] the cellular growth onto Ta surfaces is more intense than onto Ti surfaces. The study compared the biological response of Ta coatings, produced by LENS (Laser Engineered Net Shaping) and deposited onto Ti substrates, with Ti surfaces as surface control. Cell viability tests were performed by measuring the enzymatic cellular activity (MTT assay) with hFOB (Fetal Osteoblast). The results of Ta surfaces are significantly better regarding adhesion, cell growth and proliferation, when compared with Ti surfaces. The increase of the surface free energy (high wettability) promotes the increase of cellular interactions, which improves the biological fixation through enhanced cell adhesion and proliferation [38, 41]. In addition, C. J. Frandsen *et al*. [42] found that Ta shows a better biological response compared to titanium dioxide (TiO_2) surfaces, when alkaline phosphatase activity tests were performed. In fact, Ta revealed a faster matrix mineralization rate ($\approx$30%) due to its surface chemistry properties.

Moreover, Ta reveals a high affinity to react with oxygen (O), which makes tantalum oxides (TaO$_x$) its most common form. The Ta+O system may present different stoichiometries; however, tantalum pentoxide (Ta$_2$O$_5$) is the more stable phase among others TaO$_x$. The higher surface free energy of TaO$_x$ stimulates the regeneration process in living tissues and thus, increases the osseointegration efficiency [22, 20, 21, 25]. This suggests that TaO$_x$ coatings deposited onto commercial surfaces should play an important role in the interface between the bone and implant. Mostly, the native oxide, Ta$_2$O$_5$, promotes the biomineralization due to its ability to bind with calcium, enhancing the bone ingrowth [22].

To Y. X. Leng *et al.* [20], the use of Ta or Ta$_2$O$_5$ coatings in cardiovascular stents is an alternative in the market. Indeed, the superior bioactivity of these materials is evident when *in-vitro* tests by culturing HUVEC cells (Human Umbilical Vein Endothelial Cells) were carried out and compared Ta-based surfaces with stainless steel 316L (SS 316L) and CP Ti. Ta coating was deposited by plasma immersion ion implantation and Ta$_2$O$_5$ was obtained by annealing Ta coating in an air atmosphere. After 24 hours of immersion, *in-vitro* results show the formation of a cell layer uniformly distributed on Ta and Ta$_2$O$_5$ surfaces. In contrast, the surface of SS 316L and CP Ti was hardly covered by cells. Indeed, Ta and Ta$_2$O$_5$ revealed the highest density of endothelial cells on its surface when compared with the SS 316L and the CP Ti.

On the other hand, considering that the oral environment is extremely complex and acid, although the excellent osseointegration shown by bioactive surfaces, the degradation of metallic dental implants cannot be neglected.

Previous works studying the corrosion of Ti-based dental implant materials reported that the stability of the TiO$_2$ protective passive layer (Me-O) is pH dependent and can degrade in the oral environment due to the presence of corrosive substances in saliva. Considering the biological response, Ta-based materials are an alternative to Ti dental implants [43, 44]. However, only a few studies about corrosion behavior of Ta-based materials exist. Even out of the dental implant application, these studies report the corrosion response of steel (*e.g.* AISI 4340 or ASTM A723) coated with Ta-based material. These studies are focused on the influence of crystalline phases [45, 46] or surface roughness [47] in acid

environments (*i.e.* H_2SO_4), or the influence of different Ta deposition methods in saline environments (NaCl) [48]. For instance, it has been reported that coatings with α-Ta or β-Ta phases show protective behavior to steel substrates being dependent of the presence of defects such as pinholes or porosity [45, 46]. In case of defects presence, the corrosion processes are controlled by the steel dissolution through the open pores. Additionally, it is reported that the corrosion protection is maintained even using substrates with different roughness [47]. Beyond that, the electrochemical performance for TaO_x shows to be dependent on the oxide morphology/density, revealing a lower oxide breakdown potential and faster pit growth on highly porous Ta_2O_5. Furthermore, some studies are focused on Ta_2O_5 corrosion behavior for bio-applications in Simulated Body Fluid (SBF) environment, which presents a more neutral character compared to simulated saliva. Besides Ta-based coatings improve corrosion resistance of Ti, denser Ta_2O_5 coating improved the corrosion resistance in biological environments [49, 50].

In an attempt to improve the osseointegration of dental implants on the dental market, there is some works developing nanostructured Ti oxide based surfaces. However, the known biological limitations of Ti-based surfaces, with occurrence of surgical complications after implant insertion into the human body, still represent an issue that is inconvenient for the patients and increases the treatment costs [5, 18, 42]. The present work arises with the substitution of typical Ti by a multifunctional (nanostructured and bioactive) surface of Ta-based materials.

The development of highly bioactive surfaces based on Ta may be achieved through the deposition of TaO_x based coatings by magnetron sputtering or by nanopatterning a bulk Ta by anodization process. Either the magnetron sputtering deposition or anodization process allows to achieve a bioactive TaO_x surface with enhanced osseointegration and corrosion resistance. Moreover, anodization method also allows the formation of surface nanostructures, which could enhance the interaction between the implant surface and the cells from adjacent tissues.

1.4.1. Tantalum oxide produced by magnetron sputtering: bioactive surface

Several deposition techniques have been explored to deposit Ta and TaO_x thin films, including sol-gel, metal-organic decomposition method, plasma immersion, ion implantation, pulsed laser deposition, chemical vapor deposition (CVD) or magnetron sputtering (MS) [51, 52, 23, 53-56]. Among these techniques, direct current (DC) MS is one of the most used in industry since it allows good quality films at high deposition rates, being cost effective [54].

Moreover, due to the variety of reactive gases that can be added, reactive DCMS is well known for its versatility and usefulness to deposit a wide range of compounds that would not be possible to deposit by other physical processes. For example, metal oxide coatings with different compositions can be obtained involving only a metallic target and modifying the reactive atmosphere (*i.e.* the ratio between argon - Ar and O_2 partial pressures), which makes the control of the deposition parameters extremely important to optimize the final properties of the films namely chemical state, structure or morphology [57].

As stressed before, Ta (oxide) coatings are attractive for biomedical industry due to their interesting wettability, bioactivity, osseointegration and electrochemical properties. However, the applicability of Ta-based coatings is completely dependent on the physiochemical, morphological/topographical and mechanical properties [58, 55, 41, 59].

Bulk Ta has a body centered cubic (bcc) stable phase with relatively high mechanical properties such as toughness and ductility and relatively low electrical resistivity. On the other hand, Ta thin films can also show a harder and more brittle tetragonal metastable phase, which is usual in thin films, with higher electrical resistivity [40]. Depending on the deposition conditions and the substrate, Ta coatings can show any of these phases or a mixture of them [60], with a large range of chemical compositions. The most common TaO_x have been identified as: Ta_2O with a bcc; TaO with a face centered cubic (fcc); TaO_2 with a tetragonal; and Ta_2O_5 with an orthorhombic crystal structures. Beyond that, Ta_2O_5 structure is the more thermodynamically stable phase [52]. All these phases have similarities based on the common element, Ta, since they are formed by the distortion of the Ta base structure [60-62], and can be found in coatings deposited by reactive DC MS [21, 63, 64].

Regarding Ta_2O_5, its complex crystal structure determines its properties. An allotropic transformation of $Ta_2O_5 \approx 1360$ °C is known, but the crystal structure of each phase is still a subject of controversy. Ta_2O_5 crystal structure, as well as, the electronic structure and oxygen vacancies, have been studied for several years and several structures have been proposed [65, 57]. K. Lehovec [66] proposed an orthorhombic phase with a large number of oxygen vacancies, known by L- Ta_2O_5, as the low temperature crystal structure. In the high temperature phase, several authors proposed a tetragonal phase, named by H- Ta_2O_5 [67, 68]. Later, N. Stephenson and R. Roth reported [69] a vacancy-free L- Ta_2O_5 orthorhombic structure as the low-temperature crystal structure, nowadays named by β-Ta_2O_5. Besides, an irreversible phase transformation with temperature allowed to identify a hexagonal low-temperature metastable phase, δ- Ta_2O_5 [70]. All the Ta_2O_5 reported phases are similar considering the oxygen ions position in the *c* direction, which is between two Ta ions. The main difference between these structures is the oxygen ions position in the *a* and *b* directions [71].

1.4.2. Tantalum oxide produced by anodization: nanostructured and bioactive surface

Currently, highly ordered nanostructured surfaces are known to improve and promote the osseointegration due to bone biomimetic properties, as well as, prevent the infections appearance due to the antibacterial properties [27, 29]. Several nanofeatures are available, like nanopores, nanotubes and nanorods, however the first ones represent the closest biomimetic structure, taking in consideration the bone tissue morphology. On this concern, developing nanoporous metal structures with regular pore patterns and uniform pore diameters holds the key to manipulate the osseointegration mechanism.

Low-cost electrochemical methods, such as anodization process, have been used to produce nanoporous structures with regular pore patterns and uniform pore diameters [72]. The anodization is characterized by a voltage application between the anode (implant) and the cathode (lead, carbon, platinum, etc...) in the presence of an electrolyte, which generates the charge and ions transfer causing the "growth" of a metal oxide onto the implant surface. Typically, this process is associated with an increase of the

microscopic surface roughness and in certain conditions is also possible the formation of pores at nano size scale [5, 73].

Ta anodization easily leads to the formation of a dense anodic oxide layer, usually Ta_2O_5 [74]. This anodic layer reveal specific characteristics, such as high corrosion resistance and inert behavior, responsible for the high resistance to chemical attack [75, 76]. Moreover, some studies reported the formation of porous anodic TaO_x layers in a glycerol with 0.2 M NH_4F by applying a potential in the range of 10-50 V during 3 h. It is observed that the pores diameter, from 13 nm to 40 nm, is linearly proportional to the applied potential, respectively [77]. Nonetheless, the results revealed a cracked and disordered porous oxide layer. Indeed, due to the high chemical resistance, TaO_x is only efficiently chemically attacked by strong acids such as hydrofluoric acid, which causes chemical dissolution [76]. On this context, several authors reported that the formation of an ordered nanoporous layer is only possible with a mixture of sulphuric and hydrofluoric acids (H_2SO_4 and HF) [78-82, 72]. As example, H. El-Sayed *et al.* reported [72] the formation of a highly ordered nanoporous layer with low potentials around 10-20 V, below the TaO_x breakdown potential ($\approx$200 V), at anodization times between 30 s and 10 min, using H_2SO_4 mixed with HF at high electrolyte concentrations (16.4 and 2.9 M, respectively).

The formation of a porous TaO_x layer, during anodization, results from a continuous process that involves a competition between oxidation of the metal in the oxide/metal interface and dissolution of the oxide on the oxide/electrolyte interface [81, 82]. Several studies suggest that nanopores growth in the first seconds of anodization, after the formation of the compact oxide layer. Thus, the growth of disordered pits due to the preferential radial spread promoted by field-enhanced dissolution on the small surface asperities leads to the formation of highly ordered TaO_x nanopores (Figure 1.7.b) [79, 81-83]. With increase of anodization time, fluoride ions react continuously with the anodic oxide being incorporated in their outer part forming a TaF_7^{2-} [79, 81, 84, 83] , according to the reaction presented in the Equation 1.1 [85] and as represented in Figure 1.7.c.

Equation 1.1

$$2\,Ta + 5\,H_2O \rightarrow Ta_2O_5 + 10\,H^+ + 10\,e^-$$

$$Ta_2O_5 + 14\,F^- + 10H^+ \rightarrow 2\,TaF_7^{2-} + 5\,H_2O$$
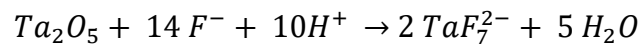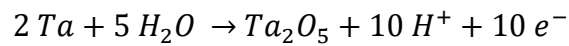
These metal-fluoride complexes are water-soluble being responsible for the pores growth and shape [84]. Due to the higher migration velocity of the fluoride ions, comparing with oxygen ions, the fluoride ions migrate from the outer part towards the walls of the anodic oxide layer, being responsible for the separation of the pores forming nanotubes due to its water solubility [84, 83]. A few seconds after, these nanotubes are vertically aligned and reach a maximum length, which limits the thickness of the oxide layer. At this stage, the anodic Ta oxide nanotubes lose stability [81]. The stability loss by the nanotubes may be related with the incorporation of fluoride ions in the bottom part of the anodic layer [79, 81, 84, 83], as represented in Figure 1.7.d, which decreases the adhesion between the metal and the anodic layer [79, 81]. The nanotubes removal leaves behind a surface with highly ordered nanopores [81].
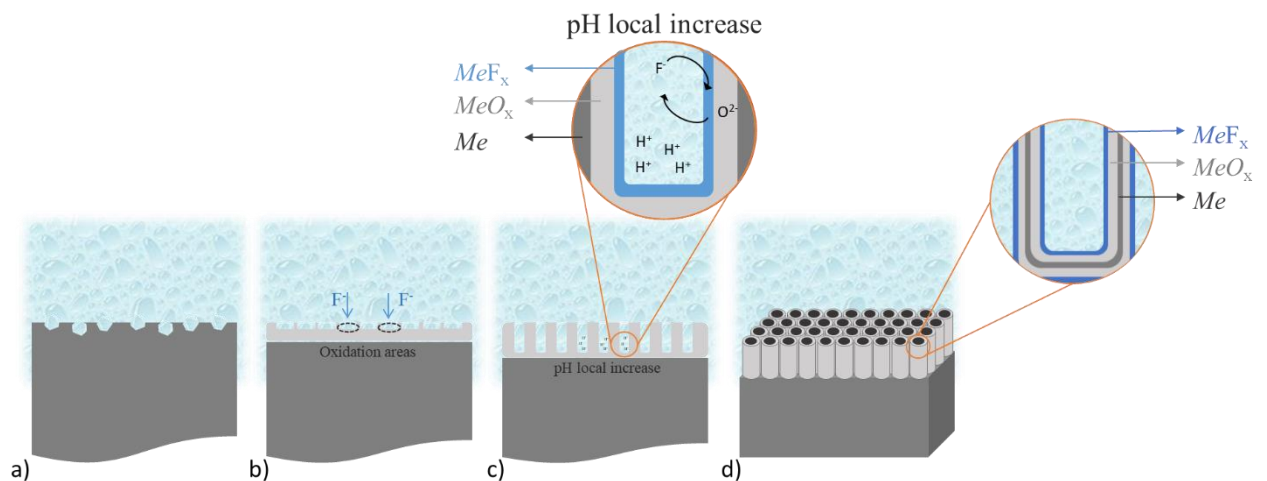
Figure 1.7: Schematic representation of nanopore-nanotube assemblies' mechanism formation: (a) Surface with pits before anodization; (b) Dissolution of Ta_2O_5 anodic layer and dimples formation; (c) Nanopores growth (Length growth by electric field); (d) Nanotubes or nanorods formation.

1.5. References

[1]   L. Vidyasagar and P. Apse, "Dental implant design and biological effects on bone-implant interface", *Baltic Dental Maxillofacial Journal,* vol. 6, pp. 51-54, 2004.

[2]   M. Oliveira, L. Pereira, and C. Cairo, "Porous structure characterization in titanium coating for surgical implants", *Materials Research,* vol. 5, pp. 269-273, 2002.

[3]   A. Maho, S. Linden, C. Arnould, S. Detriche, J. Delhalle, and Z. Mekhalif, "Tantalum oxide/carbon nanotubes composite coatings on titanium, and their functionalization with organophosphonic molecular films: A high quality scaffold for hydroxyapatite growth", *Journal of Colloid and Interface Science,* vol. 371, pp. 150-158, 2012.

[4]   M. Roy, V. K. Balla, A. Bandyopadhyay, and S. Bose, "MgO-doped tantalum coating on Ti: microstructural study and biocompatibility evaluation", *ACS Applied Materials & Interfaces,* vol. 4, pp. 577-580, 2012.

[5]   S. E. Kim, J. H. Lim, S. C. Lee, S.-C. Nam, H.-G. Kang, and J. Choi, "Anodically nanostructured titanium oxides for implant applications", *Electrochimica Acta,* vol. 53, pp. 4846-4851, 2008.

[6]   Z. H. Baqain, W. Y. Moqbel, and F. A. Sawair, "Early dental implant failure: risk factors", *British Journal of Oral and Maxillofacial Surgery,* vol. 50, pp. 239-243, 2012.

[7]   L. Zhang, C. Ning, T. Zhou, X. Liu, K. W. Yeung, T. Zhang, Z. Xu, X. Wang, S. Wu, and P. K. Chu, "Polymeric Nanoarchitectures on Ti-Based Implants for Antibacterial Applications", *ACS Applied Materials & Interfaces,* vol. 6, pp. 17323-17345, 2014.

[8]   M. Esposito, J. Hirsch, U. Lekholm, and P. Thomsen, "Biological factors contributing to failures of osseointegrated oral implants. (I) Sucess criteria and epidemiology", *European Journal Oral Sciences,* vol. 106, pp. 527-551, 1998.

[9]   R. Dimitriou and G. Babis, "Biomaterial osseointegration enhancement with biophysical stimulation", *Journal of Musculoskeletal and Neuronal Interactions,* vol. 7, pp. 253-265, 2007.

[10]   M. Plecko, C. Sievert, D. Andermatt, R. Frigg, P. Kronen, K. Klein, S. Stübinger, K. Nuss, A. Bürki, and S. Ferguson, "Osseointegration and biocompatibility of different metal implants - a comparative experimental investigation in sheep", *BMC Musculoskeletal Disorders,* vol. 13, pp. 1471-1483, 2012.

[11]   P. Branemark, G. Zarb, and T. Albrektsson, "Tissue integrated prostheses", *Surgical procedures,* pp. 211-232, 1985.

[12]   W. Singhatanadgit, "Biological responses to new advanced surface modifications of endosseous medical implants", *Bone and Tissue Regeneration Insights,* vol. 2, p. 1, 2009.

[13]   A. Mavrogenis, R. Dimitriou, J. Parvizi, and G. Babis, "Biology of implant osseointegration", *Journal of Musculoskeletal and Neuronal Interactions,* vol. 9, pp. 61-71, 2009.

[14]   D. Campoccia, L. Montanaro, and C. R. Arciola, "A review of the biomaterials technologies for infection-resistant surfaces", *Biomaterials,* vol. 34, pp. 8533-8554, 2013.

[15]   C. Eriksson, H. Nygren, and K. Ohlson, "Implantation of hydrophilic and hydrophobic titanium discs in rat tibia: cellular reactions on the surfaces during the first 3 weeks in bone", *Biomaterials,* vol. 25, pp. 4759-4766, 2004.

[16]   G. Zhao, Z. Schwartz, M. Wieland, F. Rupp, J. Geis Gerstorfer, D. Cochran, and B. Boyan, "High surface energy enhances cell response to titanium substrate microstructure", *Journal of Biomedical Materials Research Part A,* vol. 74, pp. 49-58, 2005.

[17]   K. Cai, M. Frant, J. Bossert, G. Hildebrand, K. Liefeith, and K. D. Jandt, "Surface functionalized titanium thin films: zeta-potential, protein adsorption and cell proliferation", *Colloids and Surfaces B: Biointerfaces,* vol. 50, pp. 1-8, 2006.

[18]   S. Lavenus, J. Rozé, A. Hoornaert, G. Louarn, and P. Layrolle, "Chapter 5 - Impact of Nanotechnology on Dental Implants," in *Emerging Nanotechnologies in Dentistry*, K. Subramani and W. Ahmed, Eds., ed Boston: William Andrew Publishing, 2012, pp. 71-84.

[19]   J. Wei, T. Igarashi, N. Okumori, T. Igarashi, T. Maetani, B. Liu, and M. Yoshinari, "Influence of surface wettability on competitive protein adsorption and initial attachment of osteoblasts", *Biomedical Materials,* vol. 4, pp. 045002-7, 2009.

[20]   Y. Leng, J. Chen, P. Yang, H. Sun, J. Wang, and N. Huang, "The biocompatibility of the tantalum and tantalum oxide films synthesized by pulse metal vacuum arc source deposition", *Nuclear Instruments and Methods in Physics Research Section B: Beam Interactions with Materials and Atoms,* vol. 242, pp. 30-32, 2006.

[21]   W. Yang, Y. Liu, Q. Zhang, Y. Leng, H. Zhou, P. Yang, J. Chen, and N. Huang, "Biomedical response of tantalum oxide films deposited by DC reactive unbalanced magnetron sputtering", *Surface and Coatings Technology,* vol. 201, pp. 8062-8065, 2007.

[22]   T. Miyazaki, H.-M. Kim, T. Kokubo, C. Ohtsuki, H. Kato, and T. Nakamura, "Mechanism of bonelike apatite formation on bioactive tantalum metal in a simulated body fluid", *Biomaterials,* vol. 23, pp. 827-832, 2002.

[23]   B. R. Levine, S. Sporer, R. A. Poggie, C. J. Della Valle, and J. J. Jacobs, "Experimental and clinical performance of porous tantalum in orthopedic surgery", *Biomaterials,* vol. 27, pp. 4671-4681, 2006.

[24]   A. Zeller, A. Musyanovych, M. Kappl, A. Ethirajan, M. Dass, D. Markova, M. Klapper, and K. Landfester, "Nanostructured coatings by adhesion of phosphonated polystyrene particles onto titanium surface for implant material applications", *ACS Applied Materials & Interfaces,* vol. 2, pp. 2421-2428, 2010.

[25]   T. Kokubo, T. Matsushita, H. Takadama, and T. Kizuki, "Development of bioactive materials based on surface chemistry", *Journal of the European Ceramic Society,* vol. 29, pp. 1267-1274, 2009.

[26]   T. Albrektsson and A. Wennerberg, "Oral implant surfaces: Part 1--review focusing on topographic and chemical properties of different surfaces and in vivo responses to them", *The International Journal of Prosthodontics,* vol. 17, pp. 536-543, 2004.

[27]   L. Zhang and T. J. Webster, "Nanotechnology and nanomaterials: promises for improved tissue regeneration", *Nano Today,* vol. 4, pp. 66-80, 2009.

[28]   K. Subramani, D. Tran, and K. Nguyen, "Chapter 8—Cellular Responses to Nanoscale Surface Modifications of Titanium Implants for Dentistry and Bone Tissue Engineering Applications", *Emerging Nanotechnologies in Dentistry, William Andrew Publishing, Boston, MA,* pp. 113-136, 2012.

[29]   E. P. Ivanova, J. Hasan, H. K. Webb, G. Gervinskas, S. Juodkazis, V. K. Truong, A. H. Wu, R. N. Lamb, V. A. Baulin, and G. S. Watson, "Bactericidal activity of black silicon", *Nature communications,* vol. 4, 2013.

[30]   L. Meirelles, "Nanoestruturas e a resposta óssea. Uma alternativa segura para a reabilitação com implantes osseointegráveis?", *Implantnews,* vol. 7, 2010.

[31]   J. Disegi, "Titanium alloys for fracture fixation implants", *Injury,* vol. 31, pp. D14-D17, 2000.

[32]   O. E. Pohler, "Unalloyed titanium for implants in bone surgery", *Injury,* vol. 31, pp. D7-D13, 2000.

[33]   H. Rack and J. Qazi, "Titanium alloys for biomedical applications", *Materials Science and Engineering: C,* vol. 26, pp. 1269-1277, 2006.

[34]   X. Ye, Y. Yang, and G. Tang, "Microhardness and corrosion behavior of surface gradient oxide coating on the titanium alloy strips under high energy electro-pulsing treatment", *Surface and Coatings Technology,* vol. 258, pp. 467-484, 2014.

[35]   X. Ye, L. Wang, Z. T. H. Tse, G. Tang, and G. Song, "Effects of high-energy electro-pulsing treatment on microstructure, mechanical properties and corrosion behavior of Ti–6Al–4V alloy", *Materials Science and Engineering: C,* vol. 49, pp. 851-860, 2015.

[36] E. Rigo, L. Oliveira, L. Santos, R. Carrodéguas, and A. Boschi, "Implantes metálicos recobertos com hidroxiapatita", *Revista Brasileira de Engenharia Biomédica,* vol. 15, pp. 21-29, 1999.

[37] Y. Leng, H. Sun, P. Yang, J. Chen, J. Wang, G. Wan, N. Huang, X. Tian, L. Wang, and P. Chu, "Biomedical properties of tantalum nitride films synthesized by reactive magnetron sputtering", *Thin Solid Films,* vol. 398, pp. 471-475, 2001.

[38] V. K. Balla, S. Banerjee, S. Bose, and A. Bandyopadhyay, "Direct laser processing of a tantalum coating on titanium for bone replacement structures", *Acta Biomaterialia,* vol. 6, pp. 2329-2334, 2010.

[39] N. Wang, H. Li, J. Wang, S. Chen, Y. Ma, and Z. Zhang, "Study on the anticorrosion, biocompatibility, and osteoinductivity of tantalum decorated with tantalum oxide nanotube array films", *ACS Applied Materials & Interfaces,* vol. 4, pp. 4516-4523, 2012.

[40] L. Gladczuk, A. Patel, C. Singh Paur, and M. Sosnowski, "Tantalum films for protective coatings of steel", *Thin Solid Films,* vol. 467, pp. 150-157, 2004.

[41] V. K. Balla, S. Bodhak, S. Bose, and A. Bandyopadhyay, "Porous tantalum structures for bone implants: fabrication, mechanical and in vitro biological properties", *Acta Biomaterialia,* vol. 6, pp. 3349-3359, 2010.

[42] C. J. Frandsen, K. S. Brammer, K. Noh, G. Johnston, and S. Jin, "Tantalum coating on TiO2 nanotubes induces superior rate of matrix mineralization and osteofunctionality in human osteoblasts", *Materials Science and Engineering: C,* vol. 37, pp. 332-341, 2014.

[43] M. Mazur, M. Kalisz, D. Wojcieszak, M. Grobelny, P. Mazur, D. Kaczmarek, and J. Domaradzki, "Determination of structural, mechanical and corrosion properties of Nb2O5 and (NbyCu1 − y)Ox thin films deposited on Ti6Al4V alloy substrates for dental implant applications", *Materials Science and Engineering: C,* vol. 47, pp. 211-221, 2015.

[44] J. C. M. Souza, S. L. Barbosa, E. A. Ariza, M. Henriques, W. Teughels, P. Ponthiaux, J.-P. Celis, and L. A. Rocha, "How do titanium and Ti6Al4V corrode in fluoridated medium as found in the oral cavity? An in vitro study", *Materials Science and Engineering: C,* vol. 47, pp. 384-393, 2015.

[45] S. Maeng, L. Axe, T. Tyson, and P. Cote, "Corrosion behaviour of electrodeposited and sputtered Cr coatings and sputtered Ta coatings with α and β phases", *Surface and Coatings Technology,* vol. 200, pp. 5767-5777, 2006.

[46] S. Maeng, L. Axe, T. Tyson, L. Gladczuk, and M. Sosnowski, "Corrosion behaviour of magnetron sputtered α-and β-Ta coatings on AISI 4340 steel as a function of coating thickness", *Corrosion science,* vol. 48, pp. 2154-2171, 2006.

[47] S. M. Maeng, L. Axe, T. A. Tyson, L. Gladczuk, and M. Sosnowski, "Corrosion behavior of magnetron sputtered α-Ta coatings on smooth and rough steel substrates", *Surface and Coatings Technology,* vol. 200, pp. 5717-5724, 2006.

[48] B. Díaz, J. Światowska, V. Maurice, A. Seyeux, E. Härkönen, M. Ritala, S. Tervakangas, J. Kolehmainen, and P. Marcus, "Tantalum oxide nanocoatings prepared by atomic layer and filtered cathodic arc deposition for corrosion protection of steel: Comparative surface and electrochemical analysis", *Electrochimica Acta,* vol. 90, pp. 232-245, 2013.

[49] Y.-S. Sun, J.-H. Chang, and H.-H. Huang, "Corrosion resistance and biocompatibility of titanium surface coated with amorphous tantalum pentoxide", *Thin Solid Films,* vol. 528, pp. 130-135, 2013.

[50] G. Xu, X. Shen, Y. Hu, P. Ma, and K. Cai, "Fabrication of tantalum oxide layers onto titanium substrates for improved corrosion resistance and cytocompatibility", *Surface and Coatings Technology,* vol. 272, pp. 58-65, 2015.

[51] S. Boughaba, M. Islam, G. Sproule, and M. Graham, "Characterization of tantalum oxide films grown by pulsed laser deposition", *Surface and Coatings Technology,* vol. 120, pp. 757-764, 1999.

[52]   H.-E. Cheng and C.-T. Mao, "The effect of substrate temperature on the physical properties of tantalum oxide thin films grown by reactive radio-frequency sputtering", *Materials Research Bulletin,* vol. 38, pp. 1841-1849, 2003.

[53]   C.-H. Lu and C.-H. Wu, "Low-temperature crystallization of tantalum pentoxide films under elevated pressure", *Journal of the European Ceramic Society,* vol. 26, pp. 2753-2759, 2006.

[54]   M. Chandrasekhar, S. J. Chandra, and S. Uthanna, "Characterization of bias magnetron sputtered tantalum oxide films for capacitors", *Indian Journal of Pure & Applied Physics,* vol. 47, pp. 49-53, 2009.

[55]   C. Arnould, T. Korányi, J. Delhalle, and Z. Mekhalif, "Fabrication of tantalum oxide/carbon nanotubes thin film composite on titanium substrate", *Journal of colloid and Interface Science,* vol. 344, pp. 390-394, 2010.

[56]   J. J. Colin, G. Abadias, A. Michel, and C. Jaouen, "On the origin of the metastable β-Ta phase stabilization in tantalum sputtered thin films", *Acta Materialia,* vol. 126, pp. 481-493, 2017.

[57]   R. Hollerweger, D. Holec, J. Paulitsch, R. Rachbauer, P. Polcik, and P. Mayrhofer, "Magnetic field strength influence on the reactive magnetron sputter deposition of Ta2O5", *Journal of Physics D: Applied Physics,* vol. 46, p. 335203, 2013.

[58]   Z. Pan, Y. Li, and Q. Wei, "Tensile properties of nanocrystalline tantalum from molecular dynamics simulations", *Acta Materialia,* vol. 56, pp. 3470-3480, 2008.

[59]   L. Thijs, M. L. M. Sistiaga, R. Wauthle, Q. Xie, J.-P. Kruth, and J. Van Humbeeck, "Strong morphological and crystallographic texture and resulting yield strength anisotropy in selective laser melted tantalum", *Acta Materialia,* vol. 61, pp. 4657-4668, 2013.

[60]   R. Knepper, B. Stevens, and S. P. Baker, "Effect of oxygen on the thermomechanical behavior of tantalum thin films during the β–α phase transformation", *Journal of applied physics,* vol. 100, pp. 123508-11, 2006.

[61]   N. M. G. Parreira, N. J. M. Carvalho, and A. Cavaleiro, "Synthesis, structural and mechanical characterization of sputtered tungsten oxide coatings", *Thin Solid Films,* vol. 510, pp. 191-196, 2006.

[62]   N. M. G. Parreira, N. J. M. Carvalho, F. Vaz, and A. Cavaleiro, "Mechanical evaluation of unbiased W–O–N coatings deposited by d.c. reactive magnetron sputtering", *Surface and Coatings Technology,* vol. 200, pp. 6511-6516, 2006.

[63]   Y. Zhou, Z. Xie, H. Xiao, P. Hu, and J. He, "Effects of deposition parameters on tantalum films deposited by direct current magnetron sputtering", *Vacuum,* vol. 83, pp. 286-291, 2009.

[64]   Y. Zhou, Z. Xie, H. Xiao, P. Hu, and J. He, "Effects of deposition parameters on tantalum films deposited by direct current magnetron sputtering in Ar–O2 mixture", *Applied Surface Science,* vol. 258, pp. 1699-1703, 2011.

[65]   Y.-N. Wu, L. Li, and H.-P. Cheng, "First-principles studies of Ta2O5 polymorphs", *Physical Review B,* vol. 83, p. 144105, 2011.

[66]   K. Lehovec, "Lattice structure of β-Ta2O5", *Journal of the Less Common Metals,* vol. 7, pp. 397-410, 1964.

[67]   N. C. Stephenson and R. S. Roth, "The crystal structure of the high temperature form of Ta2O5", *Journal of Solid State Chemistry,* vol. 3, pp. 145-153, 1971.

[68]   X. Liu, X. Han, Z. Zhang, L. Ji, and Y. Jiang, "The crystal structure of high temperature phase Ta 2 O 5", *Acta Materialia,* vol. 55, pp. 2385-2396, 2007.

[69]   N. Stephenson and R. Roth, "Structural systematics in the binary system Ta2O5–WO3. V. The structure of the low-temperature form of tantalum oxide L-Ta2O5", *Acta Crystallographica Section B: Structural Crystallography and Crystal Chemistry,* vol. 27, pp. 1037-1044, 1971.

[70]   S. R. Jeon, S. W. Han, and J. W. Park, "Effect of rapid thermal annealing treatment on electrical properties and microstructure of tantalum oxide thin film deposited by plasma-enhanced chemical vapor deposition", *Journal of applied physics,* vol. 77, pp. 5978-5981, 1995.

[71]   R. Hollerweger, D. Holec, J. Paulitsch, M. Bartosik, R. Daniel, R. Rachbauer, P. Polcik, J. Keckes, C. Krywka, and P. Mayrhofer, "Complementary ab initio and X-ray nano-diffraction study of Ta2O5", *arXiv preprint arXiv:1404.4347,* 2014.

[72]   H. A. El-Sayed, H. M. Molero, and V. I. Birss, "The impact of fabrication conditions on the quality of Au nanoparticle arrays on dimpled Ta templates", *Nanotechnology,* vol. 23, p. 435602, 2012.

[73]   S. Minagar, C. C. Berndt, J. Wang, E. Ivanova, and C. Wen, "A review of the application of anodization for the fabrication of nanotubes on metal implant surfaces", *Acta biomaterialia,* vol. 8, pp. 2875-2888, 2012.

[74]   I. Sieber, H. Hildebrand, A. Friedrich, and P. Schmuki, "Initiation of tantalum oxide pores grown on tantalum by potentiodynamic anodic oxidation", *Journal of electroceramics,* vol. 16, pp. 35-39, 2006.

[75]   W. Wei, J. M. Macak, N. K. Shrestha, and P. Schmuki, "Thick self-ordered nanoporous Ta2O5 films with long-range lateral order", *Journal of the Electrochemical Society,* vol. 156, pp. K104-K109, 2009.

[76]   Y. Liu, C. Bao, D. Wismeijer, and G. Wu, "The physicochemical/biological properties of porous tantalum and the potential surface modification techniques to improve its clinical application in dental implantology", *Materials Science and Engineering: C,* vol. 49, pp. 323-329, 2015.

[77]   W. Wei, J. Macak, and P. Schmuki, "High aspect ratio ordered nanoporous Ta2O5 films by anodization of Ta", *Electrochemistry Communications,* vol. 10, pp. 428-432, 2008.

[78]   H. El-Sayed, S. Singh, M. T. Greiner, and P. Kruse, "Formation of highly ordered arrays of dimples on tantalum at the nanoscale", *Nano letters,* vol. 6, pp. 2995-2999, 2006.

[79]   N. K. Allam, X. J. Feng, and C. A. Grimes, "Self-assembled fabrication of vertically oriented Ta2O5 nanotube arrays, and membranes thereof, by one-step tantalum anodization", *Chemistry of Materials,* vol. 20, pp. 6477-6481, 2008.

[80]   J. E. Barton, C. L. Stender, P. Li, and T. W. Odom, "Structural control of anodized tantalum oxide nanotubes", *J. Mater. Chem.,* vol. 19, pp. 4896-4898, 2009.

[81]   H. A. El-Sayed and V. I. Birss, "Controlled interconversion of nanoarray of Ta dimples and high aspect ratio Ta oxide nanotubes", *Nano letters,* vol. 9, pp. 1350-1355, 2009.

[82]   H. A. El-Sayed and V. I. Birss, "Controlled growth and monitoring of tantalum oxide nanostructures", *Nanoscale,* vol. 2, pp. 793-798, 2010.

[83]   L.-N. Wang, M. Jin, Y. Zheng, Y. Guan, X. Lu, and J.-L. Luo, "Nanotubular surface modification of metallic implants via electrochemical anodization technique", *International journal of nanomedicine,* vol. 9, p. 4421, 2014.

[84]   A. Ghicov and P. Schmuki, "Self-ordering electrochemistry: a review on growth and functionality of TiO 2 nanotubes and other self-aligned MO x structures", *Chemical Communications,* pp. 2791-2808, 2009.

[85]   H. El-Sayed, S. Singh, and P. Kruse, "Formation of dimpled tantalum surfaces from electropolishing", *Journal of the Electrochemical Society,* vol. 154, pp. C728-C732, 2007.

Chapter 2

Production and characterization techniques

2.1. Introduction

The chapter 2 is dedicated to the description of the experimental methodologies used in the present thesis. The Ta-based surfaces were produced by two different processes: magnetron sputtering and anodization. A summary of the theoretical background and fundamental concepts regarding both processes is provided. Additionally, a brief description of the different methods and techniques used for surface characterization, including electron probe microanalysis (EPMA), X-ray photoelectron spectroscopy (XPS), X-ray diffraction (XRD), scanning electron microscopy (SEM, scanning transmission electron microscopy (STEM), spectroscopic ellipsometry (SE), among others, is given.

2.2. Tantalum oxides production

2.2.1. Reactive magnetron sputtering

As mentioned, direct current magnetron sputtering (DCMS) is one of the most popular physical vapor deposition (PVD) techniques used in industry [1]. The PVD principle is related with the creation of vapor species from a target material followed by its condensation onto a substrate. In the DCMS method the atoms are sputtered from the target as a consequence of the collision of energetic ions (such as Ar^+ or He^+), which constitutes the plasma.

The sputtering process is based on the application of an electrical field between the cathode (target) and the anode in a non-reactive atmosphere (usually Ar or He) in a low vacuum environment. The electrical field promotes the acceleration of charged particles, including ionized species and secondary electrons (emitted by the target surface during the discharge). The charged species ensure the collision and momentum transference to the target being responsible for the atoms sputtering, as well as, for the secondary electrons emission. The secondary electrons, on the other hand, ensure the ionization of non-reactive species and plasma maintenance [2]. Thus, the sputtered atoms condense onto the substrate surface and then, nucleation and coalescence phenomenon lead to the coating formation. Ar is one of the most used non-reactive gas due to its mass that allows a high momentum transference enhancing the sputtering yield. However, there is a

minimum voltage necessary to create the plasma, known as breakdown voltage, otherwise the non-reactive species do not acquire enough kinetic energy to ionize and create charged particles [3, 4].

Although the sputtering method allows an efficient and uniform ejection of atoms from the target surface, due to the uniform discharge and gas ionization in all target, the ionization and collision rate of Ar in a DC diode system is generally low, revealing low deposition rate and poor films densities. Nonetheless, by applying a magnetic field, perpendicular to the electrical field and parallel to the target surface, it is possible to confine and trap the secondary electrons and thus, the plasma ionization and, subsequently, target sputtering is boosted. The magnetron sputtering system further allows to minimize the electronic bombardment of the substrate holder. Still, due to the helicoidal trajectories of the secondary electrons, caused by the magnetic field, the atoms ejection from the target surface is less effective [2, 5].

Moreover, the bombardment of the substrate holder with secondary electrons leads to a temperature increase in the substrate holder, as well as, atoms re-sputtering from the growing film, creating growth defects. By applying a negative bias voltage to the substrate holder it is possible to minimize the electronic bombardment, as well as, increase the ionic bombardment on the substrates and then, increase the film density [2].

Due to the variety of reactive gases that can be added, reactive DCMS is well known for its versatility and usefulness to deposit a wide range of compounds that would not be possible to deposit by other physical processes. For example, metal oxide coatings with different compositions can be obtained involving only a metallic target and modifying the reactive atmosphere (*i.e.* the ratio between Ar and O_2), which makes the control of the deposition parameters extremely important to optimize the final properties of the films namely chemical state, structure or morphology. One of the main issues during reactive MS is the presence of instabilities that are typically associated with a wrong selection of the experimental parameters. Therefore, voltage hysteresis analyses is a very useful method to understand the influence of the gas flow rate on the glow discharge by the cathode voltage evolution with the increase of reactive gas partial pressure [6].

A typical hysteresis curve exhibits three different zones that correspond to two different deposition modes: i) metallic mode; and ii) reactive mode. Figure 2.1 shows a representation of the phenomena taking place in each deposition mode. In the first one, the deposition occurs with none or low reactive gas flow (Figure 2.1.a). The target surface maintains a metallic character and has associated low discharge voltage. The metal atoms sputtered from the target react with the reactive gas on the substrate surface forming typically sub-stoichiometric compounds (in the case of Ta target, Ta_2O or Ta_4O). On the other hand, when high reactive gas flow is used, the depositions occur in a reactive mode (Figure 2.1.c). This means that the reactivity of the plasma with the metallic target is higher and induces formation of an oxidized layer (such as TaO_2 or Ta_2O_5) over the target surface by chemisorption and/or oxygen implantation. This process is known as "target poisoning" and leads to higher discharge voltages. The increase in target surface reactivity is generally associated with a decrease in the effective secondary electron emission yield (SEEY), which for a constant current density results in a significant direct dependence of the target voltage of the reactive gas flow. At this stage, the sputtering of the oxide layer existing at the surface competes with the sputtering of pure metallic atoms reducing the total sputtering yield. Moreover, the appearance of a new layer over the target surface with ceramic nature contributes to drop the deposition rate.

In between these two described depositions modes, a transition zone with an intermediate behavior arises. In this transition zone, the reactive species can partially react with the sputtered atoms on the substrate surface, on the plasma atmosphere and lastly on the target surface, associated with a progressive increase in the discharge voltage. This zone is highly unstable, which reinforces the appearance of a mixture of phases during film deposition.
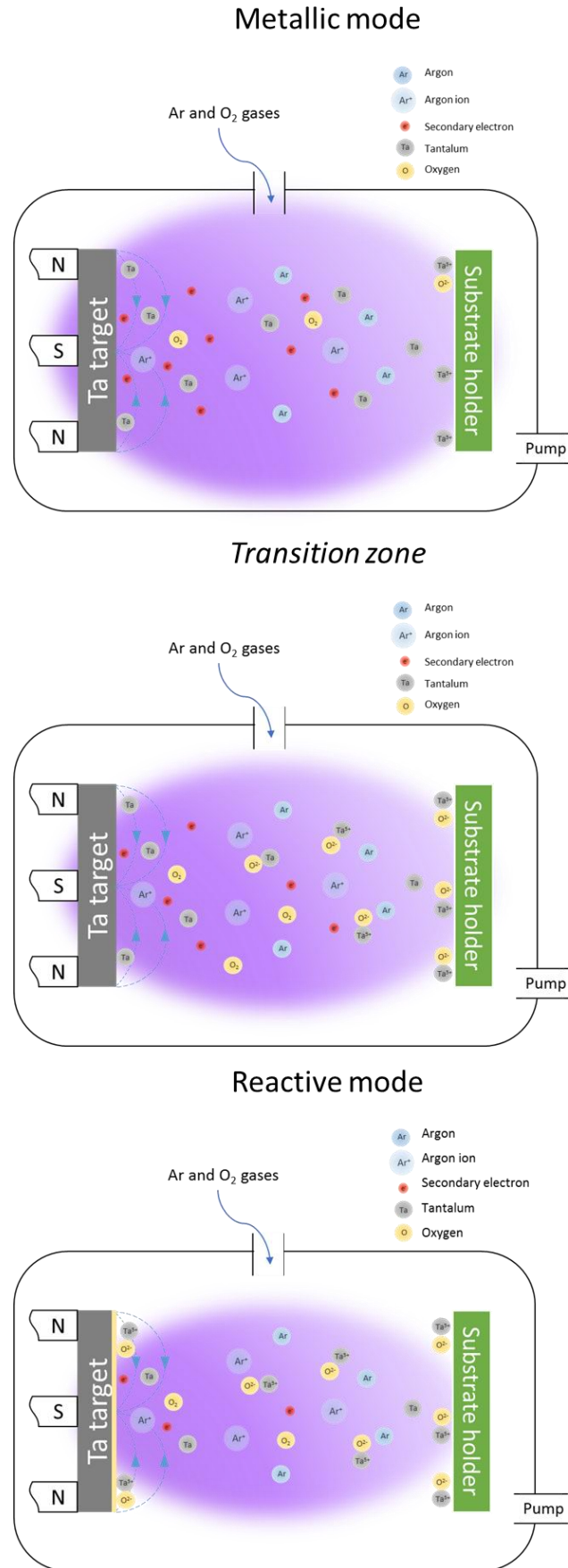
Figure 2.1: Schematic evolution of the sputtering process in an Ar + O$_2$ atmosphere with a metallic target.

2.2.2. Anodization process

Anodization is an electrochemical technique based on a potential application between the anode (working electrode) and the cathode (counter electrode such as lead, carbon, platinum, among others), which causes charge and ion transfer and a subsequently formation of an anodic oxide layer [7]. Thus, a chemical and topographical modification of the material results from anodization process due to the formation of an oxide layer. Depending on the anodization conditions, the process may lead to the formation of a nanostructured layer (pores or nanotubes) [8].

The formation of metal oxide nanostructures can be directly controlled by several parameters, such as the electrolyte composition and concentration, the applied potential, the anodization time and the temperature [9]. Knowing that the anodization is based in the surface oxidation, the electrolyte used in anodization must allow migration of oxygen ions to the metal surface to form the anodic oxide layer [10]. The application of an electric field favors the ionic transport (O_2^- and OH^-) and subsequently the thickness of the oxide layer increases as a function of the anodization time [11]. Thus, the anodization time, at a constant voltage, has a directly influence on the thickness of the oxide layer formed [8]. On the other hand, the increase in the voltage increases the electrons number/flow in the anode, which increase the anodization rate [12].

The electrolytes are in general strong acids, usually H_2SO_4, HF or H_3PO_4. The electrolyte composition and concentration determines the efficiency and velocity of the anodization process. Thus, the electrolyte selection affect the porosity formation and it is specific for each material [13]. Furthermore, the temperature together with the electrolyte concentration is an important variable that allows to control the size of the nanostructures being possible to increase the size with temperature [14].

Pores formation may occur by two main mechanisms: micro arc oxidation or dissolution assisted by electric field. The micro arc oxidation process is characterized by application of high voltages that generates an electric field higher than the electric field that the anodic layer can support, so-called breakdown potential. Reaching the breakdown potential, sparks and discharges within the anodic layer occurs, inducing local temperature increase and hence, crystallization may take place. As consequence, the

sparks creates holes, which promote a disordered porous anodic oxide layer (see as example Figure 2.2.a) [15-17]. On the other hand, dissolution assisted by electric field process is characterized by low voltages coupled with concentrated electrolytes that have the ability to dissolve the anodic oxide layer. The presence of pits on the surface combined with the electric field distribution enhances the localized dissolution towards a steady-state forming a highly ordered nanostructured surface (see Figure 2.2.b) [18, 19].
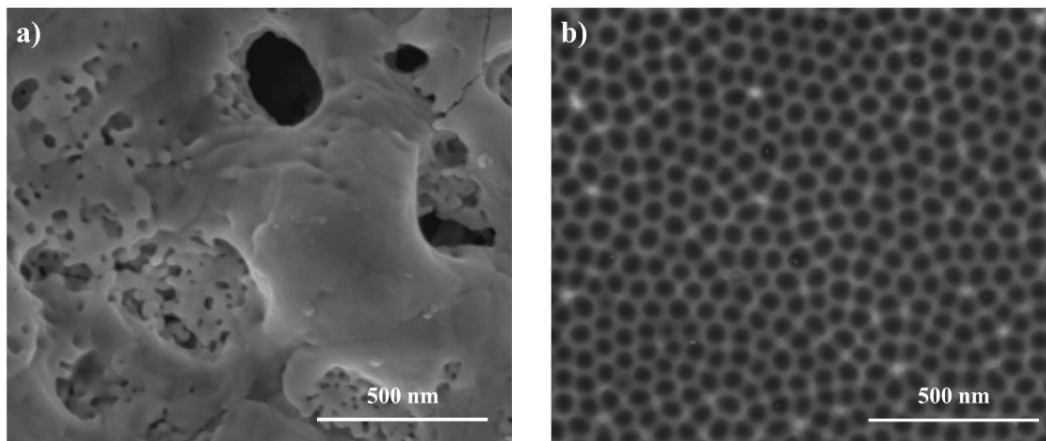
Figure 2.2: (a) SEM micrograph example of a disordered porous anodic oxide layer obtained by anodization at breakdown potential; (b) SEM micrograph example of a highly ordered nanostructured surface obtained by anodization at dissolution assisted by electric field.

Anodization is a chemical process that besides inexpensive, it is reproducible and thus, widely used for nanopatterning biomedical devices, due to the homogeneity, uniformity and high control of the topography obtained. Generically, anodization allows to modify simultaneously the surface chemical composition (formation of an oxide), as well as, the topography (from micro to nano scale).

2.3. Characterization techniques

The developed surfaces were carefully investigated and analyzed through several surface characterization techniques. It is important to note that those surfaces, namely the

coatings, were deposited onto different substrate materials such as SS 316L, Si and glass substrates; thus, the characterization were carried out to ensure that the properties were only marginally affected by the substrate, with no significant differences in the characterization result.

2.3.1. Chemical analysis

2.3.1.1.   Electron Probe Microanalysis (EPMA)

Electron probe microanalysis (EPMA) is a widely used technique for surface characterization providing both qualitative and quantitative chemical element analysis. The physical principle is based on the incidence of a focused electron beam on a sample surface, which emits X-rays specific for each element as a response. This information is analyzed by an energy dispersive (EDS) or a wavelength dispersive (WDS) spectrometers. The determination of the chemical composition is given by the comparison of the obtained spectrum X-rays intensity (dependent on the amount of the chemical element) with the standard elemental chemical intensities provided by the database in the system. EDS apparatus only analyzes the X-rays energies, which may lead to the overlapping of the X-ray energy for more than one chemical element. Differently, WDS configuration uses the X-ray wavelength to identify and quantify the chemical element. Once, the wavelength is specific for each X-ray, which in turn is unique for each element, WDS in known to allow a more accurate quantification [4].

The chemical composition of the first series of $Ta_{1-x}O_x$ coatings was determined by EPMA, using a Cameca equipment: model Camebax SX50. The accelerating voltage of the electron beam was 10 kV and 40 nA of current. Five measurements were performed randomly on each sample to make it statistically reliable. The experimental error of this technique is < 1 atomic (at.) %.

2.3.1.2.   Energy Dispersive Spectroscopy (EDS)

Energy dispersive spectroscopy is a characterization technique for qualitative chemical element analysis. As in EPMA, the X-rays emission from the sample due to the incidence of a focused electron beam allows the quantification of the X-rays energy by the EDS detector. Depending on the atomic orbital where the X-rays come from, X-rays with different energies can be emitted for the same element. From the difference between the background and the peak intensity arises the X-ray energy dispersive spectrum, as represented in Figure 2.3. Despite the chemical element identification, EDS apparatus is recommended to be used as qualitative method due to the possible overlap of the X-ray energy of some elements. Another possibility to improve the analysis is to calibrate the data with an external standard measurement (*e.g.*, from an EPMA measurement). Usually, a EDS system is coupled with some electron microscopes (*e.g.* SEM, FIB, TEM, STEM) to make possible the surface or materials composition analysis in punctual areas at high magnification images [20].
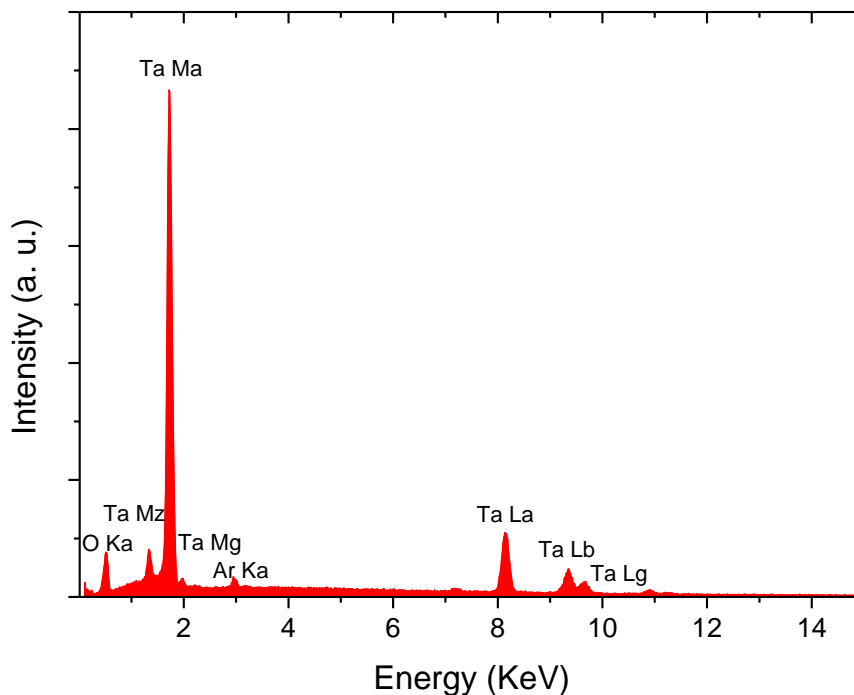
Figure 2.3: Example of an EDS spectrum for a Ta sample.

The chemical composition of the second series of $Ta_{1-x}O_x$ coatings was determined by EDS using a EDAX- Pegasus X4M equipment with an accelerating voltage of 10 kV. Again, five measurements were randomly performed on each sample in order to statistically validate the measurement. Then, the obtained EDS data were calibrated with a measurement given by EPMA composition to make the results accurate.

In specific cases, EDS-mapping was performed in an aberration-corrected FEI Titan ChemiSTEM microscope operating at 200 keV, equipped with a Super-X EDS detector. Iterative maps of 512×512 pixels were recorded with 10 µs of dwell time per pixel at 200 keV, approximately with 400 pA of current and 15 min of collection times.

2.3.1.3.   X-ray Photoelectron Spectroscopy (XPS)

X-ray photoelectron spectroscopy (XPS), is also often known as electron spectroscopy for chemical analysis (ESCA) and belongs to the surface characterization techniques used for quantification of the surface chemical composition, as well as, for identification of the atomic bonding states. The incidence of monoenergetic X-rays (hυ = 1253.6 (MgKα) or 1486.6 (AlKα) eV) on the surface material leads to electron excitation and its consequent emission out from the analyzed material, this phenomenon denominated as photoemission. The specific kinetic energy of the emitted electrons, which is collected by the detector, combined with the X-ray source energy can be described in terms of the binding energy, which in relation can be expressed by the following Equation 2.1.

Equation 2.1

$$K_E = h\upsilon - B_E - \Phi$$

where K_E is the kinetic energy, $h\upsilon$ is the photon energy, B_E is the binding energy of the atomic orbital from where the electrons are generated and Φ is the work function. Considering that the B_E is characteristic for each electron in a specific orbital of a specific atom, the evaluation of the photoelectrons K_E allows the identification of the atoms

present in the material and even assess their chemical state. Furthermore, allows to determine which atoms are chemically bonded. Due to the photon collisions, the photoelectrons are subjected to energy losses limiting the surface thickness analysis to 10 nm for XPS technique [21].

The chemical bond and oxidation state of the the $Ta_{1-x}O_x$ coatings were investigated by XPS analysis using an Isa-Riber setup equipped with a Mac 2 detector. The analysis was performed in an ultrahigh vaccum chamber, which base pressure was kept below 10^{-8} Pa. It was used a monochromatic radiation MgKα (hυ = 1256.3 eV) and the photoelectrons were collected with a take-off angle of 90° from the horizontal plane of sample surface. The energy step was 0.5 eV/s for the survey spectra and 0.2 eV/s for the high-resolution spectra, with an energy pass of 20 eV. Survey scans were recorded in the 50 − 1250 eV energy range to determine the chemical elements presented in the sample and to find out possible surface contamination. Then O 1s, Ta 4f and C 1s photoelectron peaks that were separately recorded (to avoid charging effect). Each spectrum was recorded between 10 and 20 times and then the average value was calculated.

XPS analysis was also performed to understand of the protection mechanism during the corrosion tests, using a Kratos AXIS Ultra HSA, with a VISION software for data acquisition. The analysis was carried out with a monochromatic AlKα X-ray radiation source (hυ = 1486.7 eV), operating at 15 kV (150 W), in FAT mode (fixed analyzer transmission), with a pass energy of 40 eV for regions ROI and 80 eV for survey. The data acquisition was performed with a pressure lower than 1×10^{-6} Pa and a charge neutralization system was used.

The obtained XPS data was analyzed (curve fitting by peak deconvolution and calculation of peak areas) using a standard XPS software (Casa XPS). The electrical charge effect was corrected by the reference of the carbon peak at 285.0 eV. A Gaussian-Lorentzian (GL) product with 70% Gaussian contribution was used to better fit the peaks, considering the respective atomic relative sensitive factors (RSF), using a common Shirley background.

2.3.1.4.   Fourier Transform Infrared Spectroscopy (FTIR)

This is a non-destructive technique based on the molecules vibration, which provides information about the chemical bonding of the sample. If an infrared radiation goes through the solid material, the molecules start to rotate or vibrate (see Figure 2.4) at a specific frequency, this feature is dependent on the type of material and on the specific binding state associated. Additionally, the analysis of the spectrum profile can contribute to qualitatively evaluate the optical character of the irradiated material. The results can be acquired in different modes: (i) absorption, which allows to quantify the concentration; or (ii) transmission or reflection, which allow to obtain qualitative information about the chemical bonds [22, 23].
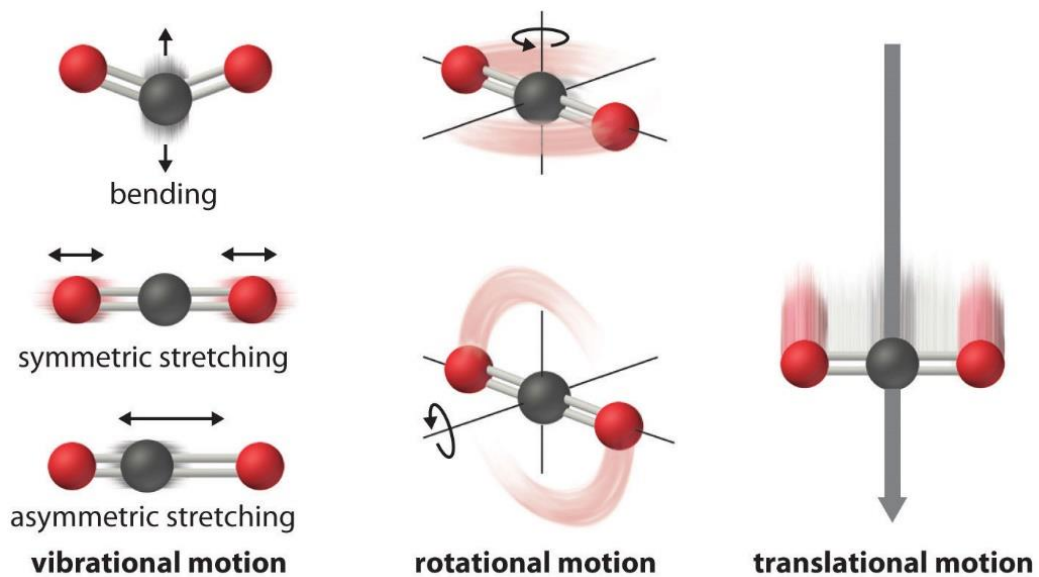
Figure 2.4: Molecules vibrations caused by the infrared radiation, which can be detected by FTIR technique [23].

The chemical bonding configuration of the coatings was evaluated by a reflectance FTIR using a Bruker Tensor 27 spectrometer in a wavenumber range operating from 400 to 1400 cm^{-1}. References intensity were performed before each single measurement by recording the direct intensity I0 for transmission and reflectance measurement on a thick gold film (98.5% of beam reflection).

2.3.1. Phase composition: X-ray Diffraction (XRD)

The evaluation of the crystalline structure of materials is often performed by the X-ray diffraction (XRD) method, which uses a radiation wavelength similar to the interatomic distance. The principle is based on the X-rays incidence at a certain angle (θ) in relation to the material surface, and hence, parallel crystallographic planes in the material cause the diffraction of the incident radiation with an angle (2θ) between the incident and diffracted photons. In a crystalline material, the atoms are ordered and the radiation suffers a constructive interference while, when the atoms are randomly organized the radiation intensity is annulled suffering destructive interference. Figure 2.5 shows a schema of the interaction of the X-ray radiation with the material and the photon pathways caused by the respective interferences [24].
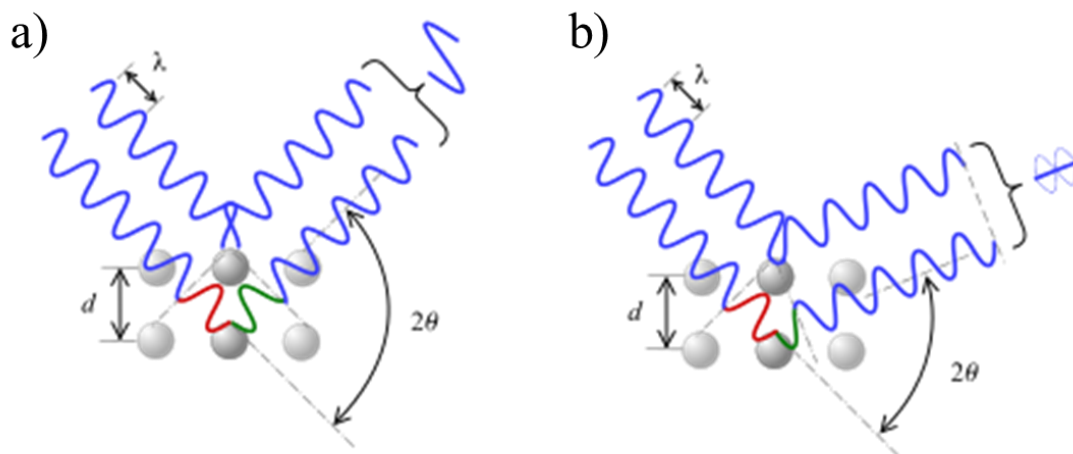
Figure 2.5: Interaction of the X-ray with the material: (a) constructive interference; (b) destructive interference.

The structure of the samples was studied by X-ray diffraction (XRD) using a Bruker D8 Discover, operating at 40 kV and 40 mA with a Cu radiation ($\lambda k_{\alpha 1}$ = 0.1540600 nm and $\lambda k_{\alpha 2}$ = 0.1544339 nm) equipped with a collimator. The acquisition data were performed in Bragg-Brentano and grazing angle configurations with a step size of 0.02° and 1 s per step. The diffractometer is also equipped with an Anton Paar heating chamber, which allows *in-situ* annealing up to 900 °C under air atmosphere. The θ–2θ spectra were acquired at each 100 °C of temperature increase, being 1 °C/s the heating/cooling rates.

2.3.2. Morphology assessment

2.3.2.1. Scanning Electron Microscopy (SEM)

Scanning electron microscopy (SEM) is one of the most used characterization technique in surface engineering applications. The principle is based on the focused electron beam incidence over the sample surface, which may cause numerous types of interactions such as elastic interactions with the atomic electrons and elastic collisions with the atomic nucleus (see Figure 2.6). For example, secondary electrons (SE) emission arise from the elastic interaction of the focused electron beam with the electrons in the material. The SE emission promote an electronic transition of one electron from a higher energy level, emitting an X-ray. For electrons from deeper energy levels the SE emission energy is lower thus, the signal for SE detection mainly comes from the top surface layer (until around 10 nm thickness), giving information about both the morphology and topography of the samples. Besides this, the elastic collisions between the electron beam and the atomic nucleus contribute to an energy conservation leading to the emission of backscattered electrons (BSE), which emission is strongly influenced by the atomic number (Z) of the specimen. Then, for deep depths information about the atomic contrast is also reached [22, 25]. Coupled with the SEM microscope, electron backscatter diffraction (EBSD) is a technique that allows the study of the microstructural-crystallographic features of a polycrystalline material. From the interaction of the focused electron beam with the material arises some scattered electrons. Some of these electrons exit the sample at a certain angle and accomplish the Bragg condition similarly to the XRD diffraction technique. Thus, texture, grain defects, morphology and deformation can be evaluated [20].
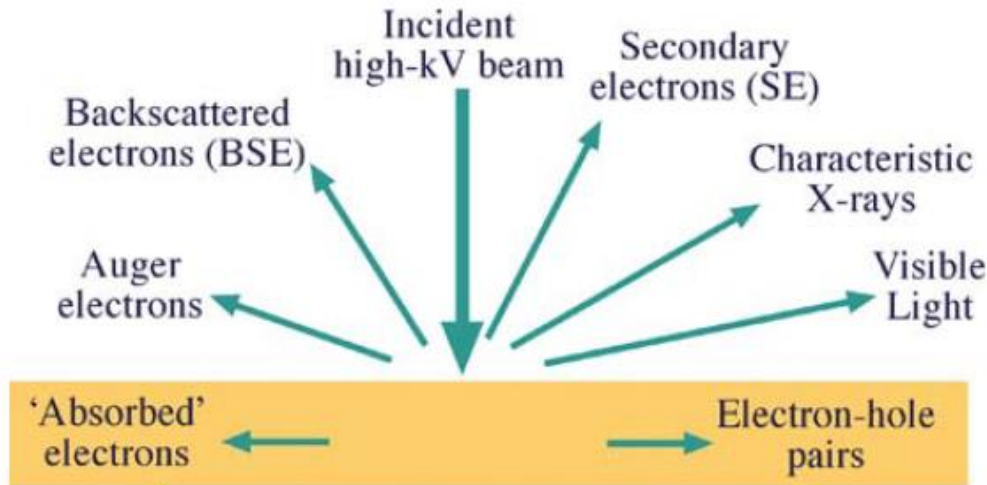
Figure 2.6: Materials signals generated from the focused electron beam incidence, adapted from [26].

Cross section morphology and thickness of the samples were assessed by SEM using a NanoSEM – FEI Nova 200 operating between 5 - 10 keV in secondary electron mode.

In a specific case, texturing analysis was performed by a SEM – EBSD using a FEI Quanta 400FEG ESEM operating at 15 keV at 75°.

2.3.2.2. Transmission Electron Microscopy (TEM) and Scanning Transmission Electron Microscopy (STEM)

Scanning transmission electron microscopy (STEM) is a powerful technique used nowadays once it combines the benefits of transmission electron microscopy (TEM) with the advantages of scanning electron microscopy (SEM). In a conventional TEM, the images are formed by passing a parallel-aligned electron beam through a very thin specimen. On the other hand, with STEM it is possible to focus a very narrow electron spot on a very thin sample, and hence, a fine scanning of the transmitted electrons through the specimen can be performed, allowing an integrative image of each scanned point/spot. The scanning of the transmitted beam across the specimen makes STEM a suitable technique to analyze Z-contrast point by point in the samples. For instance, high-angle annular dark-field (HAADF) STEM is a method widely used because only the elastic scattered electrons are detected while the direct transmitted beam is avoided (see Figure 2.7), thus enhancing the mass contrast.
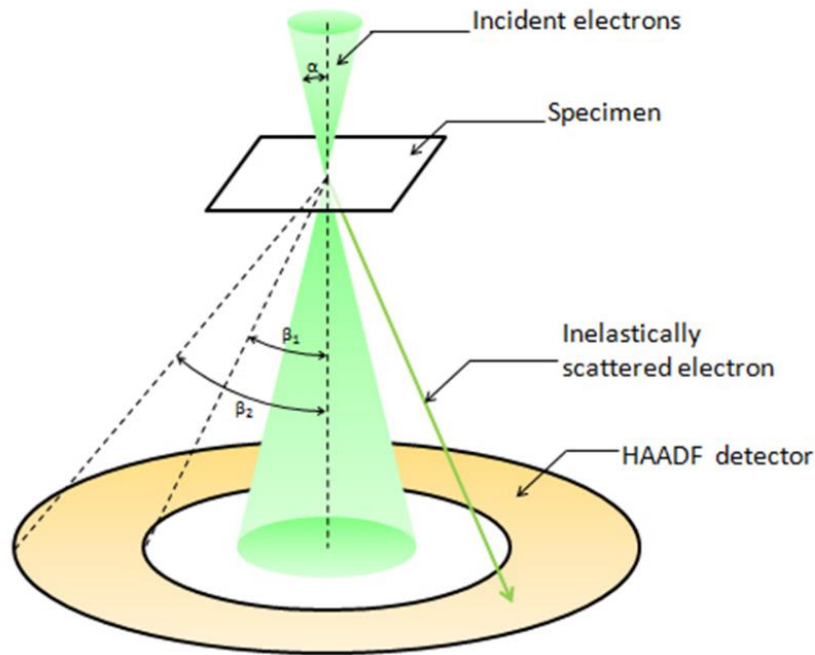
Figure 2.7: Representation of the transmission microscope configuration in HAADF STEM mode [27].

Nevertheless, only very thin samples can be analyzed by STEM characterization technique. Considering that the electron beam needs to be completely transmitted through the sample, the mean free path of the elastic scattered electrons is dependent of the specimen molecular weight. For materials that present on their composition chemical elements with high atomic number, the mean free path of the specimen will be lower, and thus, it needs to be compensated with a lower thickness [26, 27].

In this work, HAADF STEM images were acquired on an aberration-corrected FEI Titan ChemiSTEM microscope operated at 200 keV. The images were recorded using a convergence angle of 21 mrad with a pixel dwell time set at 10 µs. It was selected a camera length of 135 mm, collecting electrons between 56 and 200 mrad.

2.3.2.3.   Focused Ion Beam (FIB)

Focused ion beam (FIB) technique is a method that allows the preparation of a thin sample from a bulk sample which in turn can be characterized through electron transmission techniques. The focused ion beam (commonly composed by Ga^+ ions) can be operated at low or at high currents for morphological imaging or sample milling, respectively. In the specific case of TEM/STEM sample preparation, high currents are applied in order to precisely cut and prepare a very thin lamella (thickness <100 nm), as shown in Figure 2.8.
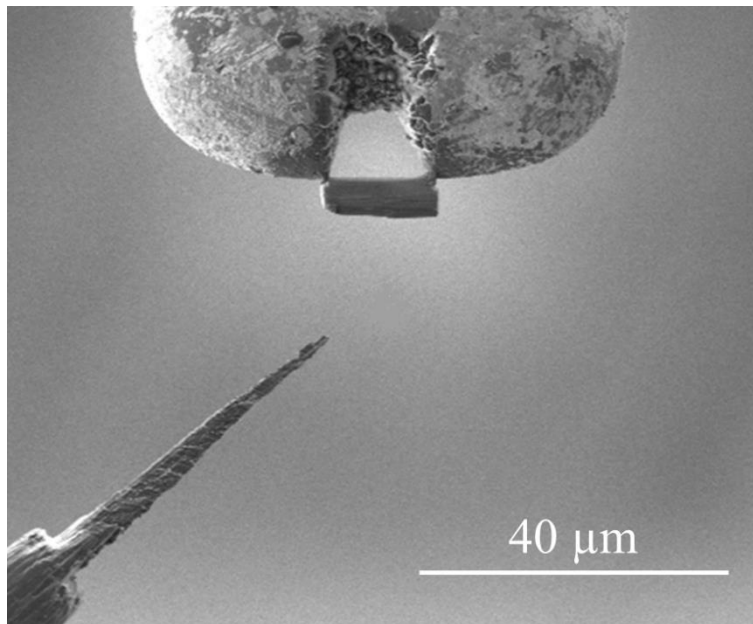
Figure 2.8: Example of a FIB sample.

TEM/STEM sample preparation by FIB method is composed by a set of several milling steps, starting from the bulk material until reaching a lamella (thickness ≈2 μm). Thereafter, the lamella is thinned to attain the desired thickness. It must be stressed that it is critical to decrease both the ion current and the beam size (spot size) to minimize the damage and improve the cut precision once the lamella is very thin. Additionally, to prevent lamella damage during the thinning process, the bulk surface is usually covered with a protective layer (usually Platinum - Pt).

TEM and STEM samples were prepared by FIB using a Helios 450S (FEI) - Dual FIB with UHRSEM.

2.3.2.4.   Atomic Force Microscopy (AFM)

Atomic force microscopy (AFM) is a characterization technique used to evaluate the topography of the material's surface. It uses a microfabricated piezoelectric cantilever to measure the interatomic forces between the surface atoms and the cantilever tip. Depending on the magnitude of the tunneling current or on the cantilever deflection, magnitude that depends on the distance between the surface and the tip, it is possible to measure the surface height with atomic resolution in the three directions, and then mapping the surface topography [22].

The surface scanning may occur in two basic modes: contact or tapping, as demonstrated in Figure 2.9. The difference between the two modes is on the distance between the surface and the cantilever tip. In contact mode, the tip is in permanent contact with the surface and then, by applying a constant force, the tunneling current is measured. Oppositely, in tapping mode the tip is driven to oscillate at a certain distance from the sample surface and then, the cantilever deflection needed to keep the tunneling current constant is measured, that deflection strongly depends on the repulsive/attractive forces. Both approaches allow to determine the surface topography, although, contact mode is recommended to be used in materials with low roughness or hard materials due to the applied force, while tapping mode is recommend to be used in materials with high roughness or soft materials in order to not induce deformation on the asperities [28, 25]. peakforce tapping is an alternative methodology that arise as Bruker property. In peakforce tapping mode, the tip is in permanent contact with the surface but the applied force varies along the topography roughness. In this sense, it is possible to maximize the resolution without compromise the surface integrity.
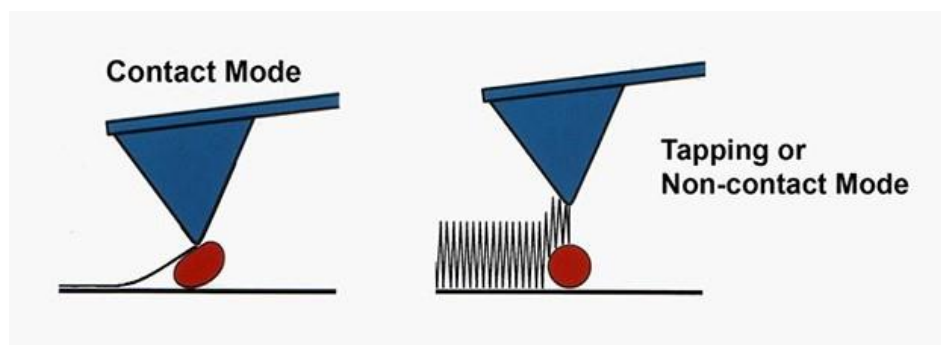
Figure 2.9: Schematic representation of the contact and tapping mode of AFM, adapted from [28].

The surface topography was evaluated by AFM using NanoScopeIII model from Digital Instruments operating in tapping mode for the $Ta_{1-x}O_x$ coatings; and an Icon Dimension with ScanAsyst model from Bruker operating in peakforce tapping for the anodized surfaces. The recorded AFM images were acquired over scanning areas of 5x5 μm^2 and each sample was analyzed at least three different regions.

2.3.3. Optical properties: Spectroscopic ellipsometry (SE)

Ellipsometry is an optical characterization technique that has become widely used for coatings and surfaces due to the progression on both the data acquisition and processing. The method is based on the analysis of the polarized light that is refracted by the sample. In detail, a collimated polarized light beam is focused on the sample with a controlled incidence angle and wavelength. As a result of the interaction between the beam light and the material, some part of the light is reflected and some part travels inside in the sample [22]. The incident light is refracted by the material with an elliptical form according to the well-known Snell's Law [29]. The oscillation curve shape depends on the material' properties and needs to be simulated by an optical model, which describes the optical properties of the material. The amplitude of these oscillations allows the modulation and estimation of the refractive index and the extinction coefficient as well. Furthermore, the thickness, the roughness, the density, the material microstructure and other materials' properties can also be obtained from the ellipsometry measurements [22, 29].

The optical properties of the coatings were evaluated by spectroscopic ellipsometry (SE) using a Jobin-Yvon UVISEL DH10 ellipsometer with a wide spectral range between 1.5 and 5 eV with an incidence angle of 70°. Tauc-Lorentz (TL) dispersion function was used to fit the data and then extrapolate the optical properties and thickness of the coatings [30].

2.3.4. Elastic properties

2.3.4.1. Surface Acoustic Waves (SAW)

The elastic modulus may be measured by the laser-acoustic (LA) wave method which is based on surface acoustic waves (SAW). This technique uses short laser pulses (laser wavelength: 337 nm, pulse length: 3 ns, pulse energy: 80 μJ) focused into a line that create wide-band surface acoustic waves that are detected by a piezoelectric transducer. On its turn, the transducer transforms the mechanical waveform into an electrical signal. Signals are detected at different distances between the laser focus line and the transducer. They are recorded by an oscilloscope and Fourier-transformed, yielding the amplitude and the phase spectra of the waveforms. With the phase spectra of the waveforms, the phase velocity can be calculated for all frequencies included in the waveform spectrum. This signal processing yields the dispersion curve that is fitted afterwards by the theory to calculate the material parameters [31].

The results of the elastic modulus presented are the average of six SAW measurements of the elastic properties of $Ta_{1-x}O_x$ coatings, deposited onto Si substrates. The Poisson ratio (0.34) was kept constant in all measurements.

2.3.4.1. *Ab-initio* Density Functional Theory Calculations (*DFT*)

The structural and mechanical calculations reported herein were based on density functional theory (*DFT*) calculations employing the generalized gradient approximation (GGA) parametrized by Perdew, Burke, and Ernzerhof (PBE) [32] and the projector-augmented-wave method, as implemented in VASP code [33]. The core electrons were frozen within the Projector Augmented Wave (PAW) method [34, 35], whereas valence electrons ($Ta:5p_65d_36s_2$; $O:2s_22p_4$) were treated explicitly by a plane wave basis set with a cutoff energy of 520 eV for structural optimizations and 700 eV for elastic constants calculations. Surface Brillouin-zone integration was performed on a Monkhorst-Pack [36] k mesh of 20×20×20 in the Methfessel-Paxton scheme [37] for Ta, TaO, Ta_2O, Ta_4O crystal structures, and 2×4×4 mesh for Ta_6O, with a smearing width of 0.2 eV for the Fermi-surface broadening. In the case of TaO_2, (β, δ)-Ta_2O_5 structures, the tetrahedron method

with Blochl corrections was used with a k-mesh of 2×4×2 for δ-Ta_2O_5 and 12×12×14 for the other structures [38]. The total energies were converged to better than 1 meV. The equilibrium lattice constants for different Ta_2O_5 structures were obtained through total energy minimization. The force tolerance for geometry relaxation was 0.01 eV/A°.

The material density, formation enthalpy, and elastic properties of α-Ta (ICCD card n. 00-004-0788), β-Ta (ICCD card n. 00-025-1280), Ta_2O (ICCD card n. 01-074-2305), Ta_4O (ICCD card n. 03-065-6450), Ta_6O (ICCD card n. 01-071-5369), TaO (ICCD card n. 01-072-2740), TaO_2 (ICCD card n. 01-019-1297), β-Ta_2O_5 (ICCD card n. 00-025-0922) and δ-Ta_2O_5 (ICDD card n. 03-065-5464) [39] phases were calculated to study the evolution of the structural and elastic properties of the system with increased oxygen content. The formation enthalpy was calculated by Equation 2.2,

Equation 2.2

$$E_f = E_{TaO_x} - E_{Ta} - \left(\frac{x}{2}\right).E_{O_2}$$

where E_{Ta}, E_{O2} and E_{TaOx} are the total energies of bcc Ta, molecular O_2 and TaO_x crystal structures, respectively. In this calculation, the correction to O_2 total energy proposed by Wang was added [40].

The amorphous structures were generated using first-principles molecular dynamics simulations with the VASP code, starting from the crystalline structure of δ-Ta_2O_5 with a supercell containing 112 atoms and with the Brillouin zone sampled at the Γ point. The cell was annealed at a temperature of 3500 K using a Nosé-Hoover thermostat [41] followed by a quenching step down to 1000 K below the theoretical melting point. Finally, a damped molecular dynamic run was performed to optimize the structural geometry. The melt and quench procedure was carried out with various annealing times (12 ps and 20 ps) and cooling rates (300 K/ps and 200 K/ps) to generate four amorphous cells under different annealing and cooling conditions.

2.4. References

[1]   M. Chandrasekhar, S. J. Chandra, and S. Uthanna, "Characterization of bias magnetron sputtered tantalum oxide films for capacitors", *Indian Journal of Pure & Applied Physics,* vol. 47, pp. 49-53, 2009.

[2]   S. Carvalho, "Propriedades mecânicas e características microestruturais de filmes finos nanocompósitos de (Ti,Al,Si)N preparados por pulverização catódica em magnetrão", PhD in Physics, University of Minho, Braga, Portugal, 2004.

[3]   K. Wasa and S. Hayakawa, "Handbook of sputter deposition technology", 1992.

[4]   N. K. A. d. S. Manninen, "Silver segregation in Ag/a-C nanocomposite coatings for potential application as antibacterial surfaces", PhD in Mechanical Engineering, University of Coimbra, Coimbra, Portugal, 2015.

[5]   S. C. Velasco, "Production and characterization of ZrCN-Ag coatings deposited by magnetron sputtering", PhD in Materials Engineering, University of Minho, Braga, Portugal, 2016.

[6]   R. Hollerweger, D. Holec, J. Paulitsch, R. Rachbauer, P. Polcik, and P. Mayrhofer, "Magnetic field strength influence on the reactive magnetron sputter deposition of Ta_2O_5", *Journal of Physics D: Applied Physics,* vol. 46, p. 335203, 2013.

[7]   S. Minagar, C. C. Berndt, J. Wang, E. Ivanova, and C. Wen, "A review of the application of anodization for the fabrication of nanotubes on metal implant surfaces", *Acta biomaterialia,* vol. 8, pp. 2875-2888, 2012.

[8]   S. E. Kim, J. H. Lim, S. C. Lee, S.-C. Nam, H.-G. Kang, and J. Choi, "Anodically nanostructured titanium oxides for implant applications", *Electrochimica Acta,* vol. 53, pp. 4846-4851, 2008.

[9]   I. Sieber, H. Hildebrand, A. Friedrich, and P. Schmuki, "Initiation of tantalum oxide pores grown on tantalum by potentiodynamic anodic oxidation", *Journal of electroceramics,* vol. 16, pp. 35-39, 2006.

[10]   H. El-Sayed, S. Singh, M. T. Greiner, and P. Kruse, "Formation of highly ordered arrays of dimples on tantalum at the nanoscale", *Nano letters,* vol. 6, pp. 2995-2999, 2006.

[11]   H. A. El-Sayed and V. I. Birss, "Controlled growth and monitoring of tantalum oxide nanostructures", *Nanoscale,* vol. 2, pp. 793-798, 2010.

[12]   J. T. Filho, "Modificação superficial de Titânio para a produção de implantes", Mestrado em Ciências em Engenharia Metalúrgica e de Materiais, Universidade Federal do Rio de Janeiro, Rio de Janeiro, Brasil, 2007.

[13]   N. K. Allam, X. J. Feng, and C. A. Grimes, "Self-assembled fabrication of vertically oriented Ta_2O_5 nanotube arrays, and membranes thereof, by one-step tantalum anodization", *Chemistry of Materials,* vol. 20, pp. 6477-6481, 2008.

[14]   Q. Lu, S. Mato, P. Skeldon, G. Thompson, D. Masheder, H. Habazaki, and K. Shimizu, "Anodic film growth on tantalum in dilute phosphoric acid solution at 20 and 85ºC", *Electrochimica Acta,* vol. 47, pp. 2761-2767, 2002.

[15]   M. V. Diamanti and M. P. Pedeferri, "Effect of anodic oxidation parameters on the titanium oxides formation", *Corrosion science,* vol. 49, pp. 939-948, 2007.

[16]   N. K. Kuromoto, R. A. Simão, and G. A. Soares, "Titanium oxide films produced on commercially pure titanium by anodic oxidation with different voltages", *Materials Characterization,* vol. 58, pp. 114-121, 2007.

[17]   F. G. Oliveira, A. R. Ribeiro, G. Perez, B. S. Archanjo, C. P. Gouvea, J. R. Araújo, A. P. Campos, A. Kuznetsov, C. M. Almeida, and M. M. Maru, "Understanding growth mechanisms and tribocorrosion behaviour of porous TiO_2 anodic films containing calcium, phosphorous and magnesium", *Applied surface science,* vol. 341, pp. 1-12, 2015.

[18]   A. Ghicov and P. Schmuki, "Self-ordering electrochemistry: a review on growth and functionality of TiO 2 nanotubes and other self-aligned MO x structures", *Chemical Communications,* pp. 2791-2808, 2009.

[19]   L.-N. Wang, M. Jin, Y. Zheng, Y. Guan, X. Lu, and J.-L. Luo, "Nanotubular surface modification of metallic implants via electrochemical anodization technique", *International journal of nanomedicine,* vol. 9, p. 4421, 2014.

[20]   G. Cao, *Nanostructures and nanomaterials: synthesis, properties and applications*: World Scientific, 2004.

[21]   C. D. Wagner, *Handbook of X-ray photoelectron spectroscopy*: Perkin-Elmer, 1979.

[22]   C. R. Brundle and C. A. Evans, *Encyclopedia of materials characterization: surfaces, interfaces, thin films*: Gulf Professional Publishing, 1992.

[23]   M. Silberberg, *Principles of general chemistry*: McGraw-Hill Higher Education, 2012.

[24]   B. D. Cullity and J. W. Weymouth, "Elements of X-ray Diffraction", *American Journal of Physics,* vol. 25, pp. 394-395, 1957.

[25]   M. Ohring, *Materials science of thin films*: Academic Press 2001.

[26]   M. Tanaka. (27/10/2017). *high-angle annular dark-field scanning transmission electron microscopy*. Available: https://www.jeol.co.jp/en/words/emterms/search_result.html?keyword=HAADF-STEM

[27]   D. B. Williams, C. B. Carter, and P. Veyssiere, *Transmission electron microscopy: a textbook for materials science* vol. 10: Springer, 1998.

[28]   (27/10/2017). *Atomic Force Microscopy*. Available: https://ccem.mcmaster.ca/atomic-force-microscope/

[29]   P. M. Martin, *Handbook of deposition technologies for films and coatings: science, applications and technology*: William Andrew, 2009.

[30]   L. Pereira, H. Aguas, E. Fortunato, and R. Martins, "Nanostructure characterization of high k materials by spectroscopic ellipsometry", *Applied surface science,* vol. 253, pp. 339-343, 2006.

[31]   D. Schneider and T. Schwarz, "A photoacoustic method for characterising thin films", *Surface and Coatings Technology,* vol. 91, pp. 136-146, 1997.

[32]   J. P. Perdew, K. Burke, and M. Ernzerhof, "Generalized gradient approximation made simple", *Physical review letters,* vol. 77, p. 3865, 1996.

[33]   G. Kresse and J. Furthmüller, "Efficient iterative schemes for ab initio total-energy calculations using a plane-wave basis set", *Physical Review B,* vol. 54, p. 11169, 1996.

[34]   P. E. Blöchl, "Projector augmented-wave method", *Physical Review B,* vol. 50, p. 17953, 1994.

[35]   G. Kresse and D. Joubert, "From ultrasoft pseudopotentials to the projector augmented-wave method", *Physical Review B,* vol. 59, p. 1758, 1999.

[36]   H. J. Monkhorst and J. D. Pack, "Special points for Brillouin-zone integrations", *Physical Review B,* vol. 13, p. 5188, 1976.

[37]   M. Methfessel and A. Paxton, "High-precision sampling for Brillouin-zone integration in metals", *Physical Review B,* vol. 40, p. 3616, 1989.

[38]   P. E. Blöchl, O. Jepsen, and O. K. Andersen, "Improved tetrahedron method for Brillouin-zone integrations", *Physical Review B,* vol. 49, p. 16223, 1994.

[39]   Z. Helali, M. Calatayud, and C. Minot, "Novel Delta-Ta2O5 structure obtained from DFT calculations", *The Journal of Physical Chemistry C,* vol. 118, pp. 13652-13658, 2014.

[40]   L. Wang, T. Maxisch, and G. Ceder, "Oxidation energies of transition metal oxides within the GGA+ U framework", *Physical Review B,* vol. 73, p. 195107, 2006.

[41]   W. G. Hoover, "Canonical dynamics: equilibrium phase-space distributions", *Physical review A,* vol. 31, p. 1695, 1985.

Chapter 3

Tantalum oxides deposited by magnetron sputtering

Cristiana Filipa Almeida Alves

The following chapter is partially based on the results published in:

- C. F. Almeida Alves, C. Mansilla, L. Pereira, F. Paumier, Th. Gierardeau and S. Carvalho "*Influence of magnetron sputtering conditions on the chemical bonding, structural, morphological and optical behavior of Ta$_{1-x}$O$_x$ coatings*", Surface and Coatings Technology, 334 (2018) 105-115.

- C. F. Almeida Alves, L. S. Marques, S. Calderon V., P. Ferreira, D. Shneider, A. Cavaleiro and S. Carvalho "*A detailed insight on the relationship between the crystal structure and the elastic properties of Ta$_{1-x}$O$_x$ coatings*", Acta Materiallia, 2017 (submitted).

Cristiana Filipa Almeida Alves

3.1.   Introduction

Nowadays, dental implants are usually fabricated using Ti based materials due to its biocompatibility and strong corrosion resistance [1]. Ti6Al4V is the most common alloy for this application due to its higher corrosion resistance [2, 3]. However, the low ability to form a strong chemical bond with living tissue, known as bioactivity, is a significant limitation for Ti-based materials [4, 5]. Currently, Ta is proposed as an alternative to replace Ti. Ta is a bioactive element presenting interesting wettability and surface free energy which promotes osseointegration and good corrosion resistance [6-9]. The superior surface free energy of TaO_x stimulates the regeneration process in living tissues, and thus, increases the efficiency of osseointegration [6, 10-12]. Moreover, TaO_x enhances the corrosion resistance due to its high chemical stability [13-15].

On this context, this chapter provides a further insight on the influence of oxygen partial pressure at different current densities on the chemical state, structure, morphology and optical properties of $Ta_{1-x}O_x$ coatings deposited by DCMS, with increasing oxygen contents up to the stoichiometric Ta_2O_5.

3.2.   Materials and methods

$Ta_{1-x}O_x$ coatings were deposited by reactive DC magnetron sputtering from a high-purity Ta target (99.6% Ta) (200×100 mm^2) onto polished stainless steel 316L (SS 316L) (20×20 mm^2) (Annex I), single crystalline silicon (Si) (100) (10×10 mm^2) with a native oxide layer of ≈3 nm and glass. The SS 316L substrates were grinded using emery paper from 600 to 2400 grit and then mirror polished with a diamond solution attaining a final surface roughness (Ra) <3 nm. The substrates were ultrasonically cleaned in distilled water, ethanol and acetone during 10 min in each solvent.

The depositions were carried out with the substrates rotating at 70 mm from the target at constant speed of 7 rpm to improve thickness homogeneity. The deposition temperature was kept constant at approximately 200 °C.

Prior to coatings deposition, the substrates were sputter-etched for 15 min. in Ar atmosphere (1.2 Pa) at constant current density (J_{Ta}) of 0.5 mA/cm^2 applied to Ta target and by applying a current of 500 mA to the substrate holder. This procedure allowed to eliminate remaining impurities present on the target and substrates surface, as well as, to remove surface oxides.

A Ta interlayer of around 300 nm was deposited before each Ta$_{1-x}$O$_x$ coating to further improve the adhesion to the substrate. The interlayer was deposited by applying a current density of 10 mA/cm^2 in Ar atmosphere (0.6 Pa) at constant bias voltage of -75 V. Two series of samples were deposited (see Table 3.1): first series with high current density (10 mA/cm^2) aiming higher deposition rates; and a second series with low current density (2.5 mA/cm^2) to promote target poisoning and deposition in a reactive mode. Moreover, an intermediate deposition condition was studied into first series by decreasing the current density from 10 to 5 mA/cm^2 in a tentative to achieve a reactive deposition mode but still with a relatively high deposition rate (see Table 3.1). It is important to pointed out that a second interlayer of Ta oxide ($\approx$200 nm) was deposited in the coatings obtained in the reactive regime (TO16 and TO19) to further enhance the adhesion and create a gradient of oxygen concentration thus, preventing coatings delamination.

The chamber temperature and bias voltage were kept constant at approximately 200 °C and -75 V, respectively. The chamber base pressure in the range of 6×10^{-4} Pa while the working pressure (Ar + O$_2$) was varied from 4×10^{-1} to 7×10^{-1} Pa allowing to create a proper reactive atmosphere to deposit the Ta$_{1-x}$O$_x$ coatings.

Table 3.1: Chemical composition, deposition parameters and deposition rate of the deposited samples.

Sample	Chemical composition (at.%)		O₂ Flow (sccm)	Current density (mA/cm²)	Target potential (V)	Deposition rate (µm/h)
	Ta	O				
Ta1	95 ± 0.3	5 ± 0.3	0		425 ± 20	2.3
TO1	89 ± 0.6	11 ± 0.6	2		352 ± 25	2.1
TO3	73 ± 0.2	27 ± 0.2	6	10	366 ± 3.1	2.3
TO5	57 ± 0.2	43 ± 0.2	10		419 ± 3.3	2.8
TO6	*30 ± 0.4*	*70 ± 0.4*	*13*	*5*	*548 ± 8.4*	*1.9*
Ta6	93 ± 0.4	7 ± 0.4	0		274 ± 5.3	0.32
TO14	38 ± 0.6	62 ± 0.6	1.5		350 ± 2.0	0.59
TO15	31 ± 0.8	69 ± 0.8	3	2.5	449 ± 6.4	0.48
TO16	32 ± 1	68 ± 1	6		459 ± 7.4	0.15
TO19	31 ± 1	69 ± 1	15		428 ± 8.1	0.07

3.2.1. Hysteresis and target potential

The influence of deposition conditions on Ta-based coatings starts with the study of the sputtering discharge properties. The hysteresis analysis allows to understand the impact of the gas flow rate combined with the current density on the cathode voltage. Thus, Figure 3.1 shows the evolution of target potential as a function of O₂ flow rate for three different current densities applied under a constant Ar flow (50 sccm).
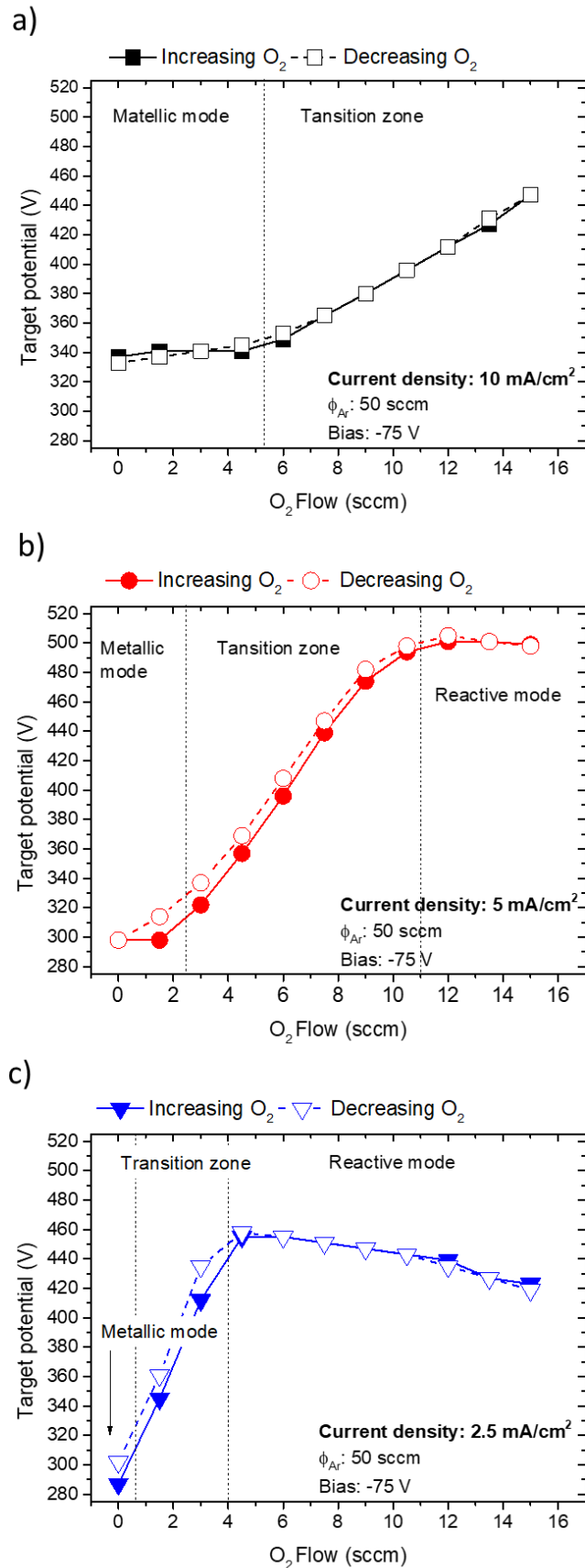
Figure 3.1: Evolution of target potential as a function of oxygen flow rate, under constant Ar flow (50 sccm) and bias voltage (-75V), for different current densities applied to the target: (a) 10 mA/cm²; (b) 5 mA/cm²; (c) 2.5 mA/cm².

It can be seen that the combination of current density 10 mA/cm^2 (Figure 3.1.a) with increasing O_2 flow is not enough to achieve the reactive mode and, therefore, the deposition occurred only in metallic mode/transition zone. When the current density decreased to 5 mA/cm^2 (Figure 3.1.b), it becomes possible to distinguish the different depositions modes. For an O_2 flow between 0 and 10 sccm, the deposition occurred in metallic mode/transition zone, since the target potential is continuously increasing. However, with a further increase of the O_2 flow (>10 sccm), the target potential achieved the maximum value and the deposition process changed to reactive mode where the formation of TaO_x is expected. A further decrease in the current density down to 2.5 mA/cm^2 (Figure 3.1.c) shows that the target potential achieved the maximum value immediately after O_2 flow of 4 sccm. This is characteristic of the reactive mode in which the deposition evolves to the deposition of TaO_x due to the poisoning effect of the target surface. The different zones associated to the deposition modes are identified on Figure 3.1.c). At the peak target potential, the discharge voltage and ion density reached the optimum conditions to restrict further oxidation of target surface. Thus, the constriction of the discharge area due to the poisoning effect also reaches a maximum [16]. Nonetheless, as it is reported by R. Hollerweger *et al.* [16], the subsequent decrease in the target potential (see Figure 3.2), revealing an unstable discharge and oxide formation conditions, indicates that initially the target surface is partially poisoned and then, proceeds until the whole target surface area is completely poisoned. Consequently, would be expected to reach a constant target potential regime, characterized by stable discharge conditions and oxide formation. In the sputtering system used, without compromising the deposition rate, this behavior is not reached due to the low O_2/Ar flow ratio.
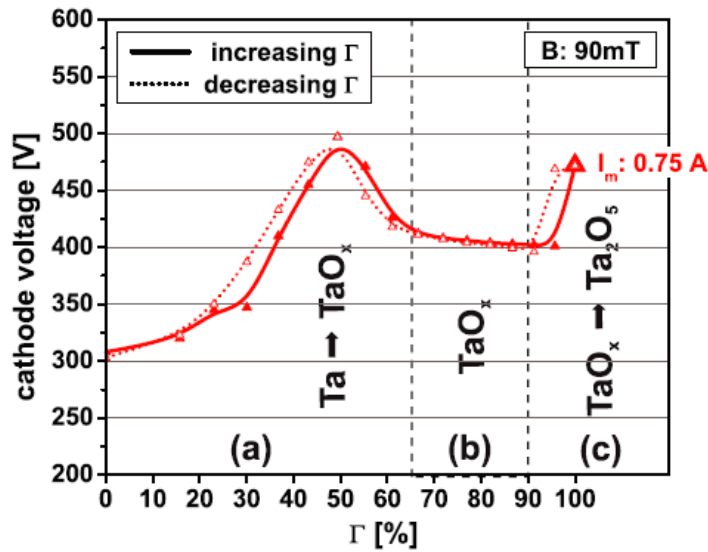
Figure 3.2: Cathode-voltage-hysteresis indicating the three main target poisoning regimes: (a) transition from Ta to TaO_x, (b) region of stable TaO_x and (c) transition from TaO_x to Ta_2O_5, reproduced from [1].

3.3. Fundamental characterization

3.3.1. Physical and chemical analysis

Differentiated conditions such as current density and reactive gas parameters were selected in order to produce coatings with different properties. Thus, the sputtering yield and deposition rate were adjusted to achieve different TaO_x coatings, as summarized in Table 3.1. The evolution of deposition rate and target potential with O_2 flow of both deposited series are depicted in Figure 3.3.

For the first series (10 mA/cm^2), a slightly decrease on the target potential is observed when a low O_2 flow was introduced. In fact, some materials show a higher SEEY emission when they are little oxidized [17]. Additionally, the first coating (Ta1) shows slightly higher target potential values comparing with the values observed in hysteresis curves because the erosion status of the target was lower when the deposition was made [16].
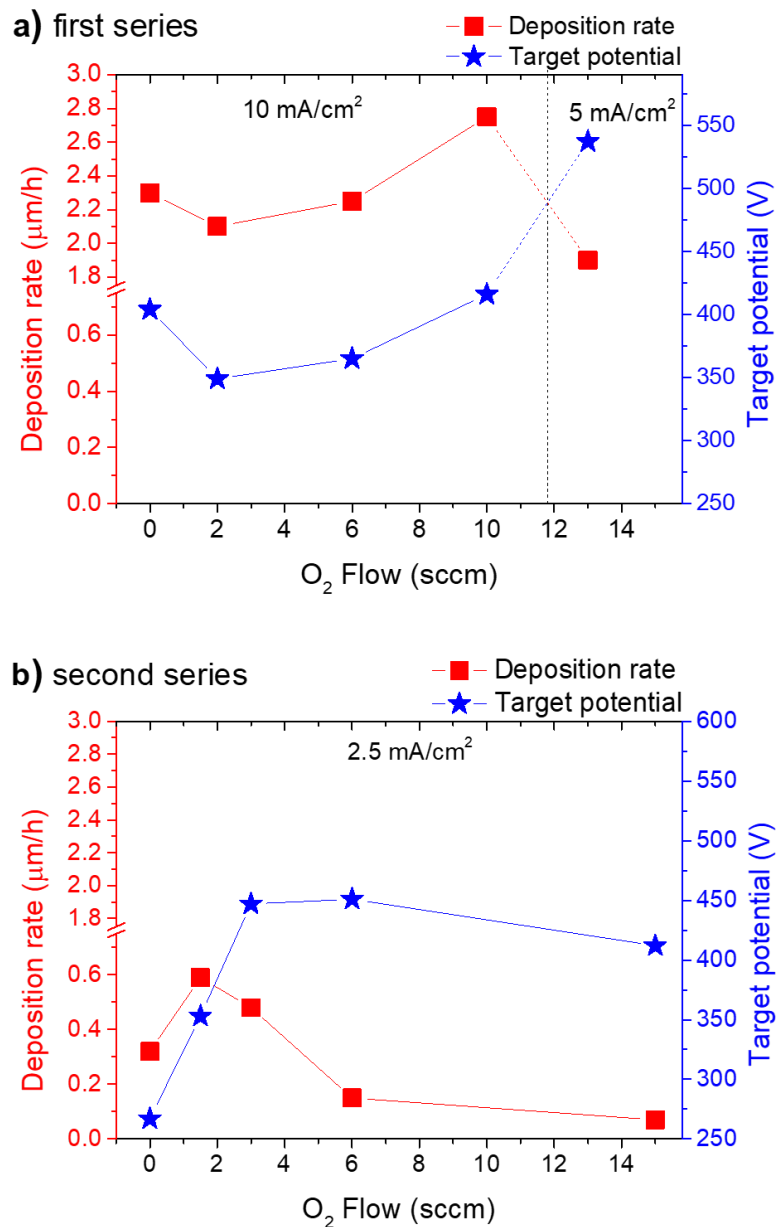
Figure 3.3: Evolution of deposition rate and target potential of $Ta_{1-x}O_x$ coatings as a function of oxygen flow: (a) first series (10 and 5 mA/cm^2); and (b) second series (2.5 mA/cm^2).

The further increase in the O_2 flow raised the deposition rate and target potential. In this regime, the target surface is composed by pure metallic zones mixed with oxidized zones. Therefore, the parallel sputtering of both zones, as well as, the partial reaction of species on the plasma atmosphere lead to an increase of the deposition rate. Simultaneously, the increase of the O_2 flow and consequently target surface oxidation cause an increase in the target potential due to the decrease of the SEEY of the oxide compounds (Ta and TaO_x)

that cover the target surface [16], in agreement with the previous hysteresis analysis. When the current density is changed to 5 mA/cm^2, the deposition rate decreases and the target potential reaches the maximum value. This behavior is mainly related to the clear reduction of the sputtering yield either related to the reduction of applied current density (half of the value) or to the poisoning effect of the target, which suggests that the deposition was done nearly in reactive mode.

Regarding the second series, when the O$_2$ flow is increased up to 2 sccm, a small increase in the deposition rate is observed since the sputtering process is occurring simultaneously from both pure metallic zones mixed with oxidized ones, as discussed above. When the O$_2$ flow was further increased, a systematic decrease in the deposition rate is observed due to the lower sputtering yield of the oxidized target compared to the metallic one. Hence, the target potential raises continuously to the maximum value at 3 sccm, which is related to the so-called poisoning effect by oxygen. Thereafter, for higher O$_2$ flow (up to 15 sccm) the target potential decreases, which indicates that the poisoning process is not complete seeing that the discharge of the target surface broadens due to the increase of the poisoned area.

Briefly, it can be said that the current density controls the deposition rate and both are directly related. On the other hand, for a given current density the deposition rate increases with the target potential (observed at 10 mA/cm^2 and from 0 to 2 at 2.5 mA/cm^2) mainly on metallic mode. After that point, the deposition rate drops down due to the lower sputtering yield of the oxidized surface vs. the metal like one mainly on reactive mode.

The chemical composition of the samples (see Table 3.1) is in good agreement with the results shown in Figure 3.1 and Figure 3.3. Ta1, TO1 and TO3 coatings are basically deposited in metallic mode (Figure 3.1), which is reflected in the high concentration of metal in the deposited layers (>70 at.%). TO5 coating deposited at 10 sccm shows lower metallic Ta content, being already in the transition regime (Figure 3.1). In contrast, TO6 coating, which was deposited at lower current density and higher O$_2$ flow, is into the reactive regime (Figure 3.1) and shows the highest oxygen concentration (70 at.%). In the second series, the overall behavior is similar. Ta6 coating is clearly metallic, while the

TO15, TO16 and TO19 are similar and belong to the reactive regime (*cf.* Figure 3.1). Finally, TO14 layer belongs to the transition zone and shows a high oxygen concentration, although not as high as the coatings deposited in the reactive regime.

3.3.2. Morphological assessment

SEM micrographs of cross-section of deposited coatings of both series are presented in Figure 3.4. Notice that the blue line marks the end of metallic Ta interlayer whereas the yellow line marks the end of Ta oxide interlayer (graded interlayer deposited for improving the adhesion on the ceramic coatings). Regarding the first series, Ta1 and TO1 coatings are formed by narrow columnar grains with densely packed fibrous morphology. This morphology is characteristic of coatings grown with low adatom mobility and diffusion at relatively high discharge pressures, corresponding to the transition zone of Thornton's model [18]. A densification of the coatings is observed when the oxygen flow is increased, reaching a featureless morphology. The presence of oxygen inhibits the nuclei growth and induces the renucleation of new and more stable grains, which results in a dense morphology [19]. The coating with the highest oxygen flow (TO6) was deposited with a different current density (5 mA/cm^2), and therefore its morphology cannot be directly compared with the other ones.

A similar tendency is observed in the second series as can be confirmed by the columnar morphology obtained for Ta6 coating. Again, the introduction of oxygen leads to the densification of the coatings and a featureless morphology. It is important to note that in TO16 and TO19 a second interlayer (marked with yellow line), composed by a $Ta_{1-x}O_x$ coating (equivalent to TO15), was deposited to create a gradient of oxygen composition to enhance the adhesion. Due to the thin measured thickness of TO16 and TO19 (around 350 and 200 nm respectively) the chemical composition of those films may be influenced by the presence of the Ta and/or $Ta_{1-x}O_x$ interlayers.

a)
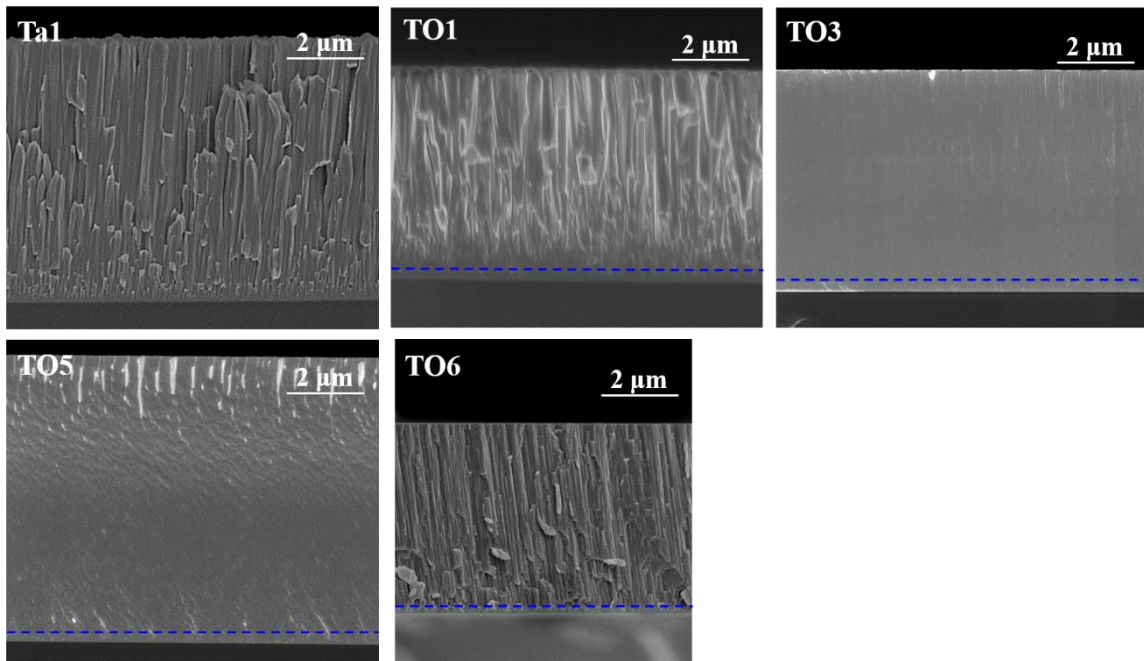
b)
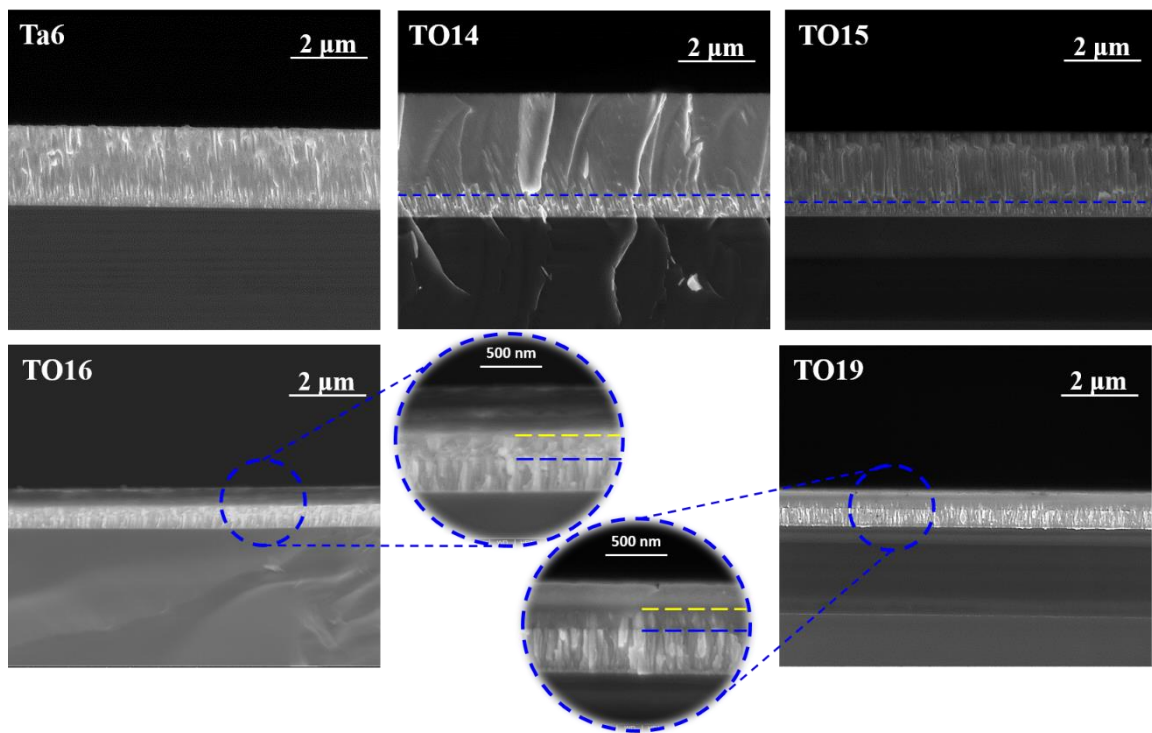
Figure 3.4: SEM cross-section micrographs of $Ta_{1-x}O_x$ coatings, deposited onto Si, as a function of oxygen content for the two series: (a) first series; and (b) second series.

3.3.3. Structural evolution

The evolution of the crystallographic structure with the increase of the oxygen content was evaluated by XRD (Figure 3.5). The identified crystalline phases are α-Ta (ICDD card nº 00-004-0788), β-Ta (ICDD card nº 00-025-1280) and Ta_4O (ICDD card nº 03-065-6450) (Annex V).
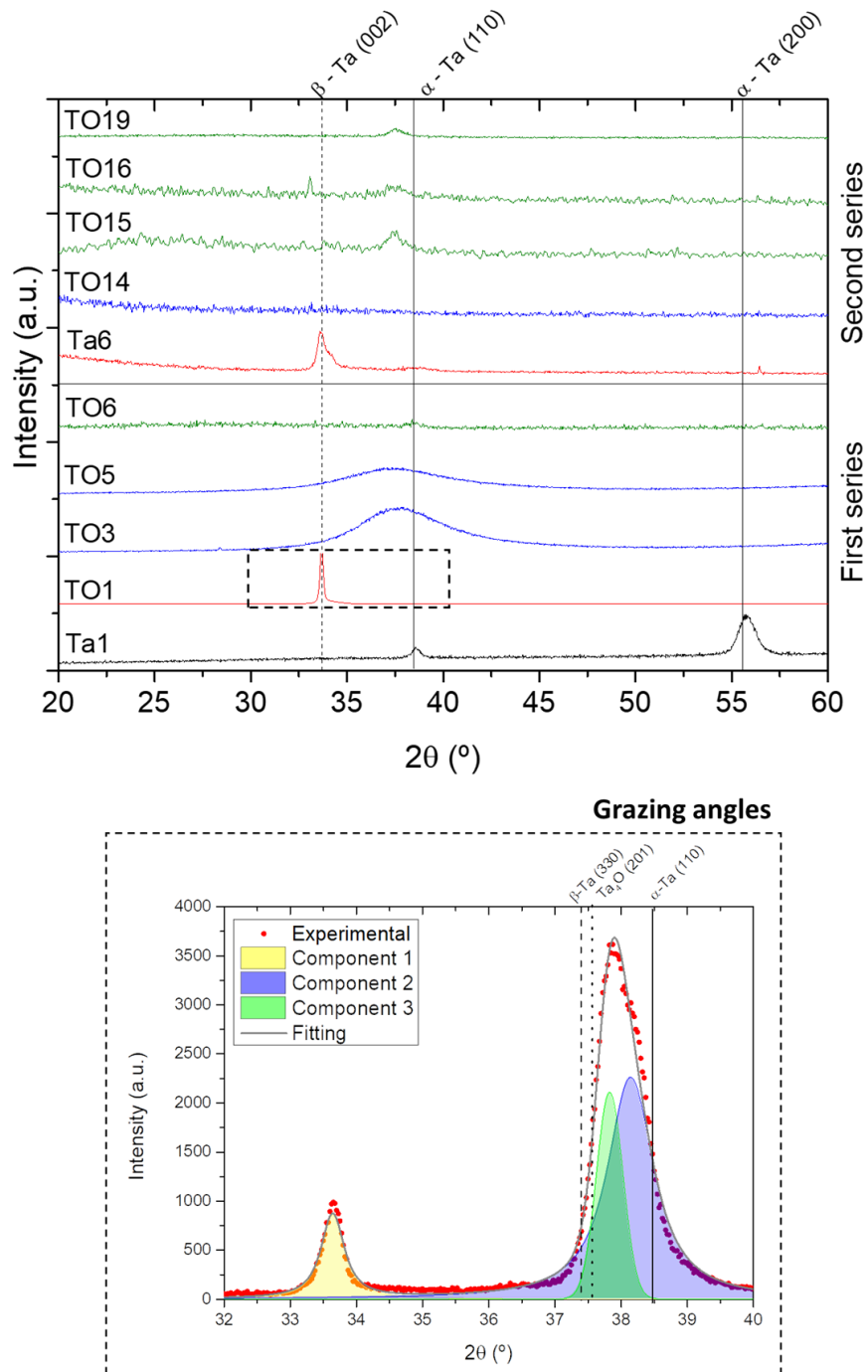
Figure 3.5: XRD patterns of $Ta_{1-x}O_x$ coatings, deposited onto Si, as a function of oxygen content for the two-deposited series (first and second).

For the first series, the non-reactive deposited Ta1 coating reveals the stable body-centered cubic (bcc) α-Ta phase. The non-usual formation of bcc α-Ta phase at relatively low deposition temperature (200 °C), when compared with Gladzuk *et al.* [20] results (400 °C), can be explained by the application of negative bias during the deposition, which increases the bombarding particles energy leading in a second stage to an increase of the local temperature [21]. When the oxygen content increases slightly above 11 at.% (TO1) a diffraction peak around 33° appears and the diffraction peak around 38° becomes asymmetric (see Grazing Angles insert in Figure 3.5) indicating that the material changed to a mixture of phases. This behavior is also reported by Zhou *et al.* [22, 23] in the Ta-O system for reactive sputtering with low O_2/Ar flow ratio. According to Kepner *et al.* [24] the incorporation of oxygen in the coating leads to a distortion in the structure of α-Ta phase (stable phase), due to its low solubility in this phase (≤ 1.4 at.%), promoting the formation of β-Ta phase [24]. Although, the asymmetric diffraction peak around 38° is also compatible with a Ta_4O structure, which exhibits a double diffraction peak around that value and hence shall not be discarded. These facts demonstrate that the α-Ta phase with incorporation of oxygen also forms a tetragonal phase, which might be erroneously considered as a pure β-Ta phase by XRD. TO3 and TO5 coatings, characterized by intermediate oxygen contents of 27 and 43 at.%, respectively, show a broad diffraction band around 37°, which indicates the presence of small grains sizes making difficult unequivocal identification of the crystalline phase(s). Indeed, metallic Ta and/or sub-stoichiometric TaO_x phases such as α-Ta, β-Ta, Ta_2O and/or Ta_4O may occur and cannot be discarded [25]. Nevertheless, with increasing oxygen content there is a shift of the band to lower angles due to an increase of the inter-atomic distance caused by the presence of more oxygen species. At higher oxygen content, TO6 (70 at.%) coating proved to be completely amorphous. Thus, the incorporation of oxygen in the crystal lattice caused its deformation promoting initially the precipitation of oxides at grain boundaries, which inhibits the grain growth, and in a second stage inhibiting the formation of a crystalline structure resulting in a formation of an amorphous phase [19].

Analyzing now the second series, the Ta6 (5 at.%) coating reveals a β-Ta phase. This can be related with the decrease of the deposition rate (as a result of lower current density), when compared with Ta1, which leads to higher oxygen incorporation and then formation

of a metastable phase. However, the presence of α-Ta phase cannot be discarded due to the presence of a slight diffraction band around 38°. In agreement with the results of previous series, the coatings with higher oxygen content become amorphous not showing any peak or diffraction band, which is in accordance with the tendency described previously for the first series. It is worth mentioning that the diffraction peaks around 33° and 38° are associated with the interlayers, hindering their indexation to a pure β-Ta or a mixture of β-Ta and α-Ta phases.

3.3.4. Thermal oxidation of Ta-based coatings

Considering that TaO_x phases are temperature dependent, the crystallographic evolution of $Ta_{1-x}O_x$ coatings was studied performing an *in-situ* annealing combined with XRD analysis, from room temperature up to 900 °C under air atmosphere. The coating deposited with a highest oxygen flow (TO19) was strategically selected taken into consideration the hysteresis analysis, which reveal an incompletely poisoning effect for this coating. Moreover, *in-situ* annealing was performed in order to study the crystallization process and identify which crystalline phases can be formed at each temperature.

The structure evolution of TO19 coating with increasing temperature is shown in Figure 3.6. The previous XRD data indicated that this coating is completely amorphous (see Figure 3.5), where the observed diffraction peaks (around 33° and 37°) correspond only to Ta interlayer. Ta interlayer was deposited with similar conditions than Ta1, which revealed α-Ta phase. The diffraction pattern remains unchangeable up to 500 °C, and only a small shift to lower angles can be noticed for the peak located at 38°, which may be associated to the oxygen incorporation. At 600 °C, the intensity of this peak is dramatically reduced and at 700 °C the peaks corresponding to the Ta_2O_5 orthorhombic phase (ICDD card nº. 00-025-0922) appear (diffraction peaks around 22.9, 28.3, 32.8, 36.7, 49.7 and 55.5°). The β-Ta or a mixture of β-Ta and α-Ta phases found initially remains attributed to the Ta interlayers crystallization.
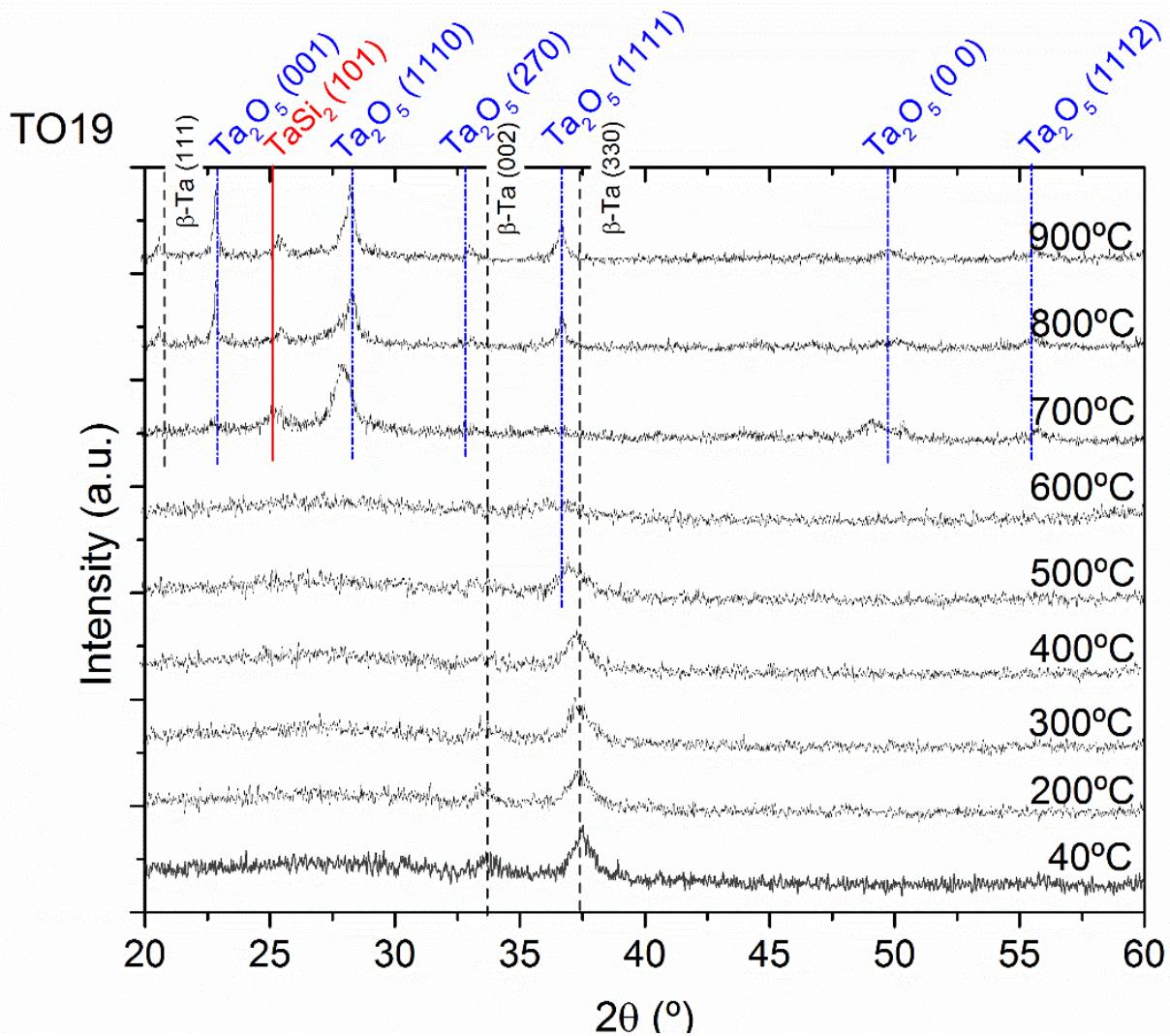
Figure 3.6: Bragg-Brentano XRD patterns of *in-situ* annealing of TO19 coating, deposited onto Si, as a function of temperature increase exposed at air atmosphere.

XPS studies were performed to identify the oxidation state of the coatings (see Figure 3.7). Ta can exhibit different oxidation states such as Ta^{5+}, Ta^{4+}, Ta^{2+}, Ta^{+} and Ta^{0} depending on the oxide type. Ta 4f peak appears as a spin-orbital doublet (Ta 4f 7/2 and Ta 4f 5/2), separated by 1.9 ± 0.1 eV with an intensity ratio around 1.3-1.4 [26-29]. Figure 3.7 shows the Ta 4f and O 1s XPS spectra of the coating TO19 acquired before (a, b) and after (c, d) thermal annealing. The fitting parameters of the spectrum deconvolution are included in Table 3.2.

Both Ta 4f photoemission spectra show the spectral doublet around 26 ± 0.2 (4f 7/2) and 27.9 ± 0.2 (4f 5/2) eV (the spin-orbit coupling was fixed at 1.9 eV). The binding energies of this doublet are similar to the energies observed in Ta_2O_5 references [30, 29], indicating that the Ta exhibits the highest oxidation state. This state is confirmed by the binding energy of the O 1s peak at 530.5 ± 0.3 eV, which corresponds to the O-Ta bonding according to the literature [31, 26, 32, 33]. It is worth mentioning that the small peak nearby 532 ± 0.5 eV on O 1s spectrum of TO19 BA coating is attributed to a surface contamination [33].
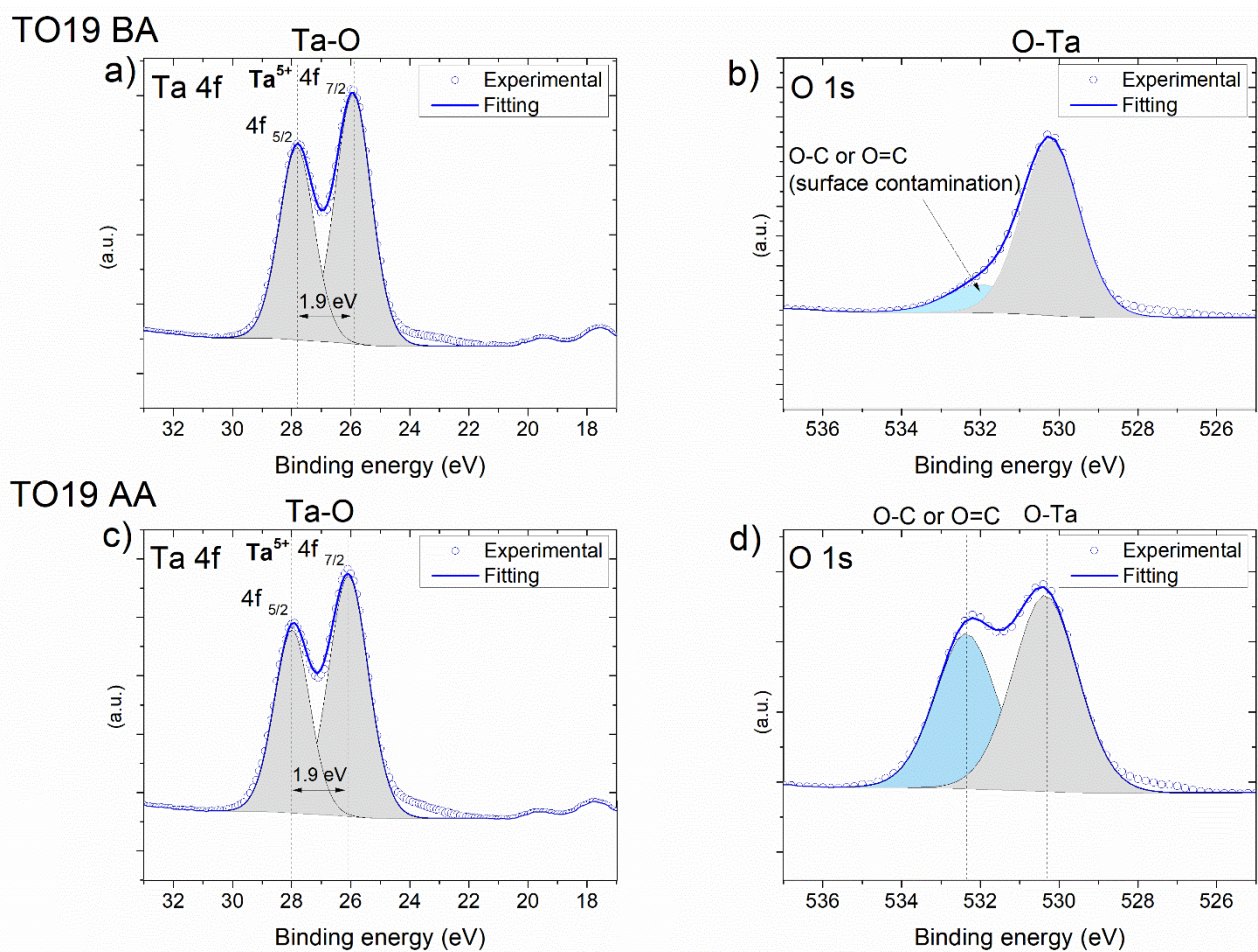
Figure 3.7: Ta 4f and O 1s XPS spectra of TO19 coating before and after thermal annealing in air atmosphere, deposited onto Si substrates.

After annealing, the previous surface contamination becomes pronounced and part of the coating. The increase of the intensity of O-C or O=C binding energy occurs due to the air

atmosphere used during the annealing, inducing the carbon incorporation into the coating. This result agrees with the initial expectations, since this coating started highly oxidized initially and mainly crystallization process took place after heating it.

It can be observed that Ta 4f7/2 and O 1s positions and the ratio between Ta 4f 7/2 and 5/2 peak area, which vary between 1.35 and 1.46 eV, are well related with the reported values in literature. Additionally, the FWHM and the energy difference between Ta 4f7/2 and O 1s nearby 1.4-1.6 eV, 1.7-1.9 and 504 eV, respectively, are in good agreement with the reported values for Ta_2O_5 as well [34, 26, 28, 29]. The estimated ratio between O/Ta ($\approx$2) is lower than the ratio observed to Ta_2O_5 (2.5), which indicates that the composition of the TaO_x has a small deficit in oxygen, which may be due to the surface contamination.

Table 3.2: Summary of XPS fitting parameters of peak deconvolution of TO19 coating before and after thermal annealing in air atmosphere, deposited onto Si substrate.

Sample	Ta 4f			O1s		ΔBE O-Ta (eV)	Area ratio O/Ta
	BE Ta 4f 7/2 (eV)	FWHM (eV)	A $_{(4f\ 7/2)}$ /A $_{(4f\ 5/2)}$	BE O 1s (eV)	FWHM (eV)		
TO19 BA	25.9	1.44	1.35	530.2	1.71	504.3	2.0
TO19 AA	26.1	1.58	1.46	530.4	1.94	504.3	2.1

3.3.5. Optical characterization

Figure 3.8 shows the FTIR spectra for both series of $Ta_{1-x}O_x$ coatings. The coatings deposited in the first series, all deposited at 10 mA/cm^2 with low or intermediate oxygen flow, shows a metallic behavior, not being possible to identify any band in the analyzed wavenumber range. The same metallic behavior is observed for Ta6 coating from the second series of coatings. In contrast, for TO6 coating from the first series, which present much higher oxygen content (since it was deposited with 5 mA/cm^2), as well as, for TO15, TO16 and TO19 from the second series it is possible to identify several bands correlated to the formation of different oxide compounds. Although it seems that TO14 shows an

absorption band (around 810 cm^{-1}) the band is only an interference effect due to the high thickness of the coating.
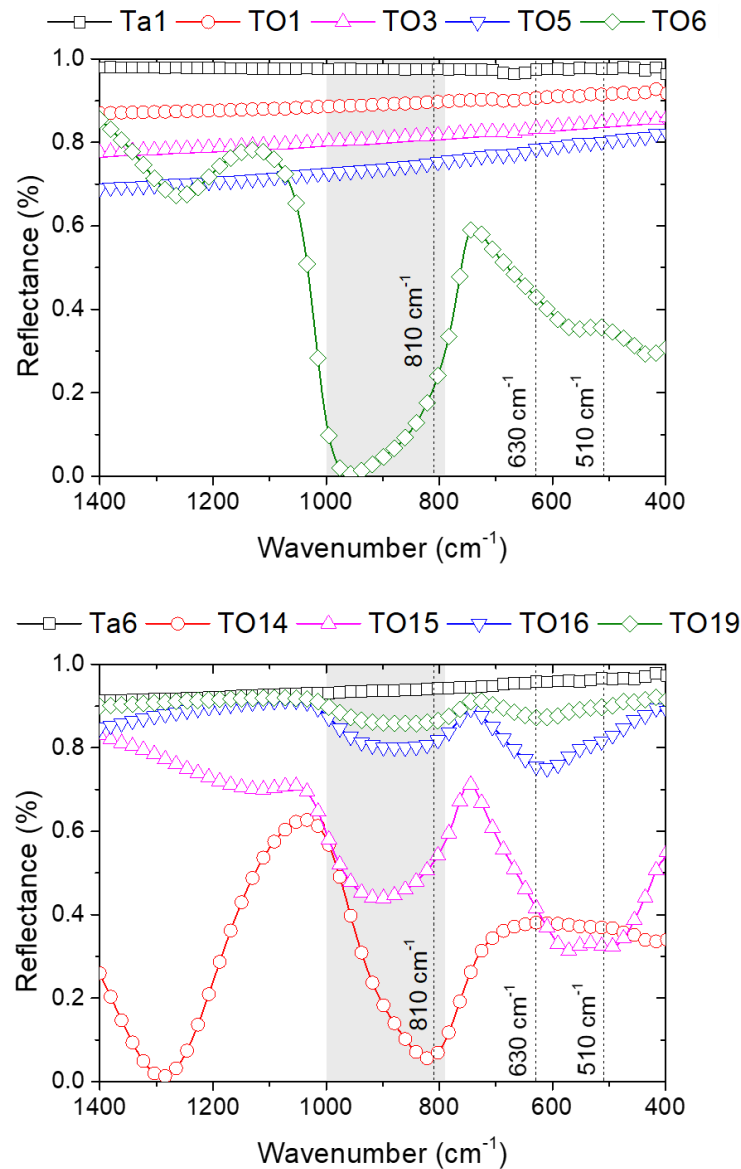
Figure 3.8: FTIR spectra in a range of wavenumbers (400-1400 cm^{-1}) of both series of Ta$_{1-x}$O$_x$ coatings, deposited onto Si substrates, as a function of oxygen content: (a) first; and (b) second series.

Typically, FTIR spectra of stoichiometric crystalline TaO$_x$ show absorption bands centered at 810 and 510 cm^{-1} corresponding to a Ta-O-Ta and O≡3Ta stretching modes, respectively [35, 21]. These bands could shift to 700-1000 and 630-640 cm^{-1}, respectively, when the material becomes amorphous [36-38, 35]. Table 3.3 summarize these absorption bands

and relate them to the different stretching modes of TaO$_x$ in amorphous or crystalline state.

Table 3.3: Wavenumbers of the absorptions bands to the different stretching modes of TaO$_x$ in amorphous or crystalline nature.

Vibration Mode	Amorphous (cm^{-1})	Crystalline (cm^{-1})
3 Ta ≡ O	630-640	510
Ta – O – Ta	790 - 1000	810
Ta = O	2340	2335

Ta1, TO1, TO3, TO5, Ta6 and TO14 (deposited in metallic and transition regimes) reveal a metallic behavior without evidence of any absorption band. This is related with the chemical composition since they have lower and intermediate oxygen contents (from 5 at.% up to 62 at%). On the other hand, TO6 (70 at.% oxygen deposited with 5 mA/cm^2) and TO15 (69 at.% O deposited with 2.5 mA/cm^2) coatings reveal an absorption band around 700-1000 cm^{-1} corresponding to a Ta-O-Ta stretching mode in an amorphous structure, in good agreement with XRD results, as well as, exhibit a slightly shifted band at 550 cm^{-1}. This shift is already reported and suggest that despite being amorphous the layer contains some crystals embedded onto the amorphous matrix [39]. Nevertheless, these results cannot be undoubtedly corroborated with the XRD analysis, which only indicates the small size of these grains for TO6 and TO15. Additionally, the presence of an absorption band at 510 cm^{-1} in TO15 coating suggests the presence of crystallites, although not detected in the XRD results. For TO16 and TO19 coatings the band around 510-550 cm^{-1} (nanocrystalline-crystalline behavior) is suppressed and the band around 640 cm^{-1} becomes more intense and defined, which indicates a marked amorphous nature of these coatings, which is in good agreement with the XRD results.

Table 3.4: Summary of FTIR absorption bands present in each deposited coating.

Type of sample	Samples	Amorphous bands (cm^{-1})		Nano-crystalline band	Crystalline bands (cm^{-1})	
		3 Ta ≡ O	Ta-O-Ta		3 Ta ≡ O	Ta-O-Ta
		630-640	790-1000	550	510	810
Metallic	Ta1, TO1, TO3, TO5, Ta6 and TO14					
Presence of crystalline oxides band	TO15		X	X	X	
	TO6		X	X		
Amorphous oxides	TO16 and TO19	X	X			

Spectroscopic Ellipsometry (SE) was used as complementary technique to study the amorphous/nanocrystalline nature of the coatings TO6, TO15, TO16 and TO19 due to the apparently contradictory results obtained by XRD and FTIR. Considering that all the coatings are mainly amorphous, as well as, the Ta$_2$O$_5$ gap is located within the measured energy, a Tauc-Lorentz (TL) dispersion function was used to fit the SE experimental data. In effect, single TL oscillator model is widely used to simulate the optical response of amorphous materials, not only in dielectrics but also on semiconductors materials. Moreover, it is reported that two or more TL oscillators models may be used to multi-transition amorphous or polycrystalline materials [40-42]. For TO6 and TO15, the simulation of experimental data was done using a 3-layer model, represented in Figure 3.9.a). It was considered that the substrate is indeed metallic Ta, since it was purposely deposited as an adhesion interlayer and is opaque. The optical behavior of the substrate was simulated using a Drude oscillator, while the bulk of Ta$_2$O$_5$ coating was simulated by a single TL dispersion and roughness simulated by a Bruggemann Effective Model Approximation (BEMA) consisting by a mixture of 50% Ta$_2$O$_5$ and 50% of voids. An incubation layer, between the substrate and the coating, normally formed during sputtering deposition [43], was not considered in the final model since no improvements were observed in the fitting. Still, as no interfacial layer was considered, the bulk thickness extrapolation needs to be carefully analyzed [44, 42]. In fact, for TO16 and TO19 films an

interfacial layer had to be considered to improve fitting results, resulting in a four-layer model (see Figure 3.9.b). But, in these cases, the interfacial layer is associated with the intentional graded interlayer deposited, with lower oxygen flow rate, as gradient adhesion interlayer, instead considering an incubation layer. Table 3.5 summarizes the simulated TL dispersion parameters of the $Ta_{1-x}O_x$ coatings.
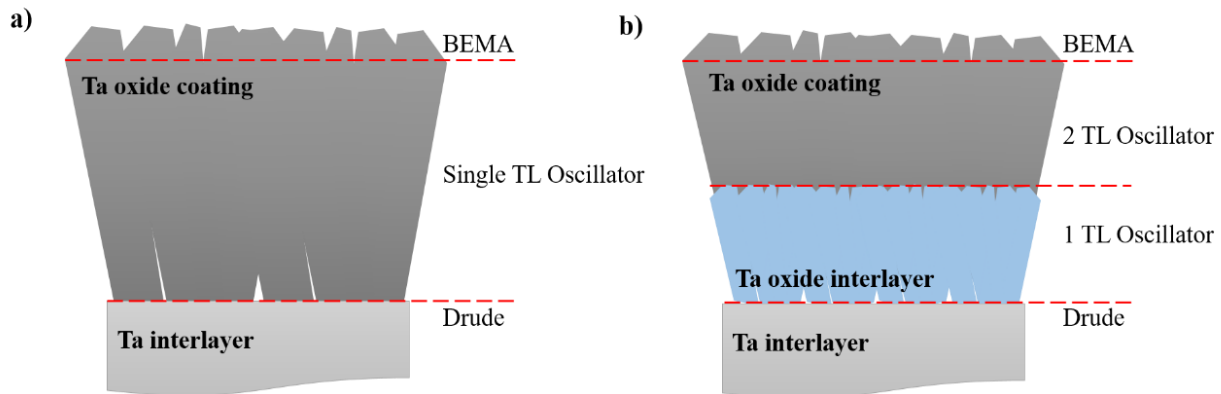
Figure 3.9: Schematic representation of the models used to simulate the optical response of the $Ta_{1-x}O_x$ coatings: (a) Three-layer model used in TO6 and TO15 coatings; (b) Four-layer model used in TO16 and TO19 coatings. The use of a double TL dispersion is only to improve the goodness of the fit in the high-energy region since the transition energy for these oscillators is outside the measured energy range.

As mentioned before, the best fitting results are reached using a TL oscillator as demonstrated by the goodness of fit obtained through minimization of the unbiased estimator (χ^2), which results from the difference between the experimental and simulation data. Concerning simulated results, as expected, the thickness values are near to the values determined by SEM. The roughness is low, in line with the expected values for amorphous films with similar thickness. Furthermore, the analysis of the other fitting parameters allows to infer some small structural modifications. For instance, the A parameter related with material density, is higher for the nanocrystalline TO6 coating. On the other hand, the analysis of the C parameter, which is inversely related with the short-range order within the layers, is not conclusive, suggesting that despite some nanocrystals may exist embedded in the layer, it is essentially amorphous.

Table 3.5: Coating thickness (d_c) and roughness(d_r) as well as, band gap (E_g), transition matrix element (A), broadening parameter (C), peak transition energy (E), unbiased estimator (χ^2) and refractive index (n) parameters of the $Ta_{1-x}O_x$ coatings estimated by SE fitting. The refractive index was determined at 0.65 µm.

Sample	d_c (nm)	d_r (nm)	E_g (eV)	A (eV)	C (eV)	E (eV)	χ^2	n
TO6	3287 ± 55	8.94 ± 0.71	4.30 ± 0.035	310 ± 19	2.67 ± 0.28	5.81 ± 0.049	1.34 ± 0.055	2.27
TO15	1633 ± 6.1	7.69 ± 0.13	4.04 ± 0.015	180 ± 3.3	2.36 ± 0.015	6.12 ± 0.028	1.56 ± 0.040	2.16
TO16	510 ± 7.8	6.18 ± 0.31	4.11 ± 0.037	202 ± 16	2.51 ± 0.067	5.24 ± 0.077	2.16 ± 0.089	2.09
TO19	306 ± 6.5	2.44 ± 0.20	4.13 ± 0.024	242 ± 15	2.27 ± 0.037	5.11 ± 0.053	2.16 ± 0.084	2.14

Figure 3.10 shows the refractive index (**n**) of $Ta_{1-x}O_x$ coatings, at different wavelengths, obtained from the TL dispersion parameters, after fitting. The values of refractive index vary between 2.09 and 2.27 at 0.65 µm, *cf.* Table 3.5, close to values reported for Ta_2O_5 thin films [45-47]. Nevertheless, some differences exist and can be correlated with modifications in the crystallinity [45]. On this regard, must be considered that the differences in the refractive index are associated with different crystallinity of the coatings. TO6 and TO15 coatings reveal the highest and narrow peaks suggesting its high density and high short-range order, respectively, in good agreement with the results obtained by FTIR. Whereas, TO16 and TO19 coatings exhibit a smaller and broad peak confirming the marked amorphous nature, also in agreement with the FTIR results (*cf.* Table 3.4). Also, the energy shift for the maximum value of refractive index suggest differences in the structure of the coatings TO6 and TO15 on regard to TO16 and TO19.
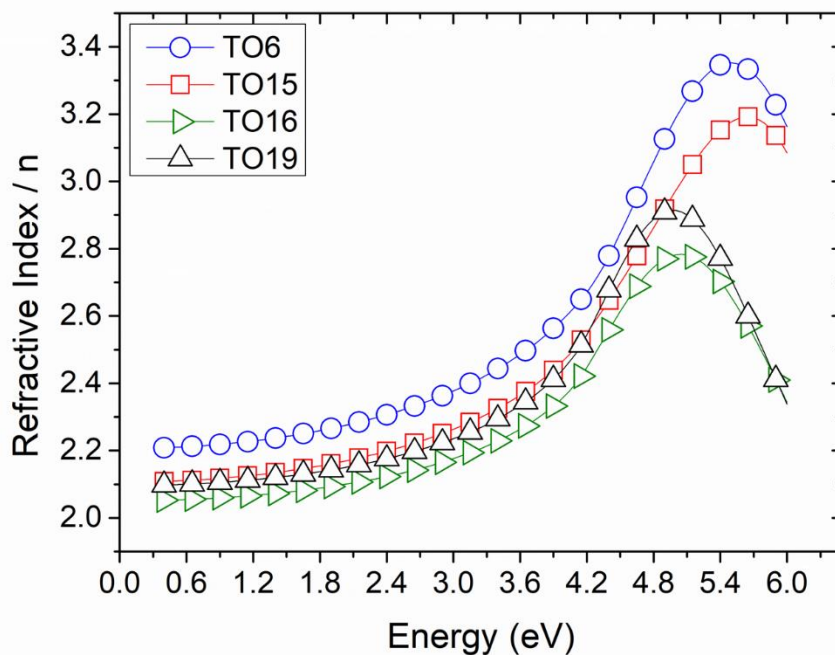
Figure 3.10: Variation of the refractive index (n) of the $Ta_{1-x}O_x$ coatings as a function of energy.

The IR spectrum and ellipsometry data suggest a four steps evolution: metallic - metallic-nanocrystalline - TO15-TO6 and TO16-TO19, which follows the trend shown in Figure 3.11. Figure 3.11 exposes the "*summary hysteresis curve*" of this study after normalization of

the target potential and oxygen flow rate. The x axes of *"the hysteresis curves"* were linearly modified to reach a coincident shape of the curves, in such a way that the minimum flow was set to zero and the half of the curves was set to 1. When deposited in metallic mode, the coatings are basically a metallic-like coating, although oxygen can be incorporated. Then, metallic Ta (Ta1) and 'not-so-crystalline' Ta (with oxygen incorporated - TO1, Ta6, TO3, TO5 and TO14) can be seen. When the threshold of the reactive mode is approaching, the target is strongly oxidized. Indeed, in TO15 and TO6 formation of nanocrystalline oxides (*i.e.* proto-grains that are observed by IR, but not by XRD) can be identified. However, it still not present that much O_2 in the chamber (a lot reacts with the target) to achieve the reactive mode. When the "partial poisoned" regime is achieved, the Ta target cannot accommodate more O and the sputtering changes. The deposition rate drastically decreases, as well as, the deposition temperature decreases the adatom mobility. Then, only amorphous oxides (TO16 and TO19) can be observed, probably due to the interference of O_2 in the growth of the coating.
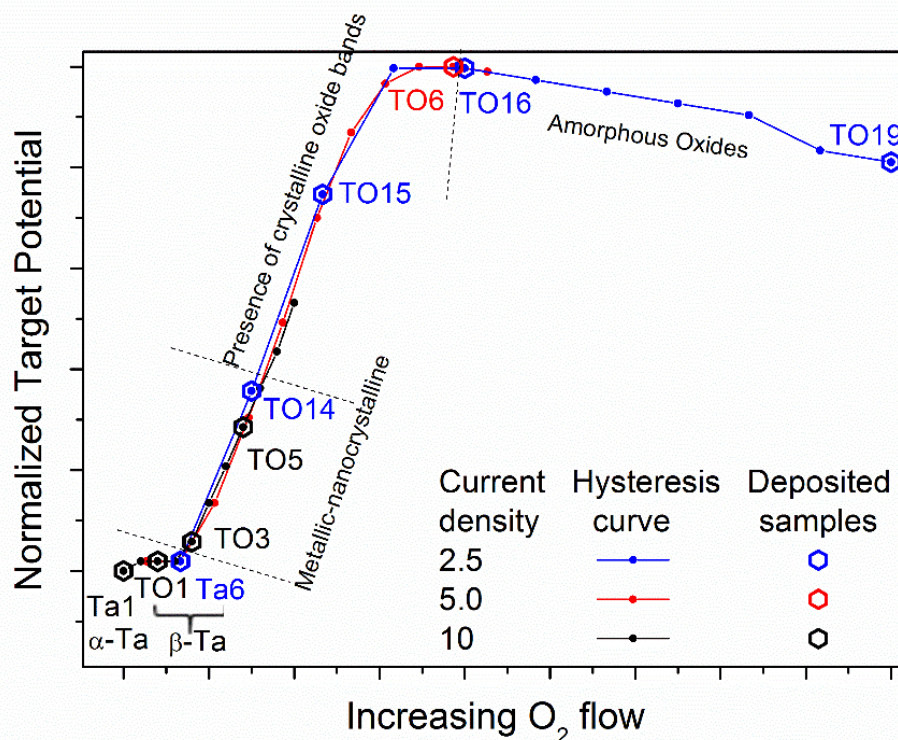
Figure 3.11: Summary hysteresis curve used in our study after normalization of the target potential and oxygen flow rate.

Nonetheless, after identification of the three deposition regimes and the coatings distribution along them, the first series of coatings is selected to perform the further characterizations. Take into consideration the desired industrial applicability for these coatings, it is important to ensure diversity and good properties, as well as, ensure good quality coatings at relative high deposition rates, being industrially cost effective.

3.4. Elastic modulus analysis

Along this chapter, it was shown that small increase of oxygen content leads to a change of Ta phase from stable phase (α-Ta: bcc) to mixture of phases. For coatings with intermediate oxygen content (TO3 and TO5) the broad diffraction band at 37° suggests that the coatings are nanocrystalline making difficult an unequivocal identification of the phase or phases occurring. In fact, in this zone, diffraction peaks of Ta and sub-stoichiometric TaO_x phases, such as α-Ta, β-Ta, Ta_2O, TaO_2 and/or Ta_2O_5 phases may occur. Thus, the use of the synergy between a theoretical study based on *ab-initio* calculations of the structures and elastic properties of different TaO_x phases and the experimental results allow an unequivocally indexation of the crystal structures. This study is fundamental for understanding the relationships chain "deposition / crystal-structure versus specific elastic properties". *Ab-initio* density functional theory calculations were carried out to obtain information about the theoretical lattice parameter, formation energy and elastic properties as a function of oxygen addition to a pure Ta bcc lattice.

To guide the results obtained by *ab-initio DFT* calculations, the density and elastic modulus (E), determined by SAW measurements, are shown in Table 3.6, as a function of the oxygen content in the coatings. In the calculation of elastic modulus, the coating thickness (evaluated by SEM) and the Poisson ratio of 0.34 were used in the fitting procedure.

Table 3.6: Chemical composition, deposition parameters, deposition rate, density and elastic modulus (E) of $Ta_{1-x}O_x$ coatings as a function of oxygen content, deposited onto Si substrates. The density and elastic properties were measured by surface acoustic waves (SAW), with a Poisson ratio of 0.34, resulting from an average of six measurements.

Sample	Chemical composition (at.%)		O_2 partial pressure (×10^{-2} Pa)	Current density (mA/cm^2)	Deposition rate (µm/h)	SAW	
	Ta	O				Density (g/cm^3)	Elastic modulus
Ta1	95 ± 0.3	5 ± 0.3	N/A		2.3	17.6±0.13	196±6
TO1	89 ± 0.6	11 ± 0.6	5.2		2.1	16.2±0.09	241±8
TO3	73 ± 0.2	27 ± 0.2	10	10	2.3	15.7±0.09	248±7
TO5	57 ± 0.2	43 ± 0.2	15		2.8	14.2±0.06	239±6
TO6	*30 ± 0.4*	*70 ± 0.4*	*20*	*5*	*1.9*	*8.96±0.09*	*155±5*

Generally, a density decrease and elastic modulus increase is observed with the increase of oxygen content and consequent coatings amorphization. Therefore, the incorporation of oxygen atoms into the Ta crystal structure leads to a distortion of the initial structure, decreasing the density while the elastic properties are enhanced due to the higher deformation that amorphous materials with low atomic arrangement and stronger chemical bonds may support.

TO1 and TO6 coatings do not follow the same tendency. In spite of the lower oxygen content in TO1, compared with TO3 and TO5, the elastic modulus is very close in all of them; for TO6 an unexpected decrease in the elastic modulus is observed even with the further increase of the oxygen content.

Ab-initio DFT calculations were performed to obtain the enthalpy of formation, density, Poisson ratio and elastic modulus for different Ta and TaO_x phases in order to understand this behavior. These results are shown in Table 3.7.

Table 3.7: Enthalpy formation, density, elastic constants (C11, C12, C22 and C44) (Annex II), bulk modulus (Bv, Br), shear modulus (Gv, Gr), elastic modulus (E) and Poisson's ratio (n) of Ta and TaOx crystal structures, estimated by *DFT* calculations.

Structure	ΔHf (KJ/mol)	Density (g/cm³)	C11 (KBar)	C12 (KBar)	C22 (KBar)	C44 (KBar)	Bv (GPa)	Gv (GPa)	Br (GPa)	Gr (GPa)	E (GPa)	E [100] (GPa)	E [110] (GPa)	E [111] (GPa)	n
α-Ta	0.00	16.59	2775	1643	2775	716	205	66	205	66	179	157	184	195	0.35
β-Ta	0.00	16.26	2979	1439	2979	665	202	62	202	59	165	207	187	182	0.36
Ta₆O	-321	15.24	2655	1607	2803	720	201	67	201	66	179	146	180	195	0.35
Ta₄O	-353	15.64	3098	1547	3098	1107	227	77	222	67	196	209	262	285	0.35
Ta₂O	72	11.62	317	1830	317	378	134	-8	134	96	119	-284	160	105	0.35
α-Ta+5 at.% O interstitial	-5.14	16.33	2841	1642	2841	722	207	68	207	68	184	166	188	196	0.35
TaO	-244	13.81	2715	2356	2715	-893	251	-47	251	65	27	53	441	-309	0.48
TaO₂	-885	9.11	3610	2588	3610	2588	267	126	266	97	293	147	340	608	0.32
β-Ta₂O₅	-1019	7.13	2814	1216	6315	351	233	130	199	68	257	211	115	100	0.30
δ-Ta₂O₅	-1117	7.44	2386	887	2226	581	205	81	161	71	200	193	163	155	0.32
Amorphous δ-Ta₂O₅	-1385	7.49	4600	2625	4204	874	336	94	333	91	254				0.37

The calculations established an increase of the phases' stability with higher oxygen content. However, Ta_2O and TaO were found to be thermodynamically unstable structures under stress. The former presents a large enthalpy of formation ($\Delta H_f > 0$) and born instability ($C_{11} - C_{12} < 0$), while the latter possesses shear elastic instability ($C_{44} < 0$). Thus, these phases are not considered for further analysis. Moreover, Ta_4O structure shows a remarkable stability and may be seen as a bcc Ta with oxygen atoms in interstitial positions. As final remark, it can be concluded that the insertion of interstitial oxygen in α-Ta phase tends to give rise to the formation of stable compounds.

The density obtained by *DFT* calculations is in a good agreement with both SAW experimental data and literature results. With the increasing addition of oxygen to the Ta phase, a decrease in the density of the crystal structures is observed, explained by the incorporation of oxygen atoms into the Ta leading to a distortion of the initial crystal structure [24].

In what concerns the elastic modulus of pure Ta phase, a correlation between the experimental results and *DFT* calculations can also be established. In the case of $Ta_{1-x}O_x$ coatings, the evolution of the elastic modulus must be carefully analyzed. In fact, there is a significant increase of elastic modulus from the non-reactive Ta1 coating to TO1 coating, despite the small difference in the oxygen content. Moreover, the high value of elastic's modulus measured for the coating with mixture of phases (TO1), is much larger than the values obtained by *DFT* calculations for Ta metallic phases (α and β). On this concern, theoretical simulations were performed for α-Ta base lattice with interstitial addition of different amounts of oxygen. Naturally, depending on the oxygen content added, the base crystalline structure evolves to other structures. For instance, α-Ta + 5 at.% O maintains the bcc phase and Ta_4O (α-Ta + 20 at.% O) assumes the very stable tetragonal phase ($\Delta H < 0$). The increase of the oxygen content into the α-Ta phase, from 5 up to 20 at.%, causes significant distortion, making the elastic modulus highly anisotropic (see Table 3.7 - E [100], E [110] and E [111]). Thus, apparently, the mixture of α-Ta with the Ta_4O phases allows to explain the TO1 behavior, which is in good agreement with XRD analysis.

In the case of coatings with intermediate oxygen content, TO3 and TO5, an increase of the oxygen leads to both a loss of crystallinity and the decrease of the density. To further

analyze the structure, STEM/EDS mapping was performed in cross section. The STEM images (Figure 3.12) show a multilayer growth for both TO3 and TO5 coatings.
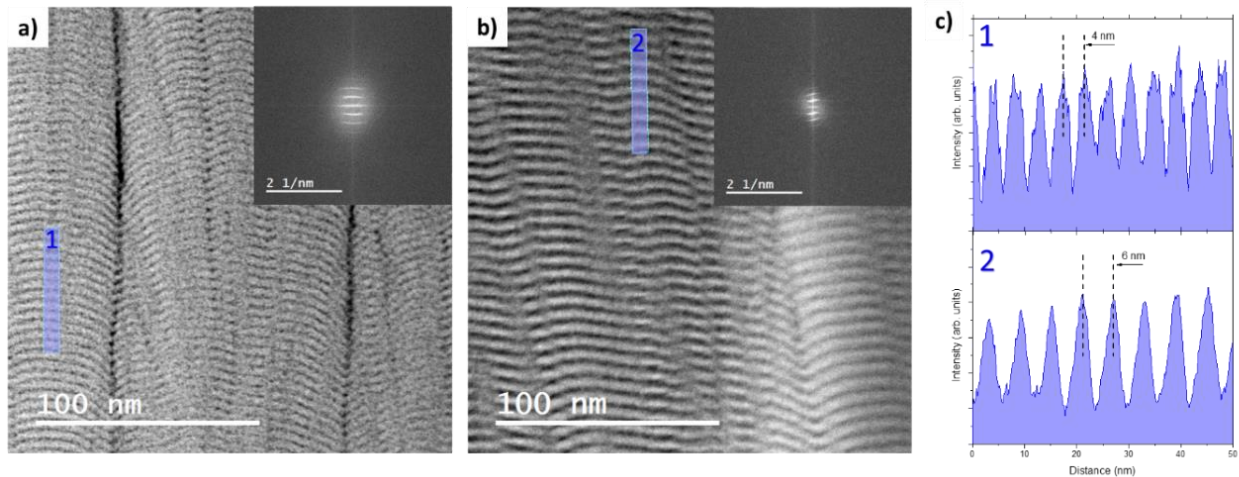
Figure 3.12: Cross-section HAADF STEM images of a) TO3 and b) TO5 coatings with their corresponding Fast Fourier Transform, c) intensity profile calculated on the HAADF images for TO3 and TO5.

This multilayer configuration is attributed to the deposition conditions. In fact, the depositions were carried out using only one Ta target in a non-poisoned mode (transition zone) and rotation of the substrate holder; thus, the formation of a differentiated plasma surrounding the substrate holder can be expected. When the sample is facing the target a fresh metallic Ta layer is deposited, which is very difficult to oxidize due to the high Ta deposition rate as a consequence of the high Ta sputtering yield. On the other hand, when the sample is turning around, the oxidative plasma environment (Ar + O_2) promotes the oxidation of the films, which results in an increase of oxygen in the surface of the Ta layer, including this multilayer aspect (see Figure 3.13). The multilayer growth also allows to explain the IR results where these coatings revealed a metallic behavior. Moreover, as the oxygen flow increase due to the higher incorporation of oxygen in the growing film leads the deposition rate increase and hence, the thickness of each multilayer also increase.
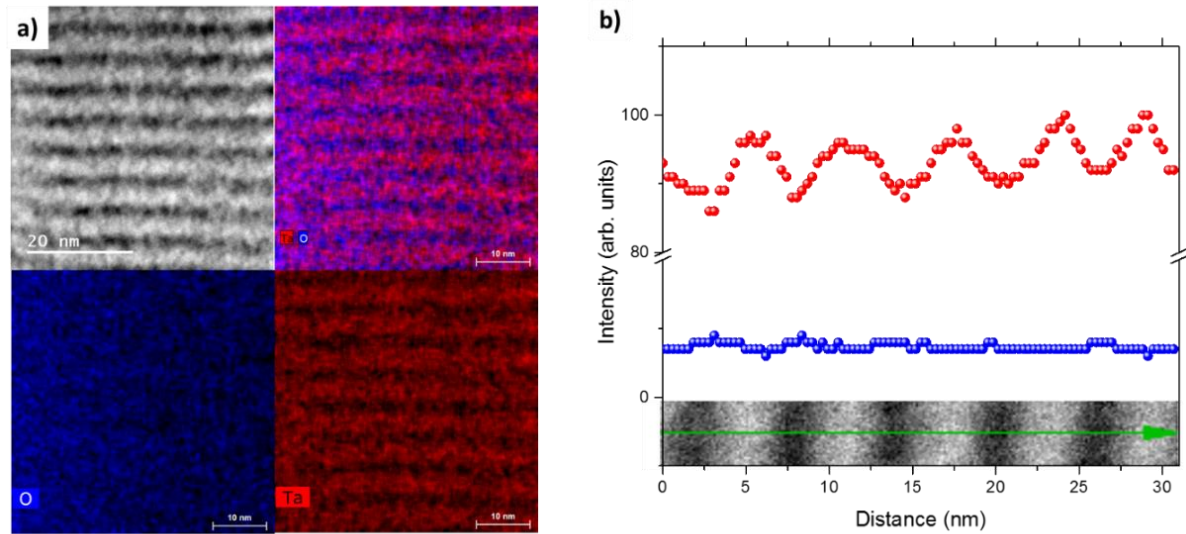
Figure 3.13: a) HAADF STEM and EDS spectrum images showing the elemental distribution for the multilayer structures (TO5) and b) Line composition analysis acquired by EDS for 5 bilayers of TO5 coating.

The multilayer growth combined with the overall decrease in the crystallinity of the coatings with increasing oxygen content, explain the high elastic modulus values. Additionally, the increase of oxygen content induces a decrease in the metallic bonds and the formation of stronger chemical bonds with only a slight reduction of the density, which in turns, results in high values of elastic modulus. These arguments are supported by *DFT* calculations of elastic properties (Table 3.7) where an increase in the elastic modulus can be observed for stable amorphous TaO_x phases together with an overall decrease in the material density.

Finally, despite of presenting higher oxygen content, TO6 reveals the lowest elastic modulus and density values, 155 GPa and 9 g/cm^3, respectively. This density level is attained by the large incorporation of oxygen in the structure, as demonstrated by *DFT* calculation, which results in a lower average elastic modulus, when compare to low oxygen content samples. Moreover, TO6 coating is formed by narrow columnar grains morphology, exhibiting a lower density caused by the lower applied current density, while TO3 and TO5 revealed a featureless morphology, which help to explain elastic modulus decrease. On the other hand, the chemical composition evaluated by EPMA does not allow to certainly identify and differentiate the TaO_x stoichiometric between TaO_2 and

Ta_2O_5, since the difference between these two phases is small [16]. Although the amorphous character revealed by XRD, based on *DFT* results, it seems that this coating has characteristics of a δ-Ta_2O_5 phase, judging by the low density and a low elastic modulus of this structure, comparing with TaO_x (crystalline and amorphous). This is also supported by the high thermodynamically stability of δ-Ta_2O_5 phase, which has one of the lowest enthalpy formation (-1116 KJ/mol) of all TaO_x structures, as estimated by *DFT* calculations. These results are supported by the previous FTIR results, where a contribution of a nanocrystalline TaO_x embedded onto an amorphous matrix was observed for this coating.

3.5. Partial conclusions

$Ta_{1-x}O_x$ coatings with different oxygen content have been successfully deposited by reactive magnetron sputtering. The increase in the oxygen amount induces more compact and smoother $Ta_{1-x}O_x$ coatings. The non-usual formation of bcc α-Ta phase in the non-reactive Ta coating is explained by the application of negative bias during the deposition, which increases the bombarding particles energy leading in a second stage to an increase of the local temperature; when the oxygen was added, the crystalline structure changes to a mixture of phases. The coatings deposited close to the reactive mode threshold showed IR absorption bands corresponding to amorphous phase containing some crystals embedded onto the amorphous matrix. While for the coatings deposited in the poisoned regime, IR only indicates a marked amorphous structure. The changes in refractive index (between 2.09 and 2.27 at 0.65 μm) are typically correlated with modifications of density through the Lorentz equation, however, in this case it seems to be also correlated with the different crystallinity of the coatings, which is corroborated with the results obtained by FTIR.

Moreover, the synergy between the theoretical study based on *ab-initio* calculations of the structures and elastic properties of different Ta(O) phases and the SAW experimental results allow a better understanding of the relationships chain "deposition / crystal-structure versus specific elastic properties". For TO1 (11 at.% oxygen), when the oxygen was added, although the presence of a mixture of phases composed by α-Ta (bcc) and β-

Ta (tetragonal) could be accepted, *DFT* calculations seem to show other possible contribution. The remarkably stable Ta_4O structure may be seen as a bcc Ta with oxygen atoms in interstitial positions that also forms a tetragonal phase, which might be mistaken as a pure β-Ta phase by XRD. Thus, the high degree of crystal anisotropy with different elastic modulus in the three major crystallographic orientations (100, 110, 111) of Ta_4O phase allows to explain the unexpected high elastic modulus of TO1 coating. Increasing the oxygen content, the coatings become nanocrystalline and hence, a density decrease and elastic modulus increase is observed. *Ab-initio* calculations are in good agreement and reveal that an increased addition of oxygen to the Ta phase causes a decrease in the density of the crystal structures, explained by the incorporation of oxygen atoms into the Ta crystal structure leading to a distortion of the initial structure. Moreover, STEM/EDS analysis of TO3 and TO5 coatings (27 and 43 at.% oxygen, respectively) revealed a multilayer configuration that combined with the overall decrease in crystallinity of the coatings, explain elastic modulus increase. Finally, besides not being possible to certainly identify and differentiate the TaO_x stoichiometric (TaO_2 or Ta_2O_5) of the coating with the highest oxygen content (70 at.% oxygen – TO6) the low elastic modulus and density values allow to judge that has characteristics of a δ-Ta_2O_5 phase, supported of its high thermodynamically stability, low density and low elastic modulus, comparing the stoichiometric TaO_x phases, as estimated by *DFT* calculations.

3.6. References

[1]   K. Subramani and R. T. Mathew, "Chapter 6 - Titanium Surface Modification Techniques for Dental Implants—From Microscale to Nanoscale," in *Emerging Nanotechnologies in Dentistry*, K. Subramani and W. Ahmed, Eds., ed Boston: William Andrew Publishing, 2012, pp. 85-102.

[2]   J. Disegi, "Titanium alloys for fracture fixation implants", *Injury,* vol. 31, pp. D14-D17, 2000.

[3]   H. Rack and J. Qazi, "Titanium alloys for biomedical applications", *Materials Science and Engineering: C,* vol. 26, pp. 1269-1277, 2006.

[4]   S. E. Kim, J. H. Lim, S. C. Lee, S.-C. Nam, H.-G. Kang, and J. Choi, "Anodically nanostructured titanium oxides for implant applications", *Electrochimica Acta,* vol. 53, pp. 4846-4851, 2008.

[5]   A. Maho, S. Linden, C. Arnould, S. Detriche, J. Delhalle, and Z. Mekhalif, "Tantalum oxide/carbon nanotubes composite coatings on titanium, and their functionalization with organophosphonic molecular films: A high quality scaffold for hydroxyapatite growth", *Journal of Colloid and Interface Science,* vol. 371, pp. 150-158, 2012.

[6]   T. Miyazaki, H.-M. Kim, T. Kokubo, C. Ohtsuki, H. Kato, and T. Nakamura, "Mechanism of bonelike apatite formation on bioactive tantalum metal in a simulated body fluid", *Biomaterials,* vol. 23, pp. 827-832, 2002.

[7]   B. R. Levine, S. Sporer, R. A. Poggie, C. J. Della Valle, and J. J. Jacobs, "Experimental and clinical performance of porous tantalum in orthopedic surgery", *Biomaterials,* vol. 27, pp. 4671-4681, 2006.

[8]   V. K. Balla, S. Banerjee, S. Bose, and A. Bandyopadhyay, "Direct laser processing of a tantalum coating on titanium for bone replacement structures", *Acta Biomaterialia,* vol. 6, pp. 2329-2334, 2010.

[9]   C. J. Frandsen, K. S. Brammer, K. Noh, G. Johnston, and S. Jin, "Tantalum coating on TiO2 nanotubes induces superior rate of matrix mineralization and osteofunctionality in human osteoblasts", *Materials Science and Engineering: C,* vol. 37, pp. 332-341, 2014.

[10]   Y. Leng, J. Chen, P. Yang, H. Sun, J. Wang, and N. Huang, "The biocompatibility of the tantalum and tantalum oxide films synthesized by pulse metal vacuum arc source deposition", *Nuclear Instruments and Methods in Physics Research Section B: Beam Interactions with Materials and Atoms,* vol. 242, pp. 30-32, 2006.

[11]   W. Yang, Y. Liu, Q. Zhang, Y. Leng, H. Zhou, P. Yang, J. Chen, and N. Huang, "Biomedical response of tantalum oxide films deposited by DC reactive unbalanced magnetron sputtering", *Surface and Coatings Technology,* vol. 201, pp. 8062-8065, 2007.

[12]   T. Kokubo, T. Matsushita, H. Takadama, and T. Kizuki, "Development of bioactive materials based on surface chemistry", *Journal of the European Ceramic Society,* vol. 29, pp. 1267-1274, 2009.

[13]   C. Arnould, T. Korányi, J. Delhalle, and Z. Mekhalif, "Fabrication of tantalum oxide/carbon nanotubes thin film composite on titanium substrate", *Journal of colloid and Interface Science,* vol. 344, pp. 390-394, 2010.

[14]   N. Wang, H. Li, J. Wang, S. Chen, Y. Ma, and Z. Zhang, "Study on the anticorrosion, biocompatibility, and osteoinductivity of tantalum decorated with tantalum oxide nanotube array films", *ACS Applied Materials & Interfaces,* vol. 4, pp. 4516-4523, 2012.

[15]   Y.-S. Sun, J.-H. Chang, and H.-H. Huang, "Corrosion resistance and biocompatibility of titanium surface coated with amorphous tantalum pentoxide", *Thin Solid Films,* vol. 528, pp. 130-135, 2013.

[16]   R. Hollerweger, D. Holec, J. Paulitsch, R. Rachbauer, P. Polcik, and P. Mayrhofer, "Magnetic field strength influence on the reactive magnetron sputter deposition of Ta2O5", *Journal of Physics D: Applied Physics,* vol. 46, p. 335203, 2013.

[17]   D. Depla, J. Haemers, and R. De Gryse, "Discharge voltage measurements during reactive sputtering of oxides", *Thin Solid Films,* vol. 515, pp. 468-471, 2006.

[18]   J. A. Thornton, "High rate thick film growth", *Annual review of materials science,* vol. 7, pp. 239-260, 1977.

[19]   F. Guimarães, C. Oliveira, E. Sequeiros, M. Torres, M. Susano, M. Henriques, R. Oliveira, R. Escobar Galindo, S. Carvalho, N. M. G. Parreira, F. Vaz, and A. Cavaleiro, "Structural and Mechanical properties of Ti–Si–C–ON for biomedical applications", *Surface and Coatings Technology,* vol. 202, pp. 2403-2407, 2008.

[20]   L. Gladczuk, A. Patel, C. Singh Paur, and M. Sosnowski, "Tantalum films for protective coatings of steel", *Thin Solid Films,* vol. 467, pp. 150-157, 2004.

[21]   M. Chandrasekhar, S. J. Chandra, and S. Uthanna, "Characterization of bias magnetron sputtered tantalum oxide films for capacitors", *Indian Journal of Pure & Applied Physics,* vol. 47, pp. 49-53, 2009.

[22]   Y. Zhou, Z. Xie, H. Xiao, P. Hu, and J. He, "Effects of deposition parameters on tantalum films deposited by direct current magnetron sputtering", *Vacuum,* vol. 83, pp. 286-291, 2009.

[23]   Y. Zhou, Z. Xie, H. Xiao, P. Hu, and J. He, "Effects of deposition parameters on tantalum films deposited by direct current magnetron sputtering in Ar–O2 mixture", *Applied Surface Science,* vol. 258, pp. 1699-1703, 2011.

[24]   R. Knepper, B. Stevens, and S. P. Baker, "Effect of oxygen on the thermomechanical behavior of tantalum thin films during the β–α phase transformation", *Journal of applied physics,* vol. 100, pp. 123508-11, 2006.

[25]   H.-E. Cheng and C.-T. Mao, "The effect of substrate temperature on the physical properties of tantalum oxide thin films grown by reactive radio-frequency sputtering", *Materials Research Bulletin,* vol. 38, pp. 1841-1849, 2003.

[26]   E. Atanassova and D. Spassov, "X-ray photoelectron spectroscopy of thermal thin Ta 2 O 5 films on Si", *Applied surface science,* vol. 135, pp. 71-82, 1998.

[27]   O. Kerrec, D. Devilliers, H. Groult, and P. Marcus, "Study of dry and electrogenerated Ta 2 O 5 and Ta/Ta 2 O 5/Pt structures by XPS", *Materials Science and Engineering: B,* vol. 55, pp. 134-142, 1998.

[28]   E. Atanassova, G. Tyuliev, A. Paskaleva, D. Spassov, and K. Kostov, "XPS study of N 2 annealing effect on thermal Ta 2 O 5 layers on Si", *Applied surface science,* vol. 225, pp. 86-99, 2004.

[29]   B. Díaz, J. Światowska, V. Maurice, M. Pisarek, A. Seyeux, S. Zanna, S. Tervakangas, J. Kolehmainen, and P. Marcus, "Chromium and tantalum oxide nanocoatings prepared by filtered cathodic arc deposition for corrosion protection of carbon steel", *Surface and Coatings Technology,* vol. 206, pp. 3903-3910, 2012.

[30]   J.-Y. Zhang and I. W. Boyd, "Thin tantalum and tantalum oxide films grown by pulsed laser deposition", *Applied surface science,* vol. 168, pp. 234-238, 2000.

[31]   E. Atanassova, T. Dimitrova, and J. Koprinarova, "AES and XPS study of thin RF-sputtered Ta 2 O 5 layers", *Applied surface science,* vol. 84, pp. 193-202, 1995.

[32]   Y. Masuda, S. Wakamatsu, and K. Koumoto, "Site-selective deposition and micropatterning of tantalum oxide thin films using a monolayer", *Journal of the European Ceramic Society,* vol. 24, pp. 301-307, 2004.

[33]   T. Tsuchiya, H. Imai, S. Miyoshi, P.-A. Glans, J. Guo, and S. Yamaguchi, "X-Ray absorption, photoemission spectroscopy, and Raman scattering analysis of amorphous tantalum oxide with a large extent of oxygen nonstoichiometry", *Physical Chemistry Chemical Physics,* vol. 13, pp. 17013-17018, 2011.

[34]   A. Muto, F. Yano, Y. Sugawara, and S. Iijima, "The study of ultrathin tantalum oxide films before and after annealing with X-ray photoelectron spectroscopy", *Japanese journal of applied physics,* vol. 33, p. 2699, 1994.

[35]   S. Chandra, S. Uthanna, and G. M. Rao, "Effect of substrate temperature on the structural, optical and electrical properties of dc magnetron sputtered tantalum oxide films", *Applied Surface Science,* vol. 254, pp. 1953-1960, 2008.

[36]   H. Ono and K.-i. Koyanagi, "Infrared absorption peak due to Ta= O bonds in Ta 2 O 5 thin films", *Applied physics letters,* vol. 77, pp. 1431-1433, 2000.

[37]   A. Huang, S. Xu, M. Zhu, B. Wang, H. Yan, and T. Liu, "Crystallization control of sputtered Ta 2 O 5 thin films by substrate bias", *Applied physics letters,* vol. 83, pp. 3278-3280, 2003.

[38]   A. Huang and P. K. Chu, "Crystallization improvement of Ta 2 O 5 thin films by the addition of water vapor", *Journal of Crystal Growth,* vol. 274, pp. 73-77, 2005.

[39]   J. Capilla, J. Olivares, M. Clement, J. Sangrador, E. Iborra, and A. Devos, "Characterization of amorphous tantalum oxide for insulating acoustic mirrors", in *Frequency Control and the European Frequency and Time Forum (FCS), 2011 Joint Conference of the IEEE International*, 2011, pp. 1-6.

[40]   Y. J. Cho, N. Nguyen, C. Richter, J. Ehrstein, B. H. Lee, and J. C. Lee, "Spectroscopic ellipsometry characterization of high-k dielectric HfO 2 thin films and the high-

temperature annealing effects on their optical properties", *Applied physics letters,* vol. 80, pp. 1249-1251, 2002.

[41]   H. Chen and W. Shen, "Perspectives in the characteristics and applications of Tauc-Lorentz dielectric function model", *The European Physical Journal B-Condensed Matter and Complex Systems,* vol. 43, pp. 503-507, 2005.

[42]   L. Pereira, H. Aguas, E. Fortunato, and R. Martins, "Nanostructure characterization of high k materials by spectroscopic ellipsometry", *Applied surface science,* vol. 253, pp. 339-343, 2006.

[43]   V. Assunção, E. Fortunato, A. Marques, A. Gonçalves, I. Ferreira, H. Águas, and R. Martins, "New challenges on gallium-doped zinc oxide films prepared by rf magnetron sputtering", *Thin Solid Films,* vol. 442, pp. 102-106, 2003.

[44]   J. Price, P. Hung, T. Rhoad, B. Foran, and A. Diebold, "Spectroscopic ellipsometry characterization of Hf x Si y O z films using the Cody–Lorentz parameterized model", *Applied physics letters,* vol. 85, pp. 1701-1703, 2004.

[45]   K. Kukli, J. Aarik, A. Aidla, O. Kohan, T. Uustare, and V. Sammelselg, "Properties of tantalum oxide thin films grown by atomic layer deposition", *Thin Solid Films,* vol. 260, pp. 135-142, 1995.

[46]   C. Corbella, M. Vives, A. Pinyol, I. Porqueras, C. Person, and E. Bertran, "Influence of the porosity of RF sputtered Ta 2 O 5 thin films on their optical properties for electrochromic applications", *Solid State Ionics,* vol. 165, pp. 15-22, 2003.

[47]   X. He, J. Wu, L. Zhao, J. Meng, X. Gao, and X. Li, "Synthesis and optical properties of tantalum oxide films prepared by ionized plasma-assisted pulsed laser deposition", *Solid State Communications,* vol. 147, pp. 90-93, 2008.

Chapter 4

Biocorrosion validation of Ta$_{1-x}$O$_x$ coatings

The following chapter is partially based on the results published in:

- C. F. Almeida Alves, S. Calderon V, D. Dias and S. Carvalho; "*Influence of oxygen content on the electrochemical behavior of Ta$_{1-x}$O$_x$ coatings*" Electrochimica Acta, 211 (2016) 385-394.

4.1. Introduction

The degradation of metallic dental implants is a common process caused by the physiological environment that surrounds the implant. Thus, additionally to enhanced bioactivity, it is mandatory to ensure good corrosion properties to obtain an appropriate coating performance. In this context, corrosion resistance is evaluated in order to validate the application of these coatings in metallic implants when exposed to aggressive oral environments.

In this regard, several electrochemical tests can simulate that physiological environment and can help on evaluating and understanding the corrosion properties of the developed material. The corrosion processes are commonly reported as charge and mass transference with a simultaneously anode oxidation and cathode reduction. Thus, the charge transfer must be measured, in a DC or AC mode, aiming to evaluate the corrosion of a material in a wide range of electrolytes. The potentiodynamic curves allow to analyze the corrosion and the breakdown potential; and the electrochemical impedance spectroscopy (EIS) tests allows to determine the polarization resistance of the materials. Furthermore, from the EIS data fitting obtained, it is possible to gather a set of parameters, which are correlated with the sample morphology and structure. Potentiodynamic tests are a destructive method due to the high potential applied, while the EIS is nondestructive one due to the small amplitude of the signals used during the measurement [1].

The electrochemical tests were performed in six samples, CP Ti Gr2, SS 316L, Ta1, TO1 TO5 and TO6; the first two serving as control samples, while the remaining four coatings correspond to the proposed bioactive surfaces.

4.2. Materials and methods

The corrosion performance was assessed by an open circuit potential (OCP), EIS and anodic potentiodynamic polarization experiments. The apparatus for electrochemical measurement consists of a Gamry REF600 potenciostat controlled by EIS300 and DC105 software. Electrochemical experiments were carried out with a standard three-electrode

cell. A saturated calomel electrode (SCE) was used as the reference electrode with a Pt counter electrode and the SS 316L sample coated with $Ta_{1-x}O_x$ coating as the working electrode, with an exposed area of 0.44 cm^2. The experiments were performed on CP Ti Gr2 (ASTM: F67) as a commercial surface control, on SS 316L as surface control and on $Ta_{1-x}O_x$ coatings as new developed surfaces. Each sample was immersed into a volume of 200 mL of Fusayama artificial saliva (0.4 wt.% NaCl; 0.4 wt.% KCl; 0.795 wt.% $CaCl_2.2H_2O$; 0.005 wt.% $Na_2S.9H_2O$; 0.69wt.% $NaH_2PO_4.2H_2O$; and 1 wt.% Urea) with stabilized pH at 5.5 in equilibrium with air. The tests were performed at room temperature under static conditions. Three measurements were performed for each sample to statistically validate the results. OCP and EIS experiments were carried out as a function of the immersion time after 2, 24 hours and 7 days. Before each impedance experiment, a stable OCP potential was achieved during 1 hour for the first measurement and 30 min for the following measurements. Thereafter, EIS experiments were carried out with a sinusoidal AC perturbation of 10 mV (rms) amplitude around the open circuit potential applied to the electrode over the frequency range 0.001 Hz to 1 MHz. After 7 days of immersion, potentiodynamic tests were carried out using a scanning rate of 60 mV/min from -0.3 V vs. OCP to + 1.2 V vs OCP. Potentiodynamic tests were also conducted at 0 hours of immersion, allowing OCP primary stabilization, in order to study the influence of the immersion time on the electrochemical response.

4.3. Corrosion behavior

4.3.1. Corrosion resistance evaluation

The OCP evolution during 1 hour of immersion is plotted in Figure 4.1.a, showing a stable electrochemical system after this period of time. The Ta1 sample shows an OCP value between -350 and -400 mV vs. SCE. The TO1 and TO5 sub-stoichiometric coatings showed the lowest OCP values, even lower than Ta1 coating. In fact, these coatings revealed to have a mixture of phases, while Ta1 coating evidences a pure α-Ta phase. This suggests that the mixture of phases have an adverse effect in OCP of the coatings. For instance, β-Ta phase shows a lower OCP, and hence, the mixed potential is reduced, causing an increase of the susceptibility for corrosion. TO6 coating, on the other hand, shows the

highest OCP value around -100 and -80 mV vs. SCE, due to the higher oxygen content that allow the formation of a stable stoichiometric oxide, which has better performance against corrosion. Figure 4.1.b shows the OCP as a function of immersion time of $Ta_{1-x}O_x$ coatings in artificial saliva at room temperature after 2 h, 24 h and 7 days. The values reveal that the Ta-based samples exhibit very stable OCP. The coatings with higher oxygen content show a slight overall increase of the OCP values after 7 days of immersion, which may indicate that dense oxide layers favor the increase of the energy barrier needed to suffer corrosion.

a)

b)
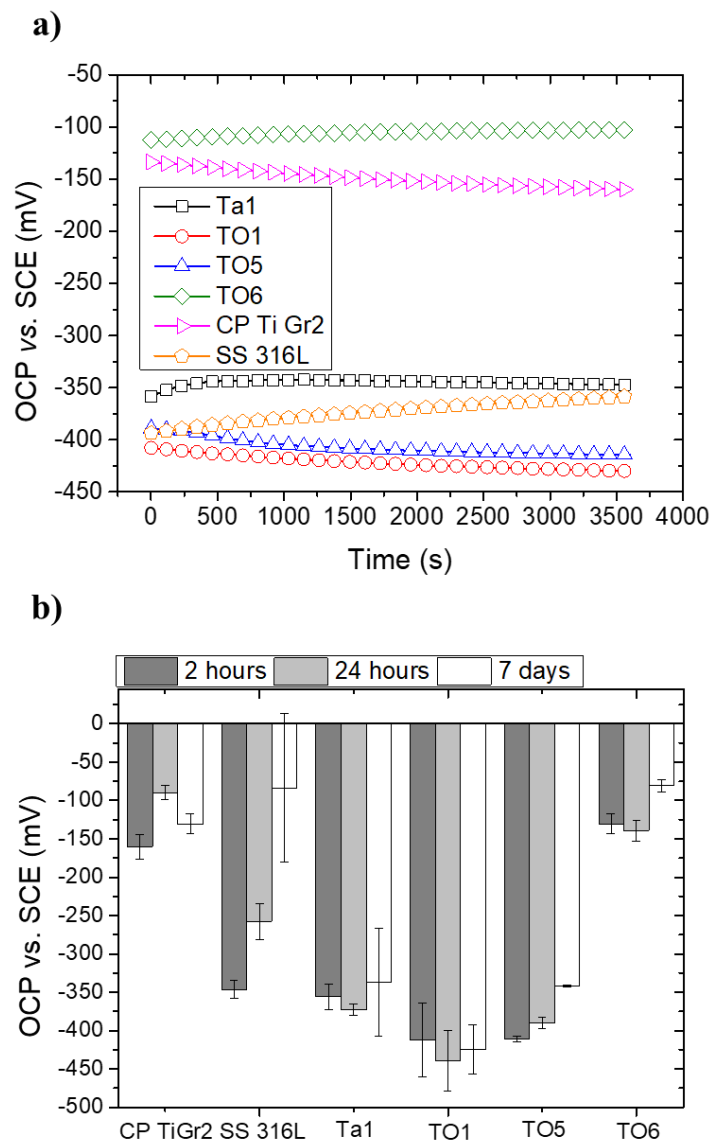
Figure 4.1: (a) OCP evolution of CP Ti Gr2, SS 316L and $Ta_{1-x}O_x$ samples immersed during 1h in artificial saliva at room temperature. The graphic profiles depicted above are representative of the undertaken measurements; (b) OCP as a function of immersion time of CP Ti Gr2, SS 316L and $Ta_{1-x}O_x$ samples immersed in artificial saliva at room temperature. The results are an average calculated from three different samples.

Figure 4.2 shows the size distribution of the surface defects calculated from optical micrographs. The defects are usually identified as pin-holes and/or droplets associated to the sputtering process. The number of defects is evidently reduced both in the histogram and the surface micrographs when oxygen is incorporated (see Figure 4.2) attributed to a morphology densification due to a more compact growth, as demonstrated by SEM surface images.
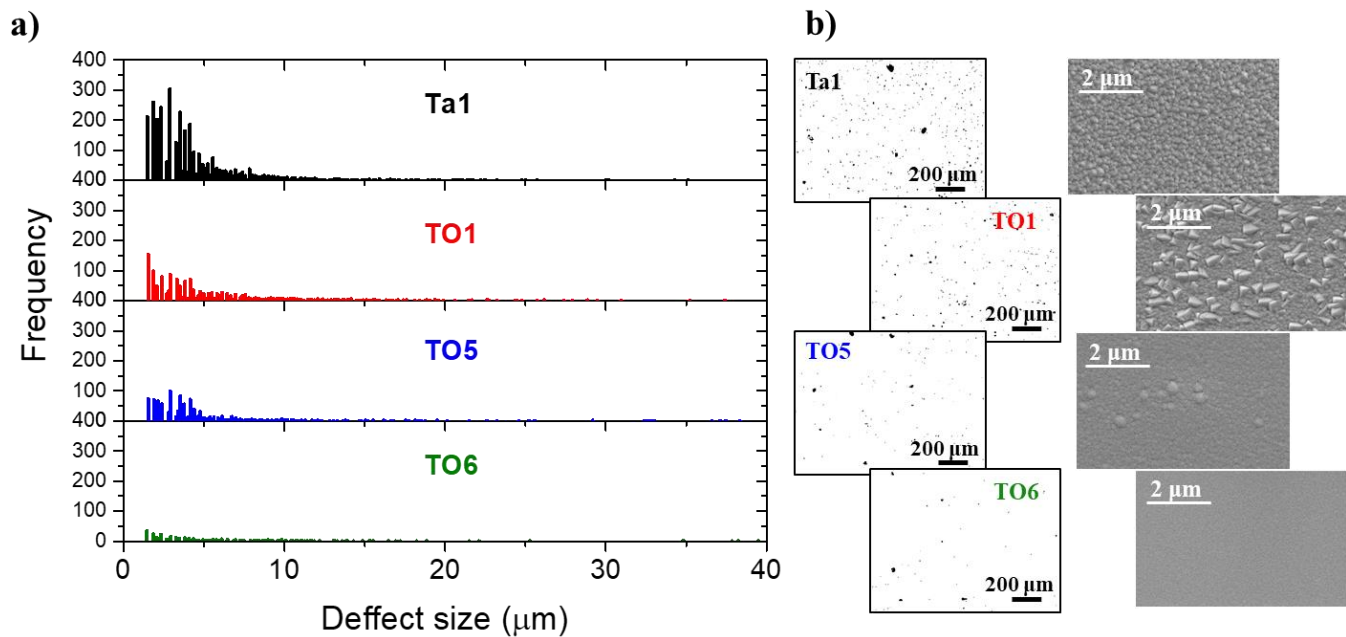
Figure 4.2: (a) Defects histogram analysis of $Ta_{1-x}O_x$ coatings as a function of oxygen content, calculated with the ImageJ software using the optical micrographs; and (b) Optical and TOP view SEM micrographs (8bits) of the as-deposited coatings on SS 316L.

The potenciodynamic curves, 0 and 7 days after immersion, are plotted in Figure 4.3. Localized corrosion protection is expected to be effective for compact morphologies (*i.e.* higher oxygen content), where the penetration of the electrolyte can be more largely avoided, preventing the contact with the SS 316L. Thus, large defects or damage to the coatings must be avoided to maintain this protection. In effect, in all samples, pitting (metastable pitting) or localized corrosion is not observed, except for the bare SS 316L wherein the breakdown potential (E_b) occurs at around 550 mV vs. SCE, revealing a protective behavior of the coatings for polarization induced corrosion of SS 316L, matching the performance of the CP Ti Gr2.

a)

b)
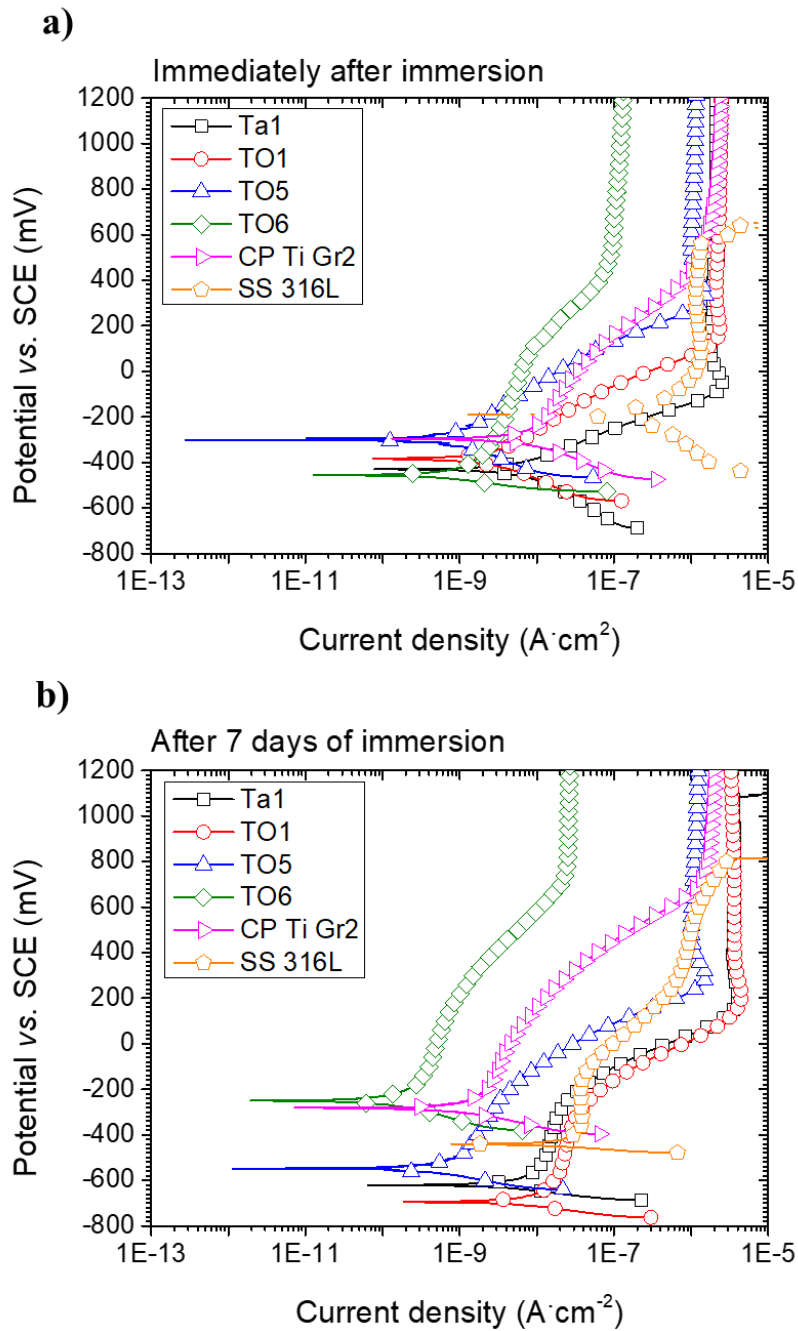
Figure 4.3: Potenciodynamic curves of CP Ti Gr2, SS 316L and Ta$_{1-x}$O$_x$ samples: (a) immediately; and (b) after 7days; of immersion on artificial saliva at room temperature.

The potendiodynamic curves immediately after immersion also reveal that the coatings with higher oxygen content (TO5 and TO6) possess lower current density, indicating that corrosion occurs at slower rates, when compared to the other samples. These results are

in agreement with the SEM and MO results, where these coatings present lower number of superficial defect, as shown in Figure 4.2. For low oxygen content coatings, the anodic branch of the potentiodynamic test shows similar kinetic, where the slope of the curves is similar between each other, indicating larger electrochemical activity of these coatings, likely due to the presence of a higher number of surface defects and more metallic Ta.

After 7 days of immersion the potenciodynamic curves evidence some changes. Almost all the samples present a more passive behavior compared to the curves immediately after immersion and a tendency widespread reduction of the current density, compared to the initial behavior. This indicates that after 7 days of immersion a protective layer is formed on the samples surface. Coatings with low content of oxygen still present the highest corrosion rate, attributed to a more metallic Ta composition of the coatings and subsequently higher number of defects. Thus, increasing the immersion time, the artificial saliva penetrates progressively throughout the porosity and the superficial defects, increasing the exposed area. The more columnar-like morphology and higher number of defects observed in the low oxygen content coatings accelerates the electrolyte intake, slowing down the reduction of the current density since the exposed area is increasing, while on the other coatings, a more compact morphology and less superficial defects help to block the electrolyte penetration, as well as, less active electrochemical behavior.

Electrochemical impedance spectroscopy was performed to characterize in detail the corrosion performance of the samples. Figure 4.4 shows the Bode and Nyquist plots for all the samples immediately after and 7 days after immersion.
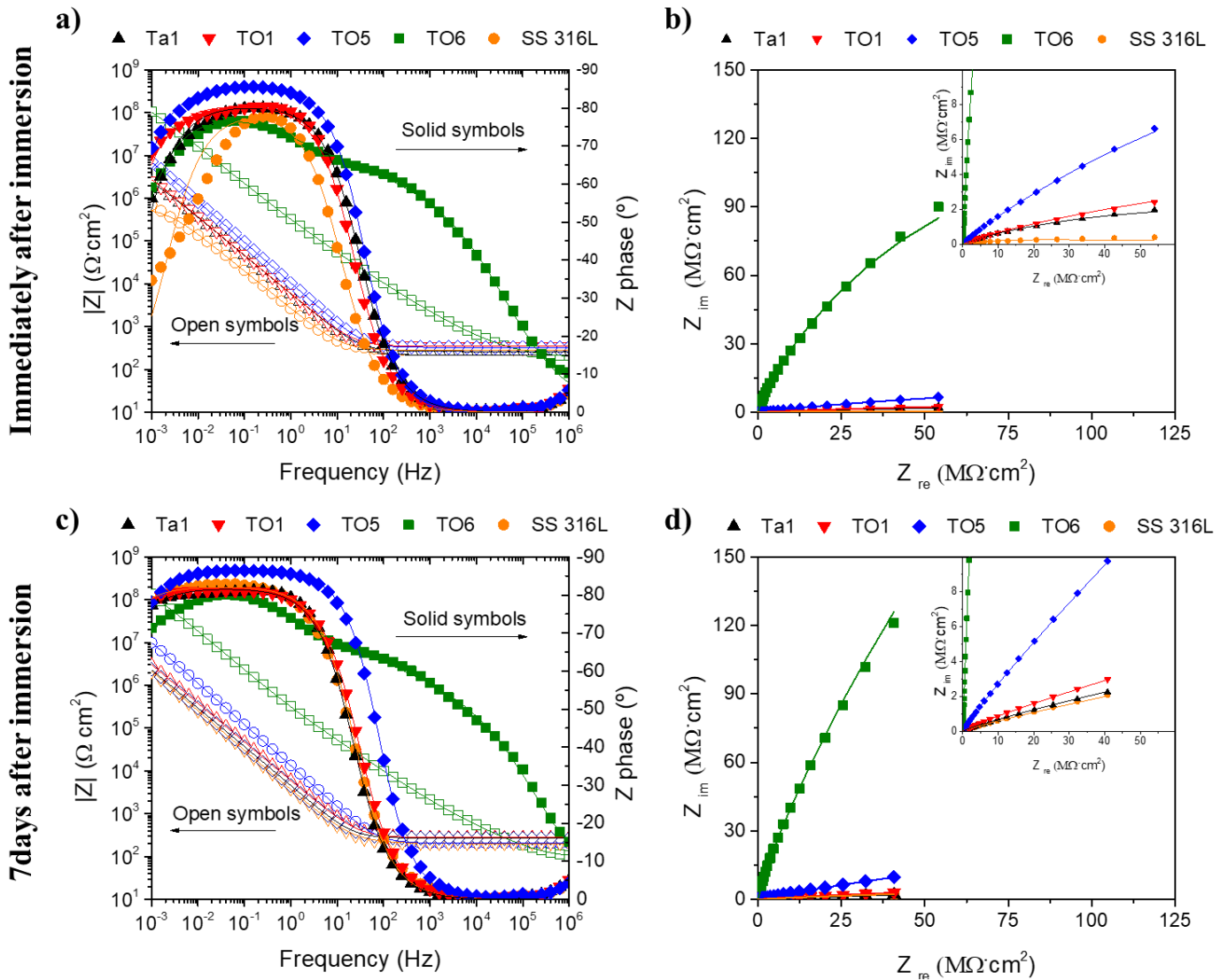
Figure 4.4: Bode (a and c) and Nyquist (b and d) plot of SS 316L and Ta$_{1-x}$O$_x$ samples immediately after (a and b) and 7 days after (c and d) of immersion on artificial saliva at room temperature. (Measured (dots) and fitted (lines) values of the impedance module are related to the left axis while the measured (dots) and fitted (lines) values of phase are related to the right axis).

The impedance results reveal larger impedance as oxygen increases in the coatings. This effect is clearly seen in the Nyquist plot shown in Figure 4.4.b) and Figure 4.4.d), where the TO6 possesses the highest impedance values. All the samples show a capacitive behavior with a single time constant, apart from the TO6 that displays a double time constant behavior, as shown in the phase angle curves present in Figure 4.4.a) and Figure

4.4.c). A more capacitive-like behavior is observed as a function of the immersion time, seen in the increment of the imaginary part of the impedance and the phase at lower frequency values, as shown in Figure 4.5. The increment indicates an enhanced protective behavior of the samples, due to the passivation of the coatings, which increases the charge transfer resistance of the coating during the corrosion process.
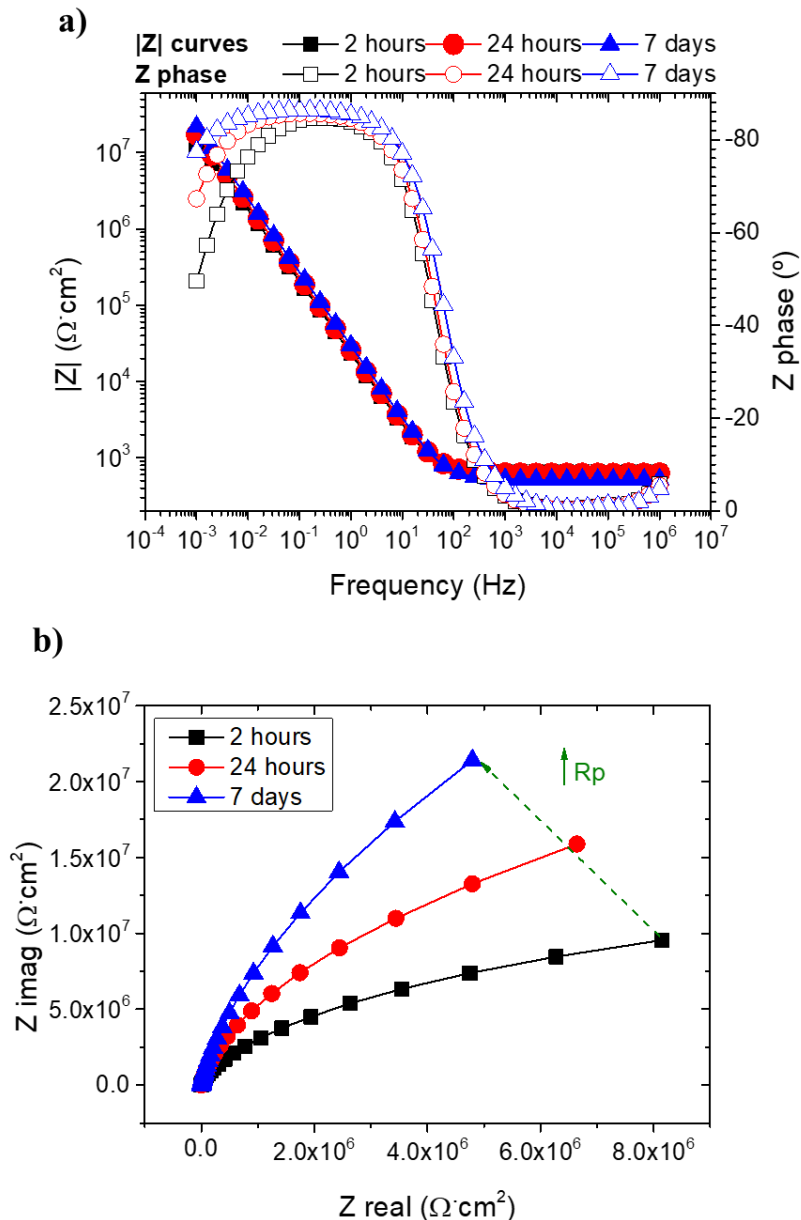
Figure 4.5: (a) Bode and (b) Nyquist plot of TO5 sample as a function of immersion time on artificial saliva at room temperature. (Measured (dots) and fitted (lines) values of the impedance module are related to the left axis while the measured (dots) and fitted (lines) values of phase are related to the right axis).

After 7 days of immersion, Ta1 and TO1 samples display a very similar electrochemical response, which mimics the SS 316L, as observed in Figure 4.4.c), where the impedance modulus and phase overlap among the three samples. This indicates that the open columnar morphology of these coatings allows the electrolyte to penetrate until the substrate, and thus, the electrochemical response is governed by the substrate. On the other hand, the coatings with higher oxygen amount show a distinctive performance, enhancing the corrosion resistance of the substrate. TO5, for instance, possesses higher impedance, and phase values compared to the previously mentioned samples, whereas TO6 shows a broader capacitive behavior and higher impedance values in the entire frequencies spectrum studied, indicating a more protective film.

In order to be able to quantify the electrochemical process, EIS results were fitted using two equivalent circuits (EC) shown in Figure 4.6. Figure 4.6.a) represent the model used to fit SS 316L, Ta1, TO1 and TO5, where a constant phase element (CPE) is used to replace the capacitance element, to consider the surface roughness and heterogeneities. This element simulates the series combination of the double-layer and film capacitive behavior at the film/electrolyte interface. The Rp, known as polarization resistance element, represents the charge transfer resistance. In the EC adopted for TO6, the first capacitive loop represents the TaO_x layer, while the second corresponds to the double-layer capacitance and charge transfer resistance at the interface between TO6 and the metallic portion (Ta and SS 316L), as described in Figure 4.6.b). It must be stressed that despite TO1 and TO5 coatings also possess a Ta interface, the absence of the electrochemical response of these layers may be due to the existence of metallic Ta in the functional layers, which hinder the differentiation between the coatings (TO1 and TO5), interlayer and substrate, and hence, a single time constant is observed in these samples (*cf.* Figure 4.4.c).
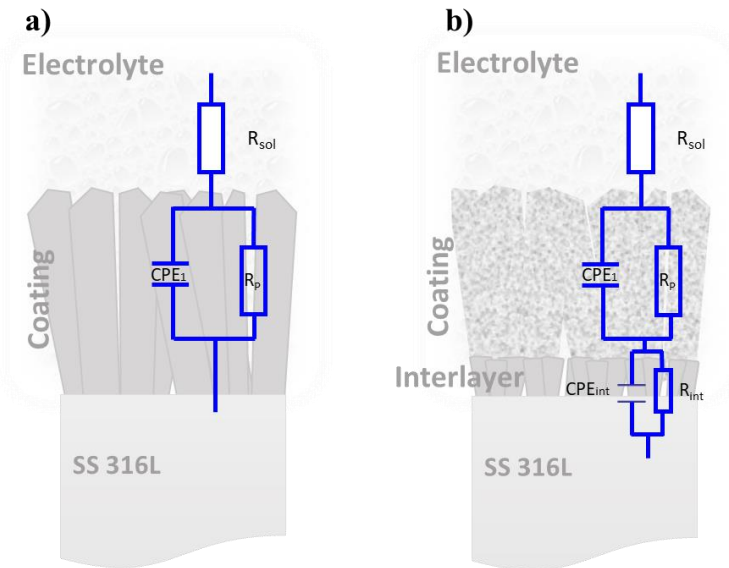
Figure 4.6: Scheme of equivalent circuit models used for fitting the EIS data. The Rsol represents the electrolyte resistance, the Rp represents the transference charge resistance of material and CPE represents the constant phase replacing a capacitance element.

The evolution of the polarization resistance in the samples is plotted in Figure 4.7, demonstrating a rise as a function of immersion time, validating once more the passivation of the surface. In addition, for TO6 the tendency may indicate obstruction of the diffusion path that contribute to the charge transfer in the system, due to passive film. For Ta1, TO1 and TO5 the consumption of free species, such as Ta, and hence, its passivation also causes a slightly obstruction of the diffusion path in the coatings. However, the high number of surface defects in Ta1 and TO1 samples allows artificial saliva to progressively penetrate, explaining the similarities in the electrochemical response between these two samples and SS 316L.
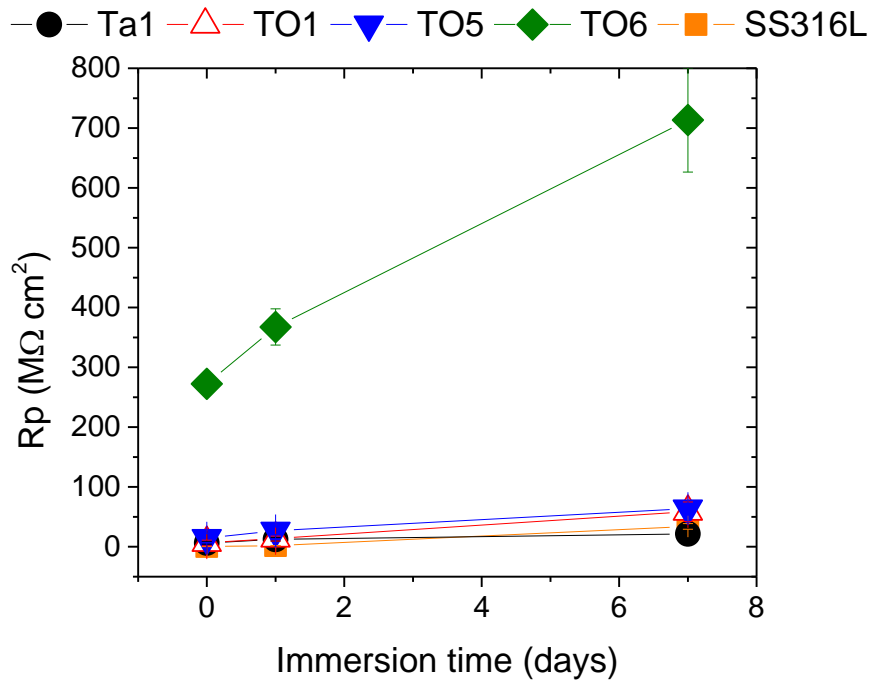
Figure 4.7: Evolution of the polarization resistance of SS 316L and Ta$_{1-x}$O$_x$ coatings as a function of immersion time, on artificial saliva at room temperature.

For clarity, Table 4.1 only shows the fitting results of EIS data after 7 days of immersion. The coatings with higher oxygen content reveal a larger polarization resistance (Rp), in agreement with the potentiodynamic tests. TO1 and TO5 show Rp values two or three folds higher than Ta1 and SS 316L samples, while TO6 has almost one order of magnitude difference. Once the electrochemical response demonstrates that the stoichiometric oxide (TO6 coating) exhibit a lower electrochemical activity in artificial saliva solution, due to the stability of the oxide phase in the coating, whereas in sub-stoichiometric oxides and Ta coatings the metallic tantalum species contributes to anodic reaction while oxidizes, reducing the stability of the coatings.

Additionally, a progressive decrease of the Q parameter in the CPE compared to the control sample (SS 316L) is observed. Although this parameter does not directly represent the capacitance of the system, an effective capacitance may be calculated using the Equation 4.1 [2].

Equation 4.1

$$C_{eff} = \frac{(Q \cdot R_p)^{\frac{1}{n}}}{R_p}$$

where **Q** and n are mathematical constants of the **CPE** impedance (for a pure capacitor elements **Q**= capacitance and **n**=1) and **Rp** is polarization resistance.

Table 4.1 shows a reduction of the effective capacitance of the system with the increase of the oxygen, due to a more ceramic behavior of the coatings, which reduces the formation of a double layer capacitance and reduces the overall capacitance due to the increase of the thickness in the dielectric materials (*i.e.* Ta_2O_5), as schematize in Figure 4.8.
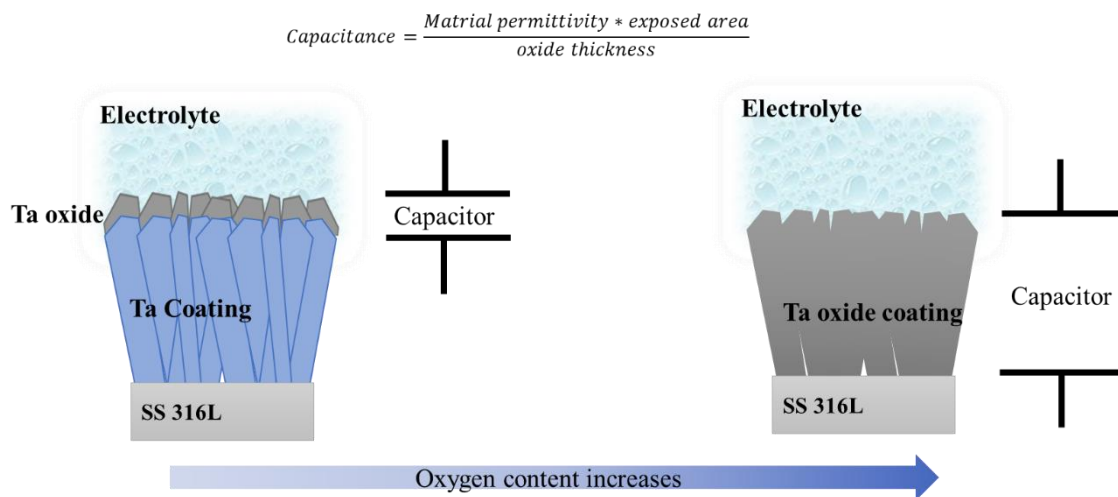
Figure 4.8: Schematic representation of the evolution of the capacitor as a function of oxygen content.

Table 4.1: EIS fitting parameters of SS 316L and $Ta_{1-x}O_x$ samples after 7days of immersion on artificial saliva at room temperature. The results are standard deviations calculated based on experimental data of three separate samples.

Sample	R_{sol} ($\Omega \cdot cm^2$)	R_p ($M\Omega \cdot cm^2$)	Q ($\mu S \cdot s^n \cdot cm^{-2}$)	n	C_{eff} $\mu F \cdot cm^{-2}$	R_{pint} ($k\Omega \cdot cm^2$)	Q_{int} ($\mu S \cdot s^\alpha \cdot cm^{-2}$)	n_{int}
SS 316L	169 ± 50	34.0 ± 4.7	40.4 ± 12.8	0.92 ± 0.01	78.5 ± 30.7	-	-	-
Ta1	209 ± 75	22.7 ± 14.1	24.0 ± 21.1	0.92 ± 0.01	70.6 ± 21.8	-	-	-
TO1	257 ± 45	58.6 ± 16.3	40.3 ± 8.43.71	0.89 ± 0.01	103.0 ± 35.0	-	-	-
TO5	216 ± 17	64.0 ± 6.5	13.0 ± 0.2	0.96 ± 0.00	17.3 ± 0.3	-	-	-
TO6	81 ± 2	714 ± 87.0	0.65 ± 0.08	0.89 ± 0.00	1.4 ± 0.14	73.5 ± 17.9	4.57 ± 0.22	0.56 ± 0.00

All the models showed a goodness of fit between 3.2 x 10 $^{-4}$ and 8.8 x 10 $^{-4}$.

4.3.2. Corrosion protection mechanism

In order to better understand the protection mechanism of the surface, XPS studies were performed before and after 7 days of immersion (at OCP potential) to identify the chemical bonds present in the as-deposited coatings and after 7 days of immersion on artificial saliva at room temperature. XPS analysis was performed in two samples, Ta1 and TO6 since these two coatings presented the threshold values measured by EPMA for the chemical composition, with highest tantalum or oxygen content, respectively.

It is important to remember that, Ta element can assume different oxidation states as Ta^{5+}, Ta^{4+}, Ta^{2+}, Ta^+ and Ta^0 depending on the oxide type formed. Each oxidation state is characterized in Ta 4f spectra by a spin-orbital doublet (Ta 4f 7/2 and Ta 4f 5/2), frequently separated by 1.9 eV [3]. The XPS results of Ta1 and TO6 coatings, before and after immersion, are shown in Figure 4.9.
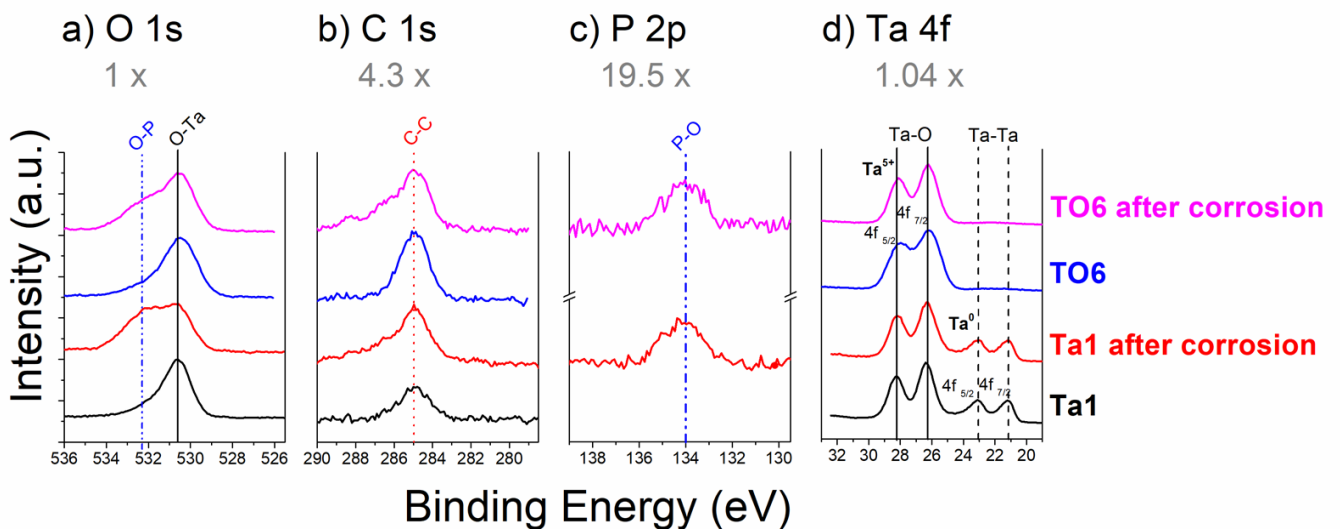
Figure 4.9: XPS spectra of (a) O 1s, (b) C 1s, (c) P 2p and (d) Ta 4f of $Ta_{1-x}O_x$ coatings, before and after 7 days of immersion on artificial saliva at room temperature.

Ta 4f photoemission spectrum at the coatings surface shows the spectral doublet around 26.3 (4f 7/2) and 28.2 (4f 5/2) eV for both analyzed coatings, before and after immersion. The binding energies of this doublet correspond to Ta_2O_5, indicating that the Ta atoms are

positively charged in Ta^{5+} oxidation state relatively to Ta metal, due to the bonding of these atoms with oxygen [4]. This bond is confirmed by the O 1s peak nearby 530.6 eV that corresponds to the O-Ta chemical bonding (Figure 4.9.a), according with the literature [5]. The appearance of Ta 4f doublet assigned to Ta_2O_5 for as-deposited Ta1 coating demonstrates the high tendency of Ta to form a protective layer. Contrary to TO6, Ta1 displays an additional doublet around 21.1 and 23.0 eV, corresponding to the binding energies of Ta^0, suggesting that the surface is composed by a mixture of pure metal and oxide. This mixture is likely to be due to a very thin protective layer of Ta_2O_5 and the metallic state underneath the oxide. Hence, the more passive behavior of TO6 observed in the potentiodynamic tests can be attributed to a pure oxide composition on the surface of the coatings, while coatings with lower content of oxygen such Ta1 displays both TaO_x and metallic Ta, exhibiting a more active electrochemical behavior.

It must be stressed that the growth of the oxide layer on Ta1 coatings is not observed, since the ratio between the Ta^{+5} and Ta^0 before and after immersion is maintained, indicating that an additional parameter contributes to the corrosion protection of the coatings. Such protection is attributed to the formation of Ta-O-P layer, as seen in Figure 4.9.c). In effect, it has been reported that the phosphate ions can bind with metal oxides and form phosphates [6]. These phosphates ions are known as excellent inorganic corrosion inhibitors that provide protection to a surface susceptible to suffer corrosion [7, 8].

The small peak around 532.3 eV in O 1s spectrum of the immersed coatings is attributed to the surface protection (O-P). It is important to note that the appearance of this minor peak is caused by the incorporation of a small amount of phosphorus in the top layer coating and can be confirmed by the P 2p observed peak at 134.0 eV that correspond to the P-O chemical bond [9], confirming the formation of a Ta-O-P protective layer.

4.4. Partial conclusions

SEM, optical micrographs and XPS analysis have been combined with potenciodynamic and EIS electrochemical analysis aiming at investigate the corrosion/electrochemical

stability and enhancement of the stainless steel 316L performance, provided by $Ta_{1-x}O_x$ coatings deposited by reactive magnetron sputtering. The assessment of sputtered Ta-based coatings reveals more compact coatings with morphology densification as oxygen amounts increase, showing smoother surfaces. Surface defects analysis revealed that the number of defects is reduced when oxygen is incorporated, attributed to denser coatings.

The electrochemical response evidenced a protective behavior of the films for polarization induced corrosion of SS 316L, matching the performance of the CP Ti Gr2. A progressive increase in the corrosion resistance as a function of the immersion time in all the coatings, attributed to the protection of the surface by both Ta_2O_5 and Ta-O-P formation is also observed. A more capacitive-like behavior is detected as a function of the immersion time highlighting the enhanced protective behavior of the coatings.

More specifically, electrochemical response demonstrates that the stoichiometric oxide (TO6 coating) exhibit a lower electrochemical activity in artificial saliva solution, reaching the best corrosion performance.

4.5.   References

[1]   S. C. Velasco, "Production and characterization of ZrCN-Ag coatings deposited by magnetron sputtering", PhD in Materials Engineering, University of Minho, Braga, Portugal, 2016.

[2]   T. Tsuchiya, H. Imai, S. Miyoshi, P.-A. Glans, J. Guo, and S. Yamaguchi, "X-Ray absorption, photoemission spectroscopy, and Raman scattering analysis of amorphous tantalum oxide with a large extent of oxygen nonstoichiometry", *Physical Chemistry Chemical Physics,* vol. 13, pp. 17013-17018, 2011.

[3]   C. Mansilla, "Structure, microstructure and optical properties of cerium oxide thin films prepared by electron beam evaporation assisted with ion beams", *Solid State Sciences,* vol. 11, pp. 1456-1464, 2009.

[4]   B. Díaz, J. Światowska, V. Maurice, M. Pisarek, A. Seyeux, S. Zanna, S. Tervakangas, J. Kolehmainen, and P. Marcus, "Chromium and tantalum oxide nanocoatings prepared by filtered cathodic arc deposition for corrosion protection of carbon steel", *Surface and Coatings Technology,* vol. 206, pp. 3903-3910, 2012.

[5]   J.-Y. Zhang and I. W. Boyd, "Thin tantalum and tantalum oxide films grown by pulsed laser deposition", *Applied surface science,* vol. 168, pp. 234-238, 2000.

[6]   O. Kerrec, D. Devilliers, H. Groult, and P. Marcus, "Study of dry and electrogenerated Ta 2 O 5 and Ta/Ta 2 O 5/Pt structures by XPS", *Materials Science and Engineering: B,* vol. 55, pp. 134-142, 1998.

[7]   E. Atanassova and D. Spassov, "X-ray photoelectron spectroscopy of thermal thin Ta 2 O 5 films on Si", *Applied surface science,* vol. 135, pp. 71-82, 1998.

[8]   E. Atanassova, G. Tyuliev, A. Paskaleva, D. Spassov, and K. Kostov, "XPS study of N 2 annealing effect on thermal Ta 2 O 5 layers on Si", *Applied surface science,* vol. 225, pp. 86-99, 2004.

[9]   T. Miyazaki, H.-M. Kim, T. Kokubo, C. Ohtsuki, H. Kato, and T. Nakamura, "Mechanism of bonelike apatite formation on bioactive tantalum metal in a simulated body fluid", *Biomaterials,* vol. 23, pp. 827-832, 2002.

Chapter 5

In-vitro bone-bonding ability of Ta$_{1-x}$O$_x$ coatings

The following chapter is partially based on the results published in:

- C. F. Almeida Alves, A. Cavaleiro and S. Carvalho; "*Bioactivity response of Ta$_{1-x}$O$_x$ coatings deposited by reactive magnetron sputtering*" Materials Science and Engineering C: Materials for Biological Applications, 58 (2016) 110-118.

5.1. Introduction

The present thesis proposes the development of a novel bioactive and osseointegrated surface based on the effect of a nanostructured and/or oxide surface of Ta-based materials. The previous chapters provided a further insight of the processing parameters influence on the surfaces optimization. Thereafter, the bioactivity of $Ta_{1-x}O_x$ surfaces developed by MS is performed in order to confirm that TaO_x surfaces are in fact bioactive and can regulate the bone-bonding ability.

According to the biocorrosion validation of the $Ta_{1-x}O_x$ coatings, the assessment of coatings surface properties is performed in two samples, Ta1 and TO6 (5 and 70 at.% oxygen, respectively), which presented the chemical composition threshold, as well as, TO6 presented the best corrosion performance. CP Ti Gr2 is used as commercial control of dental implants. The selected samples are summarized in Figure 5.1.

Commercial control
• CP Ti Gr2

Metallic-like surface
• Ta1

Oxide surface
• TO6
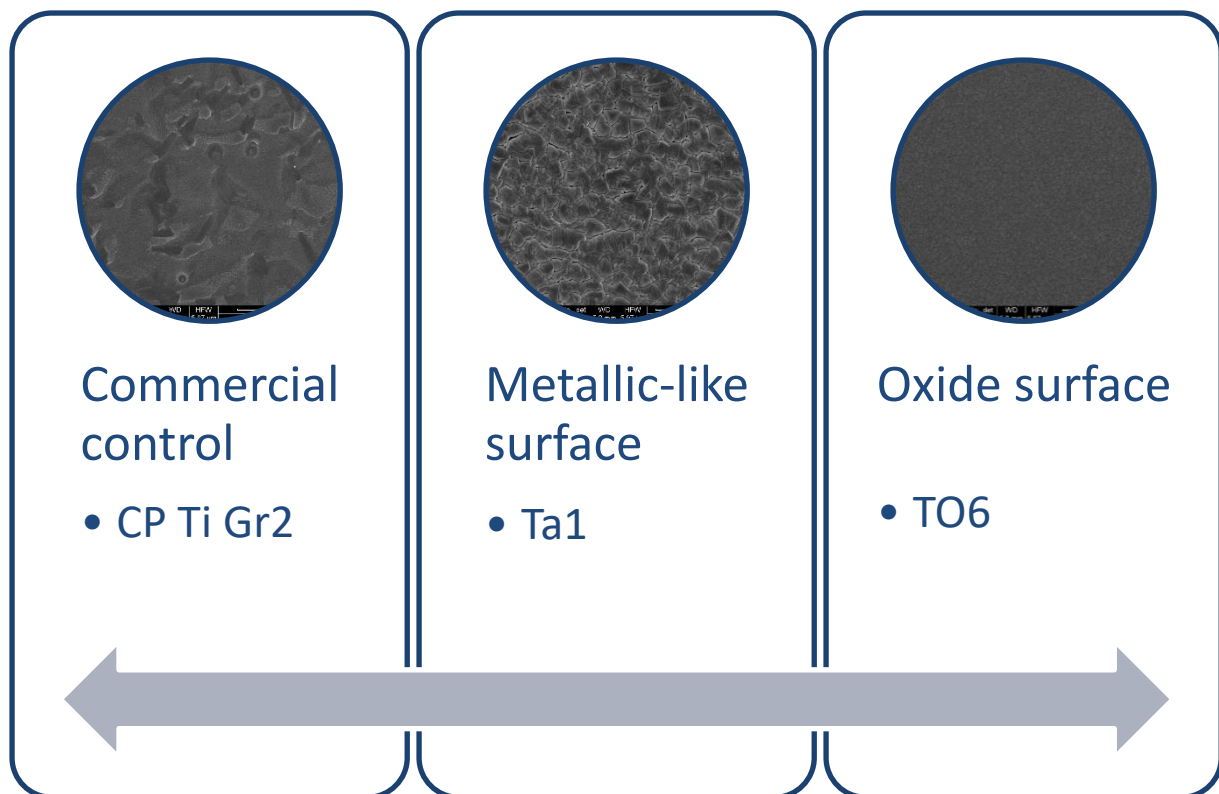
Figure 5.1: Selected samples to perform *in-vitro* bone-bonding ability studies.

Therefrom, bioactivity test allows the identification of a good candidate for bioactive surface. According to the ISO 23317, from sample immersion in Simulated Body Fluid (SBF) (Annex III), since it has an ionic concentration nearly equal to those of human blood plasma, it is possible to predict the *in-vitro* bone-bonding ability of a certain material. This method is tested in several types of materials in order to validate the methodology in terms of prediction the *in-vitro* bone bioactivity by examination of the apatite formation, either qualitatively or quantitatively. This method can also be used for screening the bone bioactivity of the materials before animal testing [1].

5.1. Materials and methods

5.1.1. Sessile drop test

Materials' surface properties are important parameters that should be taking into account for tissue engineering applications. Wettability is an important surface property when developing biomaterials once it can regulate the protein adsorption and, consequently, the cell behavior [2].

In this work, the evaluation of the surface wettability behavior follows the Van Oss approach [3], characterizing the samples' surface as a hydrophilic or hydrophobic. Van Oss considers that a surface with contact angle above 65° is considered hydrophobic, while for values lower than 65° the surface is called hydrophilic. Another important parameter to understand adhesion phenomenon of surfaces is the surface free energy determination. The calculation of the surface free energy is based on the Young's equation [3], which describes the thermodynamic equilibrium of the three interfacial tensions that coexist in the boundary of a liquid droplet in a solid surface. The Young's relation is described by the Equation 5.1

Equation 5.1

$$\gamma_{SV} - \gamma_{SL} = \gamma_{LV} \cos\theta$$

where γ_{SV} is the tension between the solid and vapor phases, γ_{SL} is the tension between the solid and the liquid phases, γ_{LV} is the tension between the liquid and vapor phases and θ is the contact angle.

The calculation of the surface free energy (ΔG) allows to quantitatively classify the hydrophilic/hydrophobic character of a surface. The surface free energy is the work necessary to expand the drop of liquid on a unit area. In this case, when the surface free energy appears negative, the interaction between the molecules of the liquid and the surface of the sample is repulsive and, thus, the surface poorly interacts with the water, making the surface hydrophobic. Contrary, when the surface free energy becomes positive (≥ 0), the interaction is repulsive and, consequently, the surface is hydrophilic due to the higher interaction between the sample surface and the water. Therefore, zero surface free energy is the limit between hydrophilic and hydrophobic surfaces [3].

The surface wettability features of the developed surfaces were assessed by measuring the static contact angle at room temperature in a DataPhysics OCA-15 equipment. It was used a 2 µL drop volume of ultra-pure water, α-bromonaphtalene and formamide as tested liquids. For each sample, a minimum of eight measurements were recorded, and aftermost the average value was calculated.

5.1.2. In-vitro bone-bonding ability

The bioactivity was evaluated by soaking the coating in 40 mL of SBF at 36.5 °C. SBF was prepared by diluting NaCl, NaHCO$_3$, KCl, K$_2$HPO$_4$.3H$_2$O, MgCl$_2$.6H$_2$O, CaCl$_2$, and Na$_2$SO$_4$ into milli-q water and buffered at pH 7.40 at 36.5 °C with 45 mM of (CH$_2$OH)3CNH$_2$ and with an appropriate amount of HCl using the Kokubo and Takadama approach [1]. After being soaked, the samples were removed from the SBF solution, respectively after 24 hours, 7 and 14 days, they were cleaned with milli-q water and dried in a desiccator. For each sample, three measurements were performed to statistically validate the results. SEM characterization operating at 5 keV in secondary electron mode and in EDS analysis performed at 10 keV were used to study and evaluate both the presence of calcium phosphates and the evolution of Ca/P ratio on the surface of the soaked samples. XRD

patterns were also recorded in Bragg-Brentano geometry (step size of 0.02° and time per step of 1 s) to detect vestiges of crystalline calcium phosphates and their respective phase composition.

5.2. Surface roughness and surface free energy

The roughness values obtained from AFM analysis of $Ta_{1-x}O_x$ coatings deposited on SS 316L substrates and CT Ti Gr2 (used in commercial dental implants) are shown in Table 5.1. The addition of oxygen on the coatings promotes a significant decrease of the mean roughness (Ra) values, which is in good agreement with SEM observations where the increase of oxygen content leaded to a denser morphology. Generally, the root mean square average (Rq) values are in good agreement with the mean roughness values demonstrating the good homogeneity of the samples.

Table 5.1: Ra, Rq and Rmax values of CP Ti Gr2 and SS 316L bulk materials, as well as, Ta1 and TO6 coatings deposited on SS 316L, measured by AFM and resulting from an average of three different zones.

Sample	CP Ti Gr2	SS 316L	Ta1	TO6
Ra (nm)	71 ± 39	2.5 ± 0.11	21 ± 2.2	5.8 ± 0.40
Rq (nm)	88 ± 49	3.4 ± 0.25	26 ± 2.6	8.2 ± 0.53
Rmax (nm)	503 ± 250	44 ± 3.1	201 ± 6.3	103 ± 17

The measured contact angle values and the surface free energy of the samples are presented in Table 5.2.

Table 5.2: Milli-q water (θ_w), formamide (θ_F) and α-bromonaphtalene ($\theta_{\alpha\text{-B}}$) contact angles, surface energy components (apolar Lifshitz–Van der Waals surface free energy component, γ_{LW}; electron acceptor surface free energy component, γ^+; and electron donor surface free energy component, γ^-) and surface free energy of CP Ti Gr2, SS 316L, the Ta1 and TO6 coatings, deposited onto SS 316L.

Sample	Contact angle ± SD* (°)			Surface energy components (mJ/m²)			ΔG_{mwm} (mJ/m²)
	ϑ_w	ϑ_F	$\vartheta_{\alpha\text{-B}}$	γ^{LW}	γ^+	γ^-	
CP Ti Gr2	74 ± 2.8	48 ± 3.1	25 ± 1.4	40	0.46	7.3	-46
Ta1	100 ± 4.8	67 ± 3.9	36 ± 1.5	36	0.20	0	-97
TO6	63 ± 2.8	38 ± 3.5	21 ± 0.98	41	0.89	13	-31

*Standard Deviation

In view of milli-q water, Ta1 surface has a much higher contact angle (around 100°) than the control CP Ti Gr2 (approximately 74°) being assumed as the sample with the most hydrophobic character. With the increase of oxygen content in the coating a decrease of the contact angle values down to 63° is observed.

Regarding the surface free energy values, similar trends are observed, Ta1 coating shows the lowest surface free energy (-97 mJ/m²), less than the CP Ti Gr2 control. Oxygen-containing coating exhibit a surface free energy increase up to -31 mJ/m². All analyzed samples show a typical hydrophobic behavior (with a surface energy value below zero). TO6 (oxygen containing sample) surface has the highest value of surface free energy, thus, indicating a lower degree of hydrophobicity, which is in accordance with its contact angle value slightly below 65° (63°). These results suggest that TO6 sample has some polar interaction with the liquids.

From literature [4], based on the surface chemistry, for Ta1 sample a lower contact angle in relation to control surface, CP Ti Gr2, is expected (31° and 54° respectively). Such trend is not observed in this study. This discordant result can be explained by the significant difference in the roughness values of the tested samples. In fact, the commercial control sample has a much higher Ra value than Ta sample, factor which is known to have a great influence on the contact angle [5-7].

The literature reports [3], that the influence nanoroughness on the wettability is not clear. So, these results suggest that the surface chemistry (addition of oxygen) is predominant on the regulation of the wettability.

Both polar surface energy components (γ^+ and γ^-) of Ta1 sample are close to zero, which indicates that the surface is predominantly apolar. On the other hand, with the increase of oxygen content the negative polar surface energy component (γ^-) increase significantly, indicating that the surface become monopolar. Ta1 sample shows qualitatively a hydrophobic behavior in agreement with its low surface free energy, while TO6 coating shows a contact angle value slightly below of 65°. This value is indicative of polar surface interaction typical to moderately hydrophilic surfaces. A better cell adhesion to hard tissue (bone) is expected for this sample since, for moderately hydrophilic and negatively charged surfaces the adsorption of cells is enhanced [8-10]. L. Bacakova e*t al.* [10], showed that a contact angle close to 63° is an optimum value for osseointegration.

5.3. Bioactivity response

Figure 5.2 shows SEM micrographs of the surfaces of the three studied samples before and after immersion in SBF for 14 days. Note that the results for samples before soaking in SBF are, hereafter, denoted as 0h. The SEM micrographs show different morphologies of the calcium phosphates formed on the surfaces after 14 days of immersion in SBF.
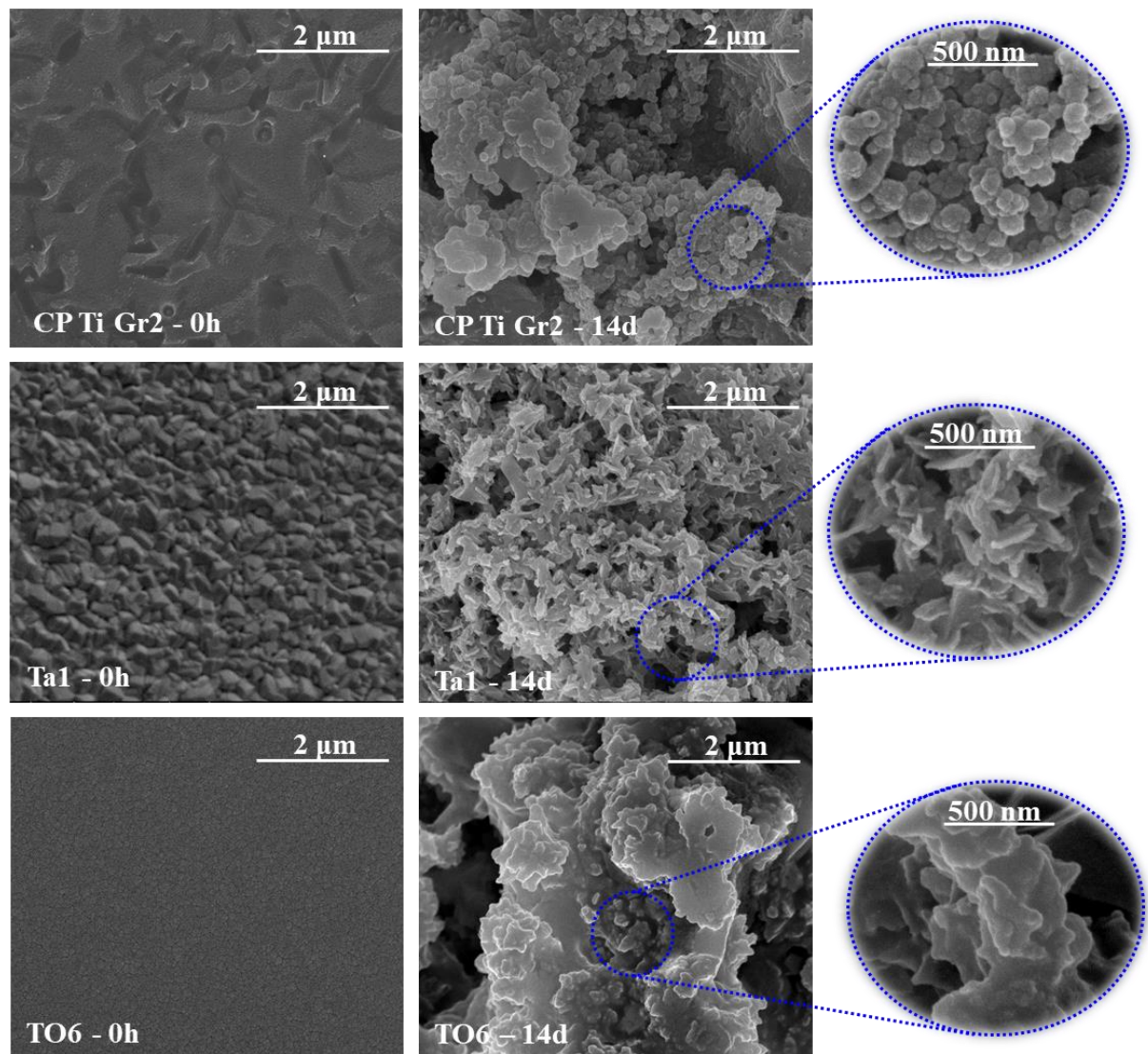
Figure 5.2: TOP view SEM micrographs of studied samples, CP Ti Gr2, Ta1 and TO6, respectively, before and after14 days of immersion in SBF at 37 °C.

The presence of Ca and P was verified by EDS technique then, the mean ratio Ca/P was determined by the average of three EDS measurements in different zones of the sample and is shown in Figure 5.3. It should be pointed out that before 7 days, no calcium phosphates were detected in any of the analyzed surfaces. After 7 days only for the CP Ti Gr2 sample signs of calcium phosphates is not observed. After 14 days of exposure the Ca/P atomic ratio on the surface of the coating with 70 at.% oxygen, TO6, is 1.73 approaching the ratio of natural hydroxyapatite (1.67 according to the literature [11]). Calcium phosphates are also observed on the Ta1 surface, with a ratio Ca/P also close to the natural hydroxyapatite (1.57). The CP Ti Gr2 control shows the worst bioactive

behavior since, by EDS, the calcium phosphates visible in the surface show a Ca/P ratio very far from the natural hydroxyapatite, specifically 0.95. This fact proves that the bioactivity kinetics of $Ta_{1-x}O_x$ surfaces is faster than that of Ti surface favoring a faster osseointegration.
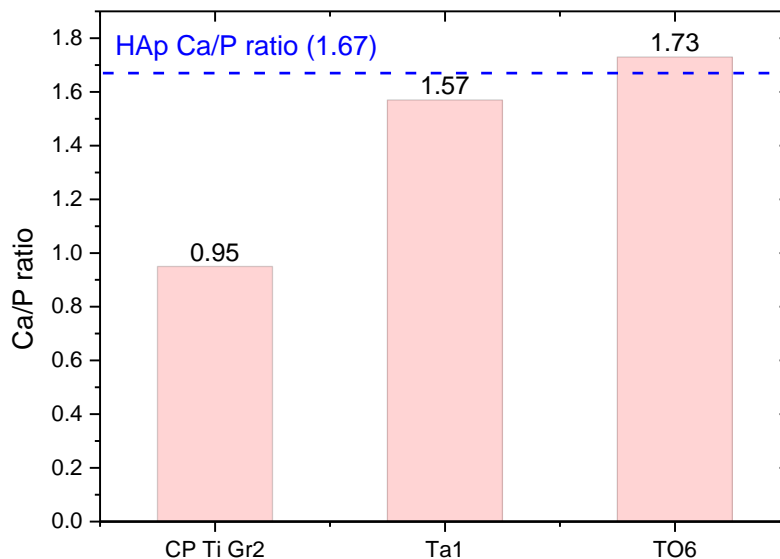
Figure 5.3: Ca/P ratio of the tested samples after *in-vitro* bone-bonding ability tests obtained by EDS analysis.

In the oxide sample the adhesion of ions of the fluid, namely Ca^{2+}, to the surface of the sample is significantly superior, what is expected since this sample showed a surface free energy close to zero and a lower contact angle around 63º, reported as optimum conditions for osseointegration [10]. According to Kokubo *et al.* [12, 13], oxide surfaces are the best option for the interaction with the fluid. From literature [14], when a Ta oxide (such as TO6) surface is soaked in SBF, by ion exchange, hydration of Ta-O occurs and Ta-OH groups are formed, providing favorable sites for the calcium phosphates nucleation. The Ta-OH groups bind to Ca^{2+} ions forming a calcium tantalate, which, then, binds to PO_4^{3-} ions to form apatite. The bone progenitor cells interact with the oxide phase through this diffusion layer; the chemical bonding established between the functional groups (Ta-OH) and the calcium phosphate ions promotes a stronger bond between the dental implant surface and the cells. As verified, the Ta-OH groups induce a faster apatite

nucleation by increasing the ionic activity at the surface. Therefore the oxidation state of the surface is benefic for the exponentiation of osseointegration [14]. Ta1 sample also demonstrates a high ability to bind with calcium phosphate ions even though only a residual content of oxygen exists. The high passivation rate of Ta and the oxide layer formed on the top [15] have a fundamental role for the formation of Ta-OH groups when the sample is soaked in SBF. For the control surface, CP Ti Gr2, although Ti also has a high passivation rate [16], it does not so easily promote apatite formation. The surface chemistry of Ta-based and Ti-based surfaces is different, which, as reported by Frandsen *et al.* [4], causes a significant difference in the adhesion of the calcium phosphate.

After 14 days of immersion, the changes in the morphology of the calcium phosphates of the soaked samples is mainly dictated by the Ca/P ratio. The morphology of the calcium phosphate in the control surface is a typical cauliflower-like apatite cluster [17] whereas, in the $Ta_{1-x}O_x$ surfaces the morphology of the calcium phosphates evolve to a needle shaped-like layered apatite [18, 19]. These needles are composed by a lot of densely packed lamellas of crystalline apatite [20]. This morphology is very promising since it is similar to that of the apatite which constitutes the bone [19].

Concerning the Ca/P atomic ratio estimated by EDS, it is possible to observe that there is a difference between the values of Ta1 and TO6 samples. These differences can be explained by the presence of carbon in the calcium phosphates, as detected by EDS measurements. As it is known, apatite is a flexible mineral that needs several elements to grow, such as, Ca, P, O and the appropriated channel-filling ions (OH^-, Cl^-, F^-, CO_3^{2-}) [21]. Subsequently, these ions allow several chemical substitutions determining the apatite structure. Usually the bone is an OH^- containing apatite with a very specific structure and composition [11]. According to the literature [20], the biomimetic way to induce the apatite growth as proposed by Kokubo and Takadama [1], also used in this study, leads to a carbonate containing bone-like apatite [20]. The carbonate substitution in the apatite structure can occur through two different ways: in the OH^- site as "A-type" substitution; or in the PO_4^- site as "B-type" substitution. Hence, it is suggested that in the present study the differences of the Ca/P atomic ratio values are related to the type of C substitution, in Ta1 surface should be of A-type whereas for TO6 of B-type [11].

Wherefore, XRD studies were performed to detect vestiges of crystalline calcium phosphates and their respective phase composition. Figure 5.4 shows the XRD results of the immersed samples in SBF after 14 days. Ta1 and TO6 samples show the presence of a crystalline phase based on calcium phosphates as suggested by EDS results. This apatite is strongly oriented, not being detected any other XRD peak in the diffractogram, which does not allow to precisely identify which apatite structure is being formed. The crystallinity degree is significantly higher in Ta1 than for TO6 surface. On the other hand, CP Ti Gr2 only shows peaks corresponding to the hexagonal Ti phase (ICDD card nº 00-044-1294) suggesting that the formed calcium phosphates in its surface is in low amount.

After 14 days of immersion in SBF

----- $Ca_{10}(PO_4)_6CO_3$: monoclinic (ICDD card nº 00-035-0180) **or**

$Ca_4H_8Ca_2O_{12}P_4.10H_2O$: monoclinic (ICDD card nº 00-025-1996)

······ Ti: hexagonal (ICDD card nº 00-044-1294)
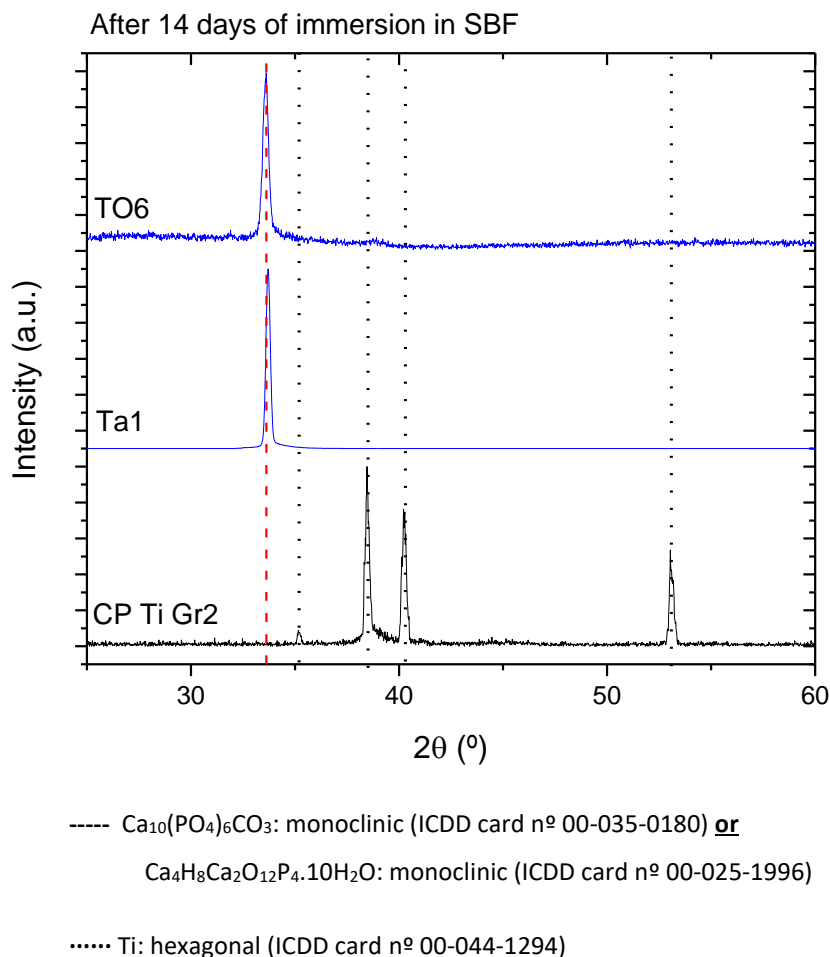
Figure 5.4: Bragg-Brentano XRD patterns of CP Ti Gr2, Ta1 and TO6 surfaces, respectively, after 14 days of immersion in SBF at 37 °C.

The XRD results are not conclusive since only one peak, around 33.86°, is detected in the pattern for Ta1 and TO6. However, considering the chemical composition estimated by EDS, showing the presence of carbon on the calcium phosphates, this peak can be assigned to either a monoclinic calcium phosphate carbonate (ICDD card nº 00-035-0180) or a monoclinic calcium tetraphosphonate decahydrate (ICDD card nº 00-025-1996). The lower crystallinity degree of TO6 sample can be related with the above type of carbonate substitution in the apatite structure. In fact, in the B-type substitution suggested for the Ta oxide sample, the amorphous carbonate is incorporated into the apatite structure in the PO_4^- site, which can lead to a decrease of the apatite crystallinity. The XRD pattern of the commercial control surface, CP Ti Gr2, exhibiting its hexagonal structure suggest that the presence of calcium phosphates in the surface is very low and, therefore, undetectable by XRD.

5.4. Partial conclusions

Regarding the surfaces developed by MS, the contact angle measurements reveal that Ta1 coating presents the most hydrophobic character (100°). Besides, the increase of oxygen content causes the decrease on the contact angle values with TO6 coating depicting the lowest value, about 63°. Bioactivity tests show the presence of calcium phosphates after 7 days of immersion in SBF, only for $Ta_{1-x}O_x$ samples. This behavior is confirmed after 14 days of exposure since Ca/P ratio values of 1.57 and 1.73 were measured for Ta1 and TO6 coatings, respectively, and are close to the hydroxyapatite value (Ca/P ≈1.67). The commercial surface control CP Ti Gr2 shows a much lower Ca/P ratio of 0.95, meaning that the osseointegration is not well enhanced as for the promising $Ta_{1-x}O_x$ surfaces.

5.5. References

[1]   T. Kokubo and H. Takadama, "How useful is SBF in predicting in vivo bone bioactivity?", *Biomaterials,* vol. 27, pp. 2907-2915, 2006.
[2]   K. Cai, M. Frant, J. Bossert, G. Hildebrand, K. Liefeith, and K. D. Jandt, "Surface functionalized titanium thin films: zeta-potential, protein adsorption and cell proliferation", *Colloids and Surfaces B: Biointerfaces,* vol. 50, pp. 1-8, 2006.

[3]   C. Van Oss, R. Good, and M. Chaudhury, "The role of van der Waals forces and hydrogen bonds in "hydrophobic interactions" between biopolymers and low energy surfaces", *Journal of colloid and Interface Science,* vol. 111, pp. 378-390, 1986.

[4]   C. J. Frandsen, K. S. Brammer, K. Noh, G. Johnston, and S. Jin, "Tantalum coating on TiO2 nanotubes induces superior rate of matrix mineralization and osteofunctionality in human osteoblasts", *Materials Science and Engineering: C,* vol. 37, pp. 332-341, 2014.

[5]   T. Albrektsson and A. Wennerberg, "Oral implant surfaces: Part 1--review focusing on topographic and chemical properties of different surfaces and in vivo responses to them", *The International Journal of Prosthodontics,* vol. 17, pp. 536-543, 2004.

[6]   G. Mendonça, D. B. S. Mendonça, F. J. L. Aragão, and L. F. Cooper, "Advancing dental implant surface technology – From micron- to nanotopography", *Biomaterials,* vol. 29, pp. 3822-3835, 2008.

[7]   L. Zhang and T. J. Webster, "Nanotechnology and nanomaterials: promises for improved tissue regeneration", *Nano Today,* vol. 4, pp. 66-80, 2009.

[8]   T. Kokubo, "Formation of biologically active bone-like apatite on metals and polymers by a biomimetic process", *Thermochimica Acta,* vol. 280, pp. 479-490, 1996.

[9]   J. Wei, T. Igarashi, N. Okumori, T. Igarashi, T. Maetani, B. Liu, and M. Yoshinari, "Influence of surface wettability on competitive protein adsorption and initial attachment of osteoblasts", *Biomedical Materials,* vol. 4, pp. 045002-7, 2009.

[10]   L. Bacakova, E. Filova, M. Parizek, T. Ruml, and V. Svorcik, "Modulation of cell adhesion, proliferation and differentiation on materials designed for body implants", *Biotechnology Advances,* vol. 29, pp. 739-767, 2011.

[11]   B. Wopenka and J. D. Pasteris, "A mineralogical perspective on the apatite in bone", *Materials Science and Engineering: C,* vol. 25, pp. 131-143, 2005.

[12]   T. Kokubo, F. Miyaji, H. M. Kim, and T. Nakamura, "Spontaneous formation of bonelike apatite layer on chemically treated titanium metals", *Journal of the American Ceramic Society,* vol. 79, pp. 1127-1129, 1996.

[13]   T. Kokubo, T. Matsushita, H. Takadama, and T. Kizuki, "Development of bioactive materials based on surface chemistry", *Journal of the European Ceramic Society,* vol. 29, pp. 1267-1274, 2009.

[14]   T. Miyazaki, H.-M. Kim, T. Kokubo, C. Ohtsuki, H. Kato, and T. Nakamura, "Mechanism of bonelike apatite formation on bioactive tantalum metal in a simulated body fluid", *Biomaterials,* vol. 23, pp. 827-832, 2002.

[15]   C. P. Sharma and W. Paul, "Protein interaction with tantalum: changes with oxide layer and hydroxyapatite at the interface", *Journal of Biomedical Materials Research,* vol. 26, pp. 1179-1184, 1992.

[16]   B. Feng, J. Weng, B. Yang, S. Qu, and X. Zhang, "Characterization of surface oxide films on titanium and adhesion of osteoblast", *Biomaterials,* vol. 24, pp. 4663-4670, 2003.

[17]   J. Shi, N. M. Alves, and J. F. Mano, "Thermally responsive biomineralization on biodegradable substrates", *Advanced Functional Materials,* vol. 17, pp. 3312-3318, 2007.

[18]   R. Murugan and S. Ramakrishna, "Bioresorbable composite bone paste using polysaccharide based nano hydroxyapatite", *Biomaterials,* vol. 25, pp. 3829-3835, 2004.

[19]   E. Nejati, V. Firouzdor, M. Eslaminejad, and F. Bagheri, "Needle-like nano hydroxyapatite/poly (l-lactide acid) composite scaffold for bone tissue engineering application", *Materials Science and Engineering: C,* vol. 29, pp. 942-949, 2009.

[20]   H. Li, W. Huang, Y. Zhang, and M. Zhong, "Biomimetic synthesis of enamel-like hydroxyapatite on self-assembled monolayers", *Materials Science and Engineering: C,* vol. 27, pp. 756-761, 2007.

[21]   L. Calderin, M. Stott, and A. Rubio, "Electronic and crystallographic structure of apatites", *Physical Review B,* vol. 67, pp. 134106-7, 2003.

Chapter 6

Tantalum oxides produced by anodization process

6.1. Introduction

Nanostructured surfaces are able to biomimetize bone tissue and hence, enhance surface-protein interaction, bioactivity and osteoblast adhesion that plays a fundamental role in bone ingrowth. Anodization method allows both formation of bioactive and nanostructured TaO_x surface, which could further enhance the interaction between the implant surface and the cells from adjacent tissues.

On this regard, this chapter provides an extensive study of the anodization conditions effect (electrolyte concentration, potential and time) on the size, shape and distribution of the nanostructures over the anodic layer formed on Ta-based materials surface. Moreover, it is intended to demonstrate how the anodization conditions may alter the nanostructures formation mechanism between nanopore and nanotube assemblies.

Additionally, due to the importance of surface properties on the osseointegration once it can regulate the interactions between the surface and the cells, some insights about the influence of the nanostructures on the roughness and wetting properties is given.

6.2. Materials and methods

6.2.1. Sample preparation

Anodic TaO_x nanostructures were produced by high-purity Ta sheet (99.95% with 0.5 mm thick) (Annex IV) anodization. The Ta sheet was previously degreased and cleaned using ultrasonic bath during 5 min in benzene and then ethanol. Subsequently, the samples were rinsed with distilled water and dried in air.

ACS H_2SO_4 (95-98%vol), HF (48%vol) and HNO_3 (69-71%vol) grade reagents were used to prepare the electrolytes.

Prior to the electrochemical anodization, an acid etching with a 1:1 volumetric mixture of HNO_3 with HF acids was performed to make the surface smoother and hence, enhance the anodic morphology homogeneity.

Electrochemical anodization occurred in potentiostatic mode with resource to an Agilent N5751A DC Power supply and Agilent 34450A 5 1/2 Digit Multimeter coupled with a computer for data logging. The anodization was performed in a two-electrode cell configuration, comprising the working electrode (Ta sheet) and reference electrode (carbon stick). The distance between the electrodes was kept constant at 30 mm, as well as, the electrolyte was magnetically stirred during the anodization to promote its homogeneity in terms of composition and temperature. Ta specimens ($20 \times 20 \times 0.5$ mm^3) were anodized in concentrated mixture of 7 - 9 volumetric percentage (vol.%) of H_2SO_4 with 0.125-1 vol.% of HF filled under potentials between 15 - 50 V during a time range of 5 - 120 s at room temperature. Immediately after anodic treatment, the samples were rinsed with multiples distillated water immersions and then, dried in air. Table 6.1 summarizes the anodization conditions used in this work.

6.2.2. Sessile drop test

The surface wettability features of the developed surfaces were assessed by measuring the static contact angle at room temperature in a DataPhysics OCA-15 equipment. It was used a 2 µL drop volume of ultra-pure water, α-bromonaphtalene and glycerol (instead of formamide) as tested liquids. For each sample, a minimum of eight measurements were recorded and aftermost the average value was calculated.

Table 6.1: Processing parameters such as electrolyte concentration, potential and time used in the samples anodization.

Sample	[H$_2$SO$_4$] (M)	Vol.% H$_2$SO$_4$	[HF] (M)	Vol.% HF	Potential (V)	Time (s)
1	14.6	8	**2.9**	**1**		
2	**14.6**	**8**	**1.45**	**0.5**	15	120
3	14.6	8	**0.73**	**0.25**		
4	14.6	8	**0.37**	**0.125**		
5	**16.4**	**9**	1.45	0.5	15	120
6	**12.8**	**7**	1.45	0.5		
7					**20**	
8					**25**	
9					**30**	
10	14.6	8	0.73	0.25	**35**	120
11					**40**	
12					**45**	
13					**50**	
14						**5**
15	14.6	8	0.73	0.25	25	**15**
16						**30**
17						**60**

6.1.   Influence of anodization parameters on the surface morphology

6.1.1. Dissolution capability affected by electrolyte concentration

Electrochemical anodization by dissolution assisted by electric field mechanism is used in this work demonstrating the formation of highly ordered nanoarrays on Ta surfaces. Figure 6.1 shows the SEM images of Ta anodized surfaces using different concentrated mixtures of H_2SO_4 with HF, at room temperature under 15 V during 120 s.
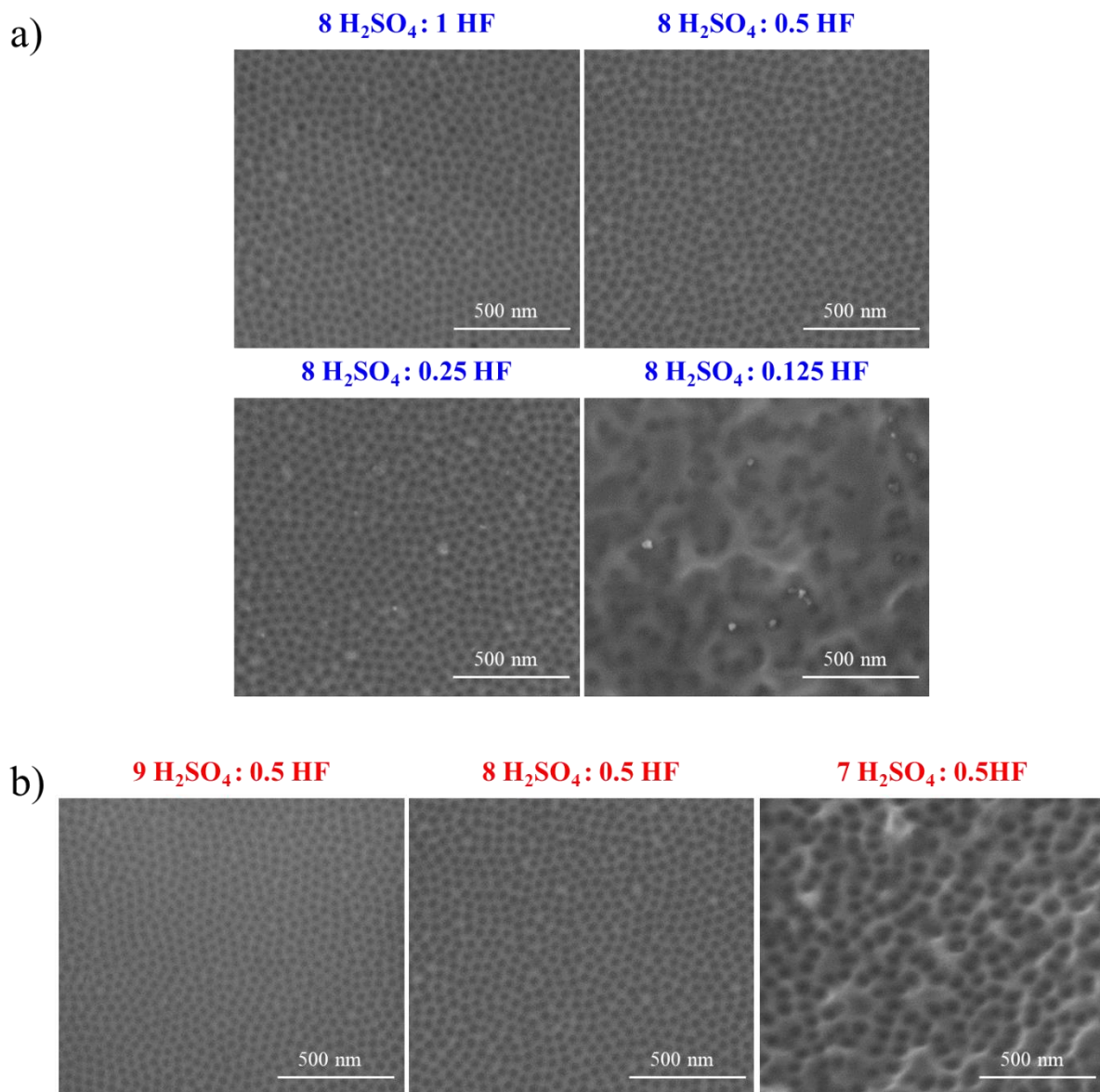
Figure 6.1: TOP view SEM images of Ta anodized surfaces using different concentrated mixtures of H_2SO_4 with HF: (a) 1-0.125 vol.% of HF; and (b) 9-7 vol.% of H_2SO_4; at room temperature under 15 V during 120 s.

The nanostructures growth results from a competition between the continuous formation and dissolution of the anodic TaO_x. Despite of the formation of highly ordered nanostructures, in agreement with what is reported in the literature [1], a dependence of the nanostructures formation of HF concentration is observed. Decreasing the HF concentration in the anodic electrolyte from 1 to 0.25 volumetric percentage (vol.%) (Figure 6.1.a), while keeping constant the H_2SO_4 concentration (8 vol.%), the nanostructures formation remains well-ordered. However, with further decrease on the HF concentration down to 0.125 HF vol.% (Figure 6.1.a) a dissolution limit-like of the anodic TaO_x is reached having a dramatic effect on the nanostructures growth, mainly on the arrays order quality. In this process, F^- ions are responsible to attack the anodic oxide and then, dissolve it by pitting. A decrease in F^- concentration simultaneously with a water content increase stabilizes the anodic oxide, decreasing the dissolution rate. Moreover, the low HF concentration compromises not only the order quality, as well as, induces a differential dissolution capacity and some areas over the surface only exhibit the formation of a compact anodic oxide. Nevertheless, in spite of the HF capacity to dissolve and create anodic oxide nanostructures, there is also a clear dependence of the H_2SO_4 concentration to achieve highly ordered nanostructures (Figure 6.1.b). Similarly, decreasing the H_2SO_4 concentration in the anodic electrolyte from 9 to 7 vol.% (Figure 6.1.b), while keeping the constant HF concentration (0.5 HF vol.%), for 7 H_2SO_4 vol.% it is also reached a dissolution limit-like of the anodic layer. According to the literature [2, 3], concentrated sulfuric acid electrolytes induce anions (SO_4^{2-}) incorporation into the anodic oxide being responsible for enhance the HF capacity to dissolve the anodic layer due to an ions exchange mechanism, which explain this dependency.

On the other hand, although the volumetric concentrations change the nanostructures morphology is not varying. Apparently, the surfaces anodized with the lowest HF or H_2SO_4 concentrations (dissolution limit-like) (Figure 6.1) seems to be different from the other ones. However, the apparently different morphology is only a electropolishing effect. During anodization and depending of the conditions, simultaneously to the formation and dissolution of anodic oxide occurs a polishing and smoothing of the surface, erasing the rough base material topography. As the dissolution rate for these two conditions is lower, the surface polishing drop down revealing a rougher surface. Yet, the existent

nanostructures over the Ta surface remains similar. Therefrom, EDS mapping by STEM analysis was performed to further clarify the shape morphology and composition of the nanostructures. Figure 6.2 shows a representative HAADF STEM - EDS map of the sample anodized with 8:0.5 (vol:vol) of H_2SO_4 mixed with HF, respectively, at room temperature under 15V during 120 s.
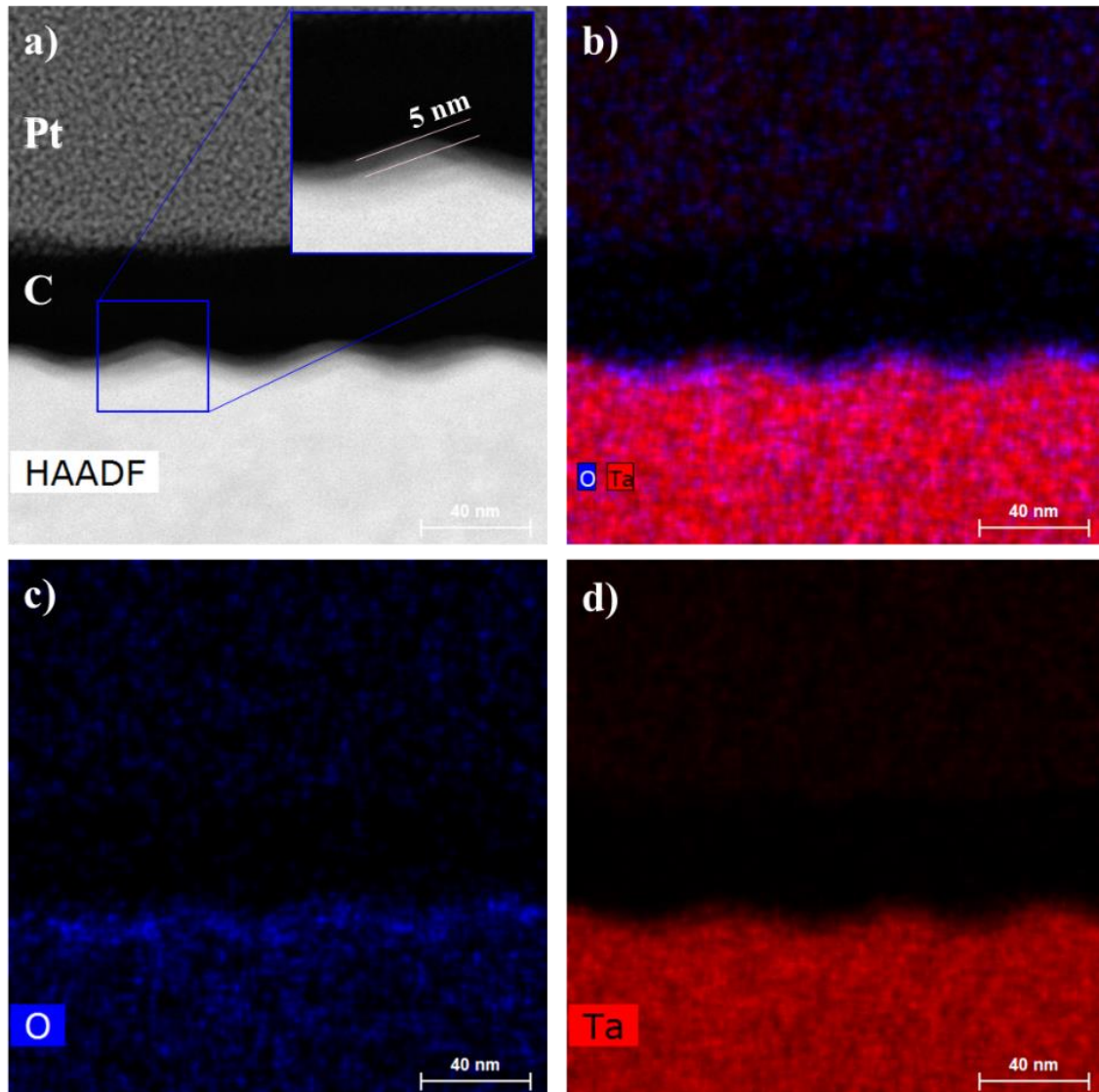
Figure 6.2: Cross-section HAADF STEM and EDS spectrum images showing the elemental distribution for the anodic layer of a Ta sample anodized with 8:0.5 (vol:vol) of H_2SO_4 : HF, respectively, at room temperature under 15 V during 120 s.

The HAADF STEM – EDS map shows a well-ordered array of dispersed dimples rather than a porous oxide. The preferential radial spread promoted by field-enhanced dissolution on the small surface asperities induces a dimpled topography inherent to the metal surface, exhibiting a thickness around 5 nm, as represented in Figure 6.2.a. The dimples start to grow at random pits and continue horizontally on the surface until reach the biggest diameter possible, as well as, grow into the bulk tantalum. According with Hany El-Sayed *et al*. [3], dimples tend to interact between each other, thus reaching a diameter steady equilibrium state.

6.1.2. Nanostructures diameter evolution controlled by anodization potential

The anodization potential is another electrochemical parameter that systematically affects the overall morphology of the nanostructures, since controls the electrons number/flow in the material during anodization [4]. Also, the efficiency of the other parameters such as electrolyte concentration, is affected by the potential as an integral parameter. Beyond that, the electric field distribution, which depends of the anodization potential, along the pits or asperities on the surface determines the diameter size of the nanostructures. On this sense, in order to study the influence of the anodization potential on the diameter of the dimples, Ta anodized surfaces with 8:0.25 (vol:vol) mixture of H_2SO_4 with HF, at room temperature during 120 s under a wide range of 15-50 V were prepared. The lower electrolyte concentration, before the dissolution limit-like, was selected in an attempt to have higher control on the process, as well as, a higher control of the morphology. In this analysis, image segmentation was carried out to determine the dimples average diameter and distribution over the Ta surface using Fiji ImageJ software. Then, a descriptive statistical analysis was performed. A set of processing conditions, including circularity, minimum and maximum (depending of the anodization potential applied) pore size, were selected to study the samples. It must be stressed that when was not possible to distinguish two or more different dimples due to the low image contrast/resolution the "dimples masks" was deleted, as shown in Figure 6.3, and not considered on the descriptive statistical analysis.
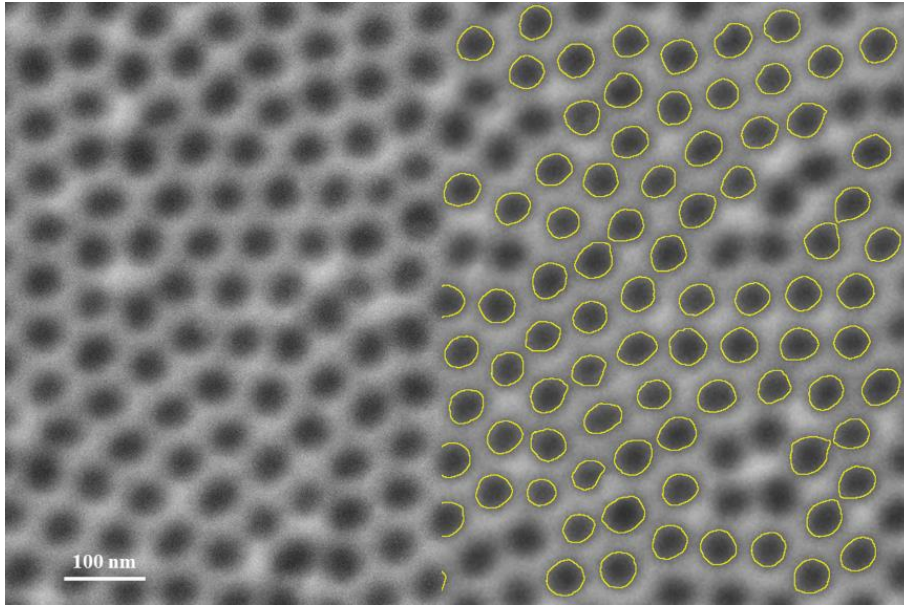
Figure 6.3: Representative TOP view SEM image and the image segmentation performed to a Ta sample anodized with 8:0.25 (vol:vol) of H_2SO_4 : HF, respectively, at room temperature under 20 V during 120 s.

The applied potential effect on the dimples diameter and distribution is shown in Figure 6.4. The number of dimples in the surface micrographs is clearly reduced when the anodization potential increases. Moreover, as potential increases a broader distribution is reached.

As reported in the literature [5], the anodized nanostructures diameter is linearly dependent of the anodization potential applied during the process. Indeed, Hany El-Sayed *et al.* [6] found that the diameter of Ta dimples empirically correlates with the applied potential according with Equation 6.1.

Equation 6.1

$$d = [1.5 \, nm \, V^{-1} \, \times \, V] + 15 \, nm$$

where *d* is the dimple diameter in nm and *V* is the applied potential vs. the counter electrode. Knowing that the anodic nanostructures grow starts from a pit or asperity in Ta surface, it is demonstrated that the nanostructures growth take place in all directions due to the hemispherical spread of the electric field and hence, the oxide structures acquires

a hemispherical shape [7]. As the pits or asperities on the surface are randomly distributed, increasing the applied potential a differential dissolution, promoted by the differences in the pits size, take place and thus, a larger dispersion and distribution of diameters arises. This demonstrates that anodization potential plays a significant role in controlling the dimple diameter.
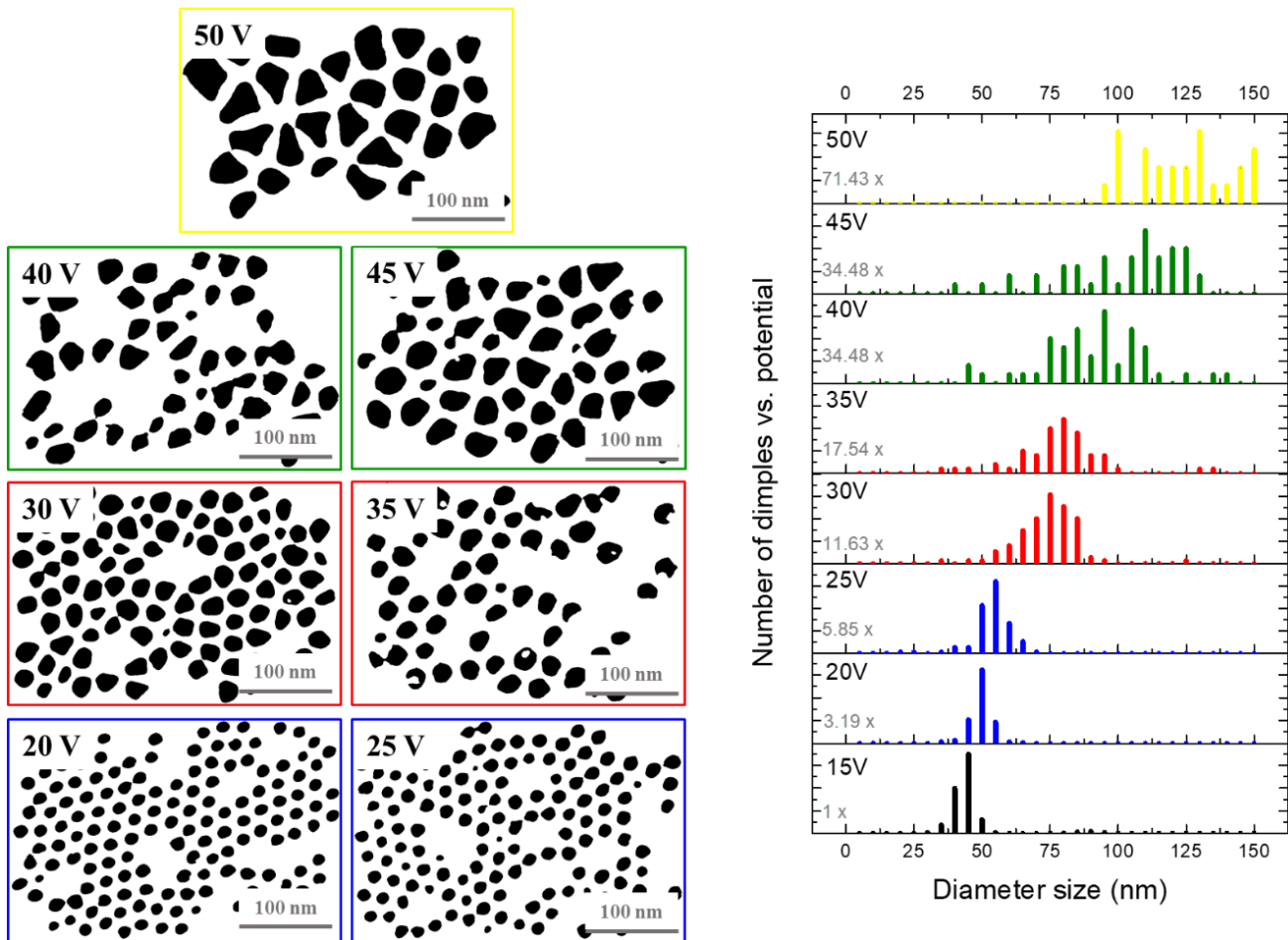
Figure 6.4: (a) Dimple masks obtained from the SEM images segmentation; (b) dimple diameter histogram as a function of the anodization potential (15-50 V) applied to the Ta anodized samples.

Apart from the statistical distribution, between 15 and 50 V the average diameter can be divided in four main behaviors. From 15 to 25 V the average dimple diameter is between 40 and 50 nm. Then, for the samples anodized with 30 and 35 V, an average diameter of 75 nm is reach. Furthermore, to 40 and 45 V the average diameter is about 100 nm, finally

reaching the maximum average diameter of 120 nm for 50 V. On its turn, the standard deviation of the average diameter increases as the anodization potential increase. Hence, as mentioned above, increasing the electrical field more differential dissolution take place as a consequence of the faster spread/dissolution in randomly modulations existents on the sample surface.

6.1.3. Cyclic mechanism of nanostructures formation: stability assessment

As reported in the state of the art [8, 9, 7, 5], with increase of anodization time F^- ions continuously react with the oxide layer being incorporated in the outer part of the anodic layer, forming a TaF_7^{2-} layer. Additionally, due to the higher migration velocity of the F^- ions, comparing with O^{2-} ions, the F^- ions may migrate from the outer part until walls of the anodic oxide layer. Considering that TaF_7^{2-} complexes are water soluble, its incorporation in the outer and inner part of the anodic layer is responsible for the separation of the pores forming nanotubes [7, 5]. Summarily, anodization is based on an electrical field application and depending on the anodization conditions, the process may lead to the formation of a nanoporous or nanotubular layer. Yet, these morphologies are difficult to stabilize during the anodization process due to the differentiated dissolution rate.

Figure 6.5 shows the morphology evolution with the anodization time of Ta anodizes surfaces using 8:0.25 (vol:vol) of H_2SO_4 mixed with HF, respectively, at room temperature under 25 V from 5 s to 60 s. The combination of a higher potential (compared with the initial ones – 15 V) with one of the lowest electrolyte concentration was selected in order to obtain a uniform distribution of the nanostructures over the surface at low dissolution rate.
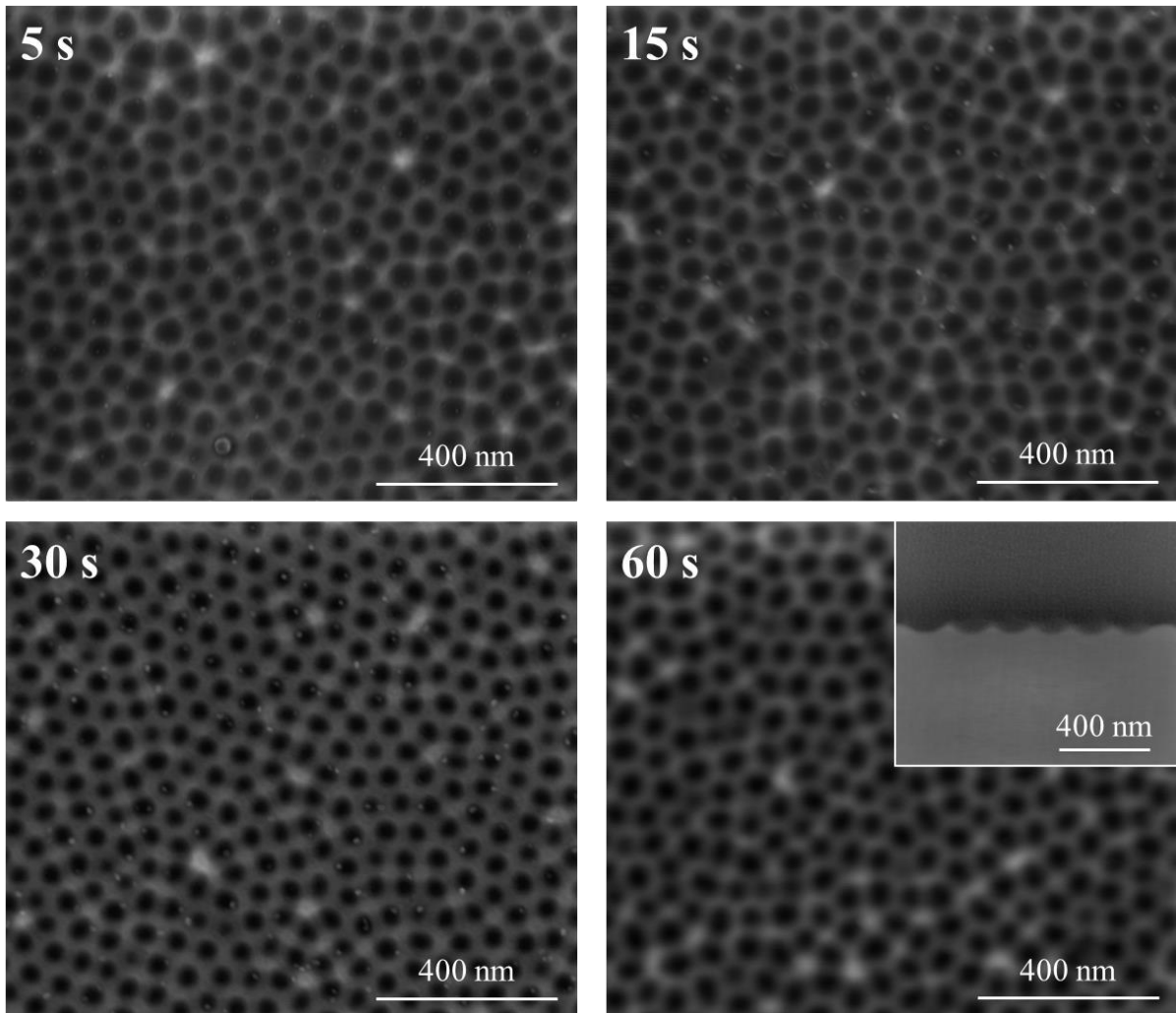
Figure 6.5: SEM images of Ta anodized surfaces with 8:0.25 (vol:vol) of H_2SO_4 : HF, respectively, at room temperature under 25 V as a function of the anodization time (5-60 s).

Unexpectedly, all the anodization times tested lead to a dimple-shaped surface morphology formation (see the cross-section SEM image insert). The literature reports [9] that the use of high H_2SO_4 concentration leads to a more unstable process due to an enhanced oxide dissolution rate by the extremely acid electrolyte. Then, this effect mostly contributes for a dimple topography formation, independently of the anodization runtime, and so explaining the dimple-shaped morphology prevalence observed. However, anodic oxide nanotubes ranging from 1 to 5 μm length are also observed on the samples' surface (see Figure 6.6.a), even though a great part is mainly horizontally aligned and lying over the surface, evidencing its instability.
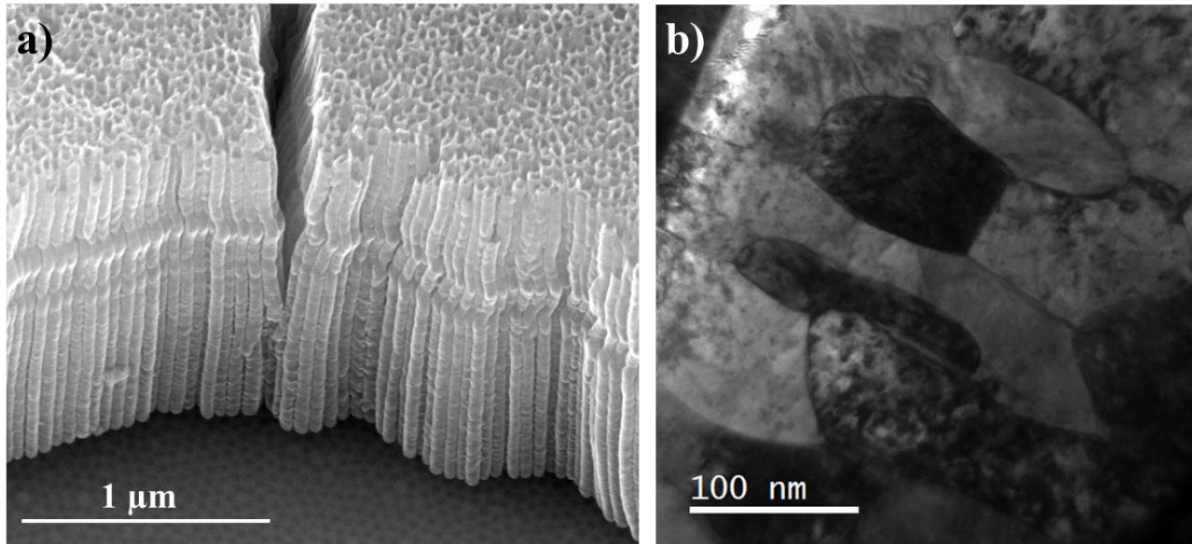
Figure 6.6: (a) Representative TOP view SEM image of the TaO$_x$ anodic nanotubes formed during anodization; (b) Cross-section TEM image of Ta sheet.

TEM observation (Figure 6.6.b) allows to get a Ta sheet cross grain size of about 100 nm, which reveal that it is not easy to relate this dimensions with the nanotubes' instability. It is important to note that, the manufacturing process of Ta sheets englobes a final rolling process, which is responsible for the cross grain size elongation. Despite, some areas are covered with oxide nanotubes patches, rather than a fully nanotubes layer, as observed in Figure 6.7.
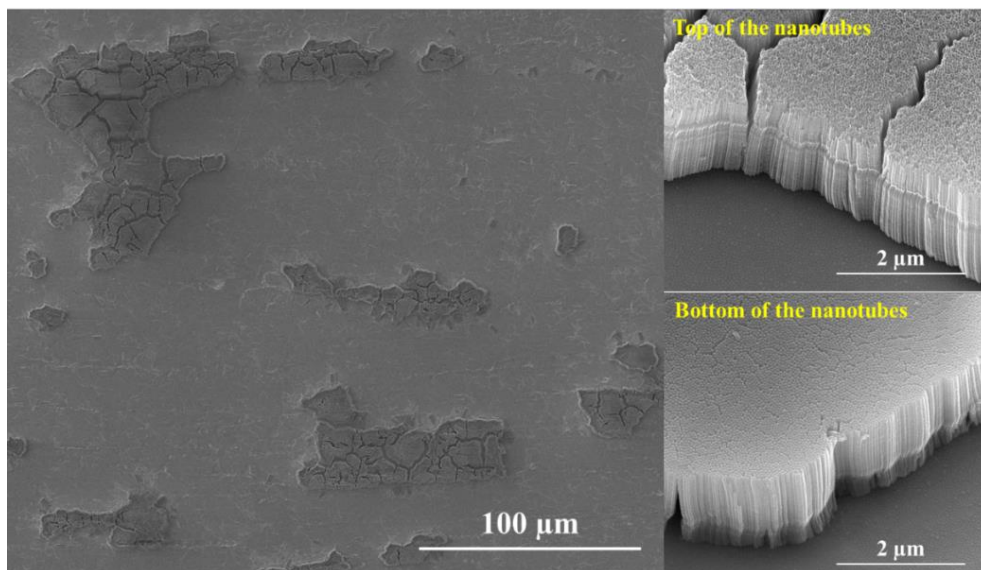
Figure 6.7: Representative TOP view SEM image of the nanotubes patches formed during anodization over Ta surface.

The patches formation can be related with shrinkage effects during the anodic oxide drying after sample withdrawal from the acid electrolyte [9]. Still, the presence of nanotubes patches is not coherent with the cyclic anodization process along the runtime reported in the literature [10] and arise randomly in the anodized surfaces.

On its turn, the presence of different crystallographic orientations in Ta base material may contribute for the appearance of nanostructures patches [1]. On this context, XRD analysis were performed in order to study the influence of sheet orientation on the differentiated dissolution rate. Figure 6.8 present the diffraction patterns for the Ta sheet without anodization, after the acid etching and after acid etching + anodization with 8:0.25 (vol:vol) of H_2SO_4 mixed with HF, respectively, at room temperature under 25 V during 120 s.
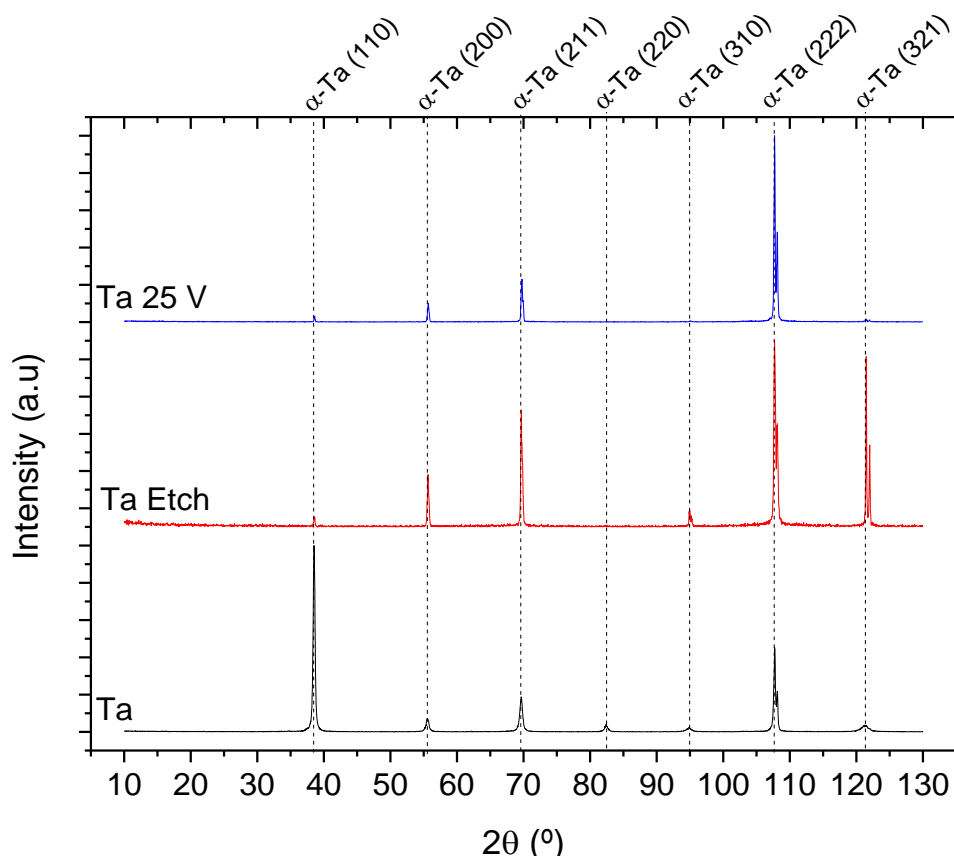
Figure 6.8: Bragg-Brentano XRD pattern of **Ta** sheet, Ta after acid etching (**Ta Etch**) and Ta anodized with 8:0.25 (vol:vol) of H_2SO_4 : HF, respectively, at room temperature under 25 V during 120 s (Ta 25 V).

It can be noticed that before any treatment the base material reveals a preferential orientation in the [110] direction. After acid etching and/or anodization, the [110] direction is consumed and a preferential orientation in the [111] direction arises. Indeed, the low atomic packing for {110} planes allows higher oxidation rate, thus inducing higher dissolution rates, comparing with the {111} planes. Hence, the presence of anodic oxide nanotubes patches, rather than a fully nanotubes layer, may be explained by the differentiated oxidation/dissolution rate induced by the orientally different crystals along Ta sheet. This hypothesis was also assessed by EBSD and is shown in Figure 6.9.
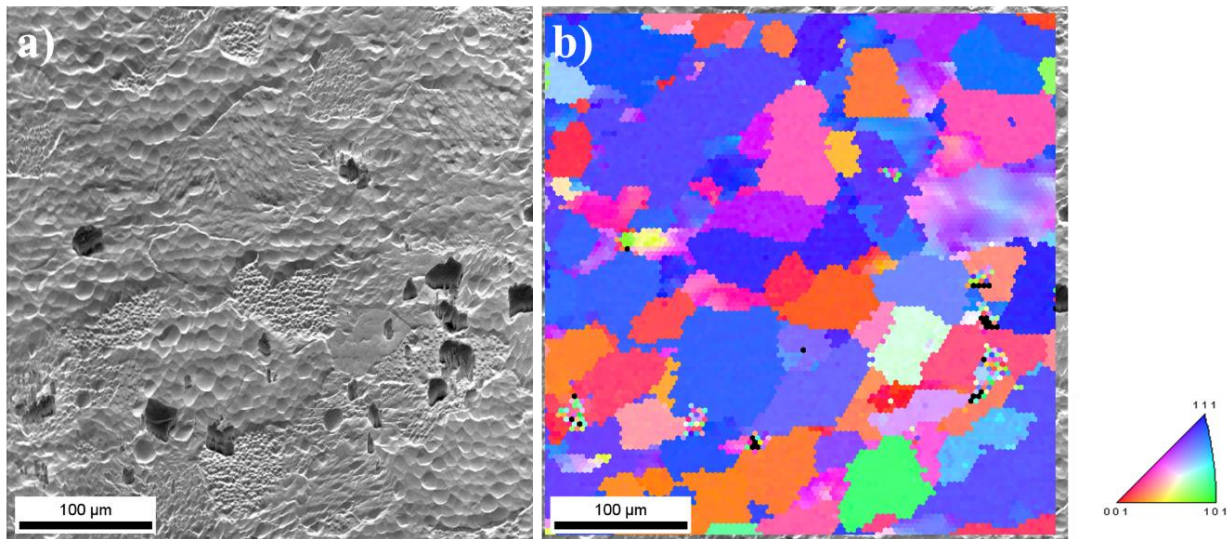
Figure 6.9: (a) TOP view SEM image of an anodized Ta surface after nanotubes patches removal; (b) Corresponding EBSD texturing map of the anodized Ta surface after nanotubes patches removal.

In good agreement with the XRD results, EBSD reveals a preferential orientation along [111] direction reinforcing the theory that [111] direction is more resistant to the oxidation and in some cases its higher resistance may slow down the dissolution rate and promote a higher stability to the nanotubes patches that remains over the anodized surface. In addition, Ta sheet showed a grain size around 70 μm, which is in good agreement with the area of the nanotubes patches presented in Figure 6.7.

6.2. Surface roughness and surface free energy

Similar to the study performed for the surfaces developed by MS, surface roughness and surface free energy were evaluated, using the same commercial control, CP Ti Gr2.

The roughness values obtained from AFM analysis of anodized samples (Ta 25 V and Ta 50 V) and Ta, Ta Etch and CT Ti Gr2 bulk materials are shown in Table 6.2. The acid etching performed to the Ta sheet clearly make the surface smoother causing a decrease in the mean roughness to a half value (from ≈37 nm to ≈15 nm). Likewise, for the sample anodized with 25 V, which revealed a dimple average diameter of 45 nm, the anodization process further causes a electropolishing with a surface smoother of about 12 nm. Still, the decrease of surface roughness is small when compared with the smoothing caused by the acid etching, which is explained by the relatively low applied anodization potential. However, the higher potential promotes an increase of mean roughness up to ≈29 nm and the initial polished finishing is reverted. This behavior is explained by the electrical field increase, which induces a faster dissolution in randomly pits existents on the sample surface increasing the final roughness. CP Ti Gr2 showed a mean roughness around 29 nm. Nevertheless, for all analyzed samples, Rp values demonstrates a good homogeneity of the samples.

Table 6.2: Ra, Rq and Rmax values of CP Ti Gr2, Ta and Ta Etch bulk materials, as well as, Ta 25 V and Ta 50 V anodized samples, measured by AFM and resulting from an average of three different zones

Sample	CP Ti Gr2	Ta	Ta E	Ta 25 V	Ta 50 V
Ra (nm)	29 ± 1.8	37 ± 7.5	15 ± 3.6	12 ± 4.2	29 ± 9.8
Rq (nm)	37 ± 1.6	51 ± 12	19 ± 4.2	17 ± 5.8	36 ± 11
Rmax (nm)	287 ± 5.0	430 ± 63	142 ± 25	218 ± 52	322 ± 17

Additionally, it should be pointed out that the apparent mean roughness differences for CP Ti Gr2 control used in both sets of developed surfaces (MS or anodization) is only an effect of non-homogeneity of the commercial samples, as shown in Figure 6.10.
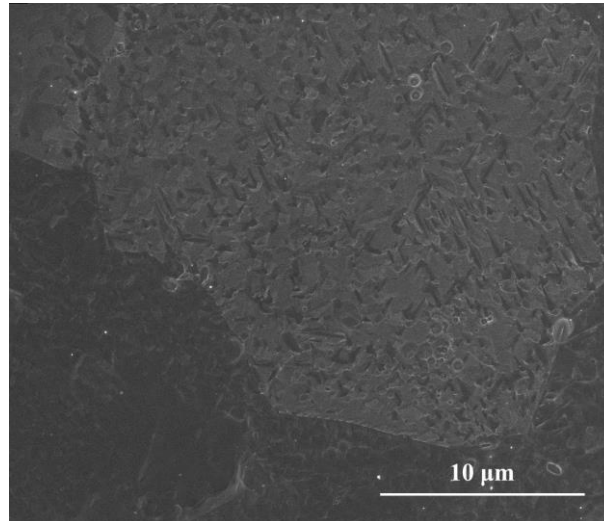
Figure 6.10: TOP view SEM image of the CP Ti Gr2 sample used as commercial control.

The measured contact angle values and the surface free energy of the samples developed by anodization are presented in Table 6.3. To note that in this case, the wetting properties were assessed by measuring the static contact angle with a glycerol instead formamide, which was used in the surfaces developed by MS. Thereafter, the contact angle values and surface free energy cannot be directly compared.

Table 6.3: Milli-q water (θ_w), Glycerol (θ_G) and α-bromonaphtalene ($\theta_{\alpha-B}$) contact angles, surface energy components (apolar Lifshitz–Van der Waals surface free energy component, γ_{LW}; electron acceptor surface free energy component, γ^+; and electron donor surface free energy component, γ^-) and surface free energy of the CP Ti Gr2, Ta, Ta Etch, Ta 25 V and Ta 50 V samples.

Sample	Contact angle ± SD* (°)			Surface energy components (mJ/m^2)			ΔG (mJ/m^2)
	ϑ_w	Θ_G	$\vartheta_{\alpha-B}$	γ^{LW}	γ^+	γ^-	
CP Ti Gr2	87 ± 2.1	76 ± 1.9	29 ± 2.1	39	NA	3.9	NA
Ta	71 ± 2.1	85 ± 2.5	29 ± 2.1	39	NA	30	NA
Ta Etch	68 ± 2.4	68 ± 2.7	32 ± 2.1	38	NA	19	NA
Ta 25 V	90 ± 1.9	80 ± 1.0	34 ± 1.2	37	NA	3.6	NA
Ta 50 V	85 ± 5.5	79 ± 7.0	42 ± 1.1	34	NA	6.4	NA

*Standard Deviation

Regarding the milli-q water results, standard Ta and Ta Etch reveal near water contact angle values, approximately 71° and 68°, respectively, being close of the hydrophobicity limit (65°) [11]. The near contact angle values indicate that the standard sheet is already oxidized (probably passivated) during the manufacturing process and hence, the oxidation promoted by the acid etching does not affect significantly the wettability. When small dimples (≈45 nm) were added to the surface, the water contact angle increase up to 90° and the sample assumes the most hydrophobic character. For higher dimples (≈120 nm) a slightly decrease in the water contact angle is observed (down to 85°). On its turn, CP Ti Gr2 exhibit a contact angle in between the anodized samples.

The literature reports [11] that the influence nanoroughness on the wettability is not clear. However, the marked increase in the contact angle values for the anodized samples, comparing with the standard Ta and Ta Etch, which the surface is chemically oxidized in all cases, reveals that the wettability is mainly regulated by the nanotopography. Generally, it is expected an amplification of the wetting properties with the increase of surface roughness, as described in the Wenzel model. However, Cassie-Baxter described a model considering more complex surfaces where could exist air pockets trapped between the surface gaps [12]. In this model, it is assumed that when the water contacts with a porous surface, the air inside the pore is not expelled out but instead compressed [13]. Hence, the capillarity is the driving force of the wettability behavior. On this context, the presence of dimples on the surface of the anodized samples induces a capillarity effect on the water, which causes an increase on the contact angle. Although, increasing the average diameter of the dimples, as in Ta 50 V sample, the capillarity effect is less intense and thus, the contact angle slightly decreases.

Considering the polar surface energy components (γ^+ and γ^-), for all samples the positive component gives an imaginary number, which according with the Van Oss approach [11] indicates that Glycerol is a non-appropriated liquid to measure the surface free energy properties on these surfaces. Take into consideration that formamide is a liquid not further allowed due to its high toxicity, it was not possible to accurately evaluate the surface free energy of these samples and hence, a correct discussion cannot be done about this issue.

Still, what concerns cell adhesion, it is recognized by the literature that either an oxide [14, 15] or nanoporous [16, 17] surface greatly promotes the interaction between the implant surface and the cells from adjacent tissues. As mentioned, anodization method allowed the formation of an oxide and a nanostructured surface and thus, is expected an enhanced bone-bonding ability for the porous surfaces, despite of the qualitatively hydrophobic character obtained by contact angles measurement.

6.3. Partial conclusions

A nanostructuration of a Ta sheet surface has been performed by anodization process, which dissolution is assisted by electric field. The main idea is to control the nanotopography of the Ta in order to manipulate its bone-bonding ability. HAADF STEM - EDS map analysis reveals a TaO_x layer with a thickness around 5 nm. For all the different parameters used (electrolyte concentration, potential, anodization time) a dimpled topography is achieved. Despite of the HF capacity to dissolve and create anodic oxide nanostructures, there is also a clear dependence on the H_2SO_4 concentration to achieve well-ordered nanostructures. In fact, decreasing both HF or H_2SO_4 concentration (down to 0.125 and 7 vol.%, respectively) a dissolution limit-like of the anodic TaO_x is reached, which compromises the dissolution rate affecting the arrays order, as well as, induces a differential dissolution meaning that in some areas over the surface only occurs the formation of a compact anodic oxide. Unexpectedly, all the anodization times tested lead to a dimple-shaped surface morphology formation. However, oxide nanotubes patches ranging from 1 to 5 µm length, are detected. In fact, the great part of nanotubes is mainly horizontally aligned and lying over the surface, indicating its instability. TEM observation allows to get a Ta sheet cross grain size of about 100 nm, which reveals that it is not easy to relate this dimensions with the nanotubes' instability. XRD and EBSD results indicates that after the electrochemical treatments a preferential orientation of Ta sheet along [111] direction arises. [111] direction demonstrates to have a higher oxidation resistance and hence, in some cases its higher resistance may promote a higher stability to the nanotubes patches that remains over the anodized surface.

The increase of anodization potential/electrical field leads to more differential dissolution, arising a larger dispersion and distribution of average diameters. Varying the anodization potential, it is possible to reach a dimple diameter threshold between 45 and 120 nm.

In what concerns wetting properties, contact angle measurements reveal near water contact angle values for both standard Ta and Ta Etch, approximately 71° and 68°, respectively, being close of the hydrophobicity limit (65°). The Ta 25 V and Ta 50 V dimpled topographies induced an increase in the water contact angle (up to 90° and 85°, respectively) and hence, the samples assumed a qualitatively hydrophobic character. Contrary to the reported in the literature, the topography assumes a predominant feature on the regulation of wettability, instead of the surface chemistry.

6.4. References

[1]   H. El-Sayed, S. Singh, and P. Kruse, "Formation of dimpled tantalum surfaces from electropolishing", *Journal of the Electrochemical Society,* vol. 154, pp. C728-C732, 2007.

[2]   D. Vermilyea, "The formation of anodic oxide films on tantalum in non-aqueous solutions", *Acta Metallurgica,* vol. 2, pp. 482-486, 1954.

[3]   H. El-Sayed, S. Singh, M. T. Greiner, and P. Kruse, "Formation of highly ordered arrays of dimples on tantalum at the nanoscale", *Nano letters,* vol. 6, pp. 2995-2999, 2006.

[4]   J. T. Filho, "Modificação superficial de Titânio para a produção de implantes", Mestrado em Ciências em Engenharia Metalúrgica e de Materiais, Universidade Federal do Rio de Janeiro, Rio de Janeiro, Brasil, 2007.

[5]   L.-N. Wang, M. Jin, Y. Zheng, Y. Guan, X. Lu, and J.-L. Luo, "Nanotubular surface modification of metallic implants via electrochemical anodization technique", *International journal of nanomedicine,* vol. 9, p. 4421, 2014.

[6]   H. A. El-Sayed, H. M. Molero, and V. I. Birss, "The impact of fabrication conditions on the quality of Au nanoparticle arrays on dimpled Ta templates", *Nanotechnology,* vol. 23, p. 435602, 2012.

[7]   A. Ghicov and P. Schmuki, "Self-ordering electrochemistry: a review on growth and functionality of TiO 2 nanotubes and other self-aligned MO x structures", *Chemical Communications,* pp. 2791-2808, 2009.

[8]   N. K. Allam, X. J. Feng, and C. A. Grimes, "Self-assembled fabrication of vertically oriented Ta2O5 nanotube arrays, and membranes thereof, by one-step tantalum anodization", *Chemistry of Materials,* vol. 20, pp. 6477-6481, 2008.

[9]   H. A. El-Sayed and V. I. Birss, "Controlled interconversion of nanoarray of Ta dimples and high aspect ratio Ta oxide nanotubes", *Nano letters,* vol. 9, pp. 1350-1355, 2009.

[10]   H. A. El-Sayed, C. A. Horwood, A. D. Abhayawardhana, and V. I. Birss, "New insights into the initial stages of Ta oxide nanotube formation on polycrystalline Ta electrodes", *Nanoscale,* vol. 5, pp. 1494-1498, 2013.

[11]   C. Van Oss, R. Good, and M. Chaudhury, "The role of van der Waals forces and hydrogen bonds in "hydrophobic interactions" between biopolymers and low energy surfaces", *Journal of colloid and Interface Science,* vol. 111, pp. 378-390, 1986.

[12]   S. Rodrigues, C. A. Alves, A. Cavaleiro, and S. Carvalho, "Water and oil wettability of anodized 6016 aluminum alloy surface", *Applied surface science,* 2017.

[13]   T. Fujii, H. Sato, E. Tsuji, Y. Aoki, and H. Habazaki, "Important role of nanopore morphology in superoleophobic hierarchical surfaces", *The Journal of Physical Chemistry C,* vol. 116, pp. 23308-23314, 2012.

[14]   T. Miyazaki, H.-M. Kim, T. Kokubo, C. Ohtsuki, H. Kato, and T. Nakamura, "Mechanism of bonelike apatite formation on bioactive tantalum metal in a simulated body fluid", *Biomaterials,* vol. 23, pp. 827-832, 2002.

[15]   B. R. Levine, S. Sporer, R. A. Poggie, C. J. Della Valle, and J. J. Jacobs, "Experimental and clinical performance of porous tantalum in orthopedic surgery", *Biomaterials,* vol. 27, pp. 4671-4681, 2006.

[16]   S. Lavenus, J. Rozé, A. Hoornaert, G. Louarn, and P. Layrolle, "Chapter 5 - Impact of Nanotechnology on Dental Implants," in *Emerging Nanotechnologies in Dentistry*, K. Subramani and W. Ahmed, Eds., ed Boston: William Andrew Publishing, 2012, pp. 71-84.

[17]   K. Subramani, D. Tran, and K. Nguyen, "Chapter 8—Cellular Responses to Nanoscale Surface Modifications of Titanium Implants for Dentistry and Bone Tissue Engineering Applications", *Emerging Nanotechnologies in Dentistry, William Andrew Publishing, Boston, MA,* pp. 113-136, 2012.

Final remarks and future research

In this work $Ta_{1-x}O_x$ with different oxygen content were successfully deposited by reactive magnetron sputtering in an $Ar + O_2$ atmosphere. Briefly, the samples are basically a metallic-like film with incorporation of small amounts of oxygen when deposited in metallic mode. When the threshold of the reactive mode is approaching, namely on higher deposition rates, the target becomes partially oxidized and can be observed the formation of nanocrystalline oxides. When the "poisoned" regime is achieved, the Ta target cannot accommodate more O and the sputtering changes. The deposition rate drastically decreases, as well as, the deposition temperature decreases the adatom mobility, reaching the deposition of amorphous oxides.

More specifically, the increase in the oxygen amount retrieved more compact and smoother $Ta_{1-x}O_x$ coatings. Likewise, structural results showed an unusual bcc α-Ta phase in the non-reactive Ta coating; transitioning to a mixture of nanocrystalline phases for low oxygen contents; achieving oxide phases with large amounts of oxygen. Further, although not observed in XRD, for the coatings deposited close to the reactive mode threshold IR showed absorption bands corresponding to amorphous phase containing some crystals embedded, while for the coatings deposited in the poisoned regime the IR suggested a marked amorphous nature. Refractive index varies between 2.09 and 2.27, within the range reported for Ta_2O_5 thin films. The changes in refractive index are correlated with the different crystallinity of the coatings, which is corroborated with the IR results.

Indeed, all $Ta_{1-x}O_x$ phases have structural similarities since they are formed by the distortion of the Ta base structure, and therefore a clear and unequivocal identification of the crystalline phases is not trivial. In this sense elastic properties determination by SAW and supported by theoretical studies were the key role for better understanding of the evolution of the coatings crystal-structure. For TO1 (11 at.%), when the oxygen was

added, *DFT* calculations show that the remarkably stable Ta_4O structure may be seen as a bcc Ta with oxygen atoms in interstitial positions that also forms a tetragonal phase, which might be mistaken as a pure β-Ta phase by XRD. Furthermore, *ab-initio* calculations of different Ta-O phases are in good agreement with the experimental results and revealed that an increase of oxygen to the Ta phase leads to the distortion of Ta crystal structure, causing a decrease in its density and an increase in the elastic constants.

Biocorrosion validation of the developed coatings was assessed by surfaces exposure to artificial saliva. All coatings evidenced a protective behavior of the films for polarization induced corrosion of SS 316L, matching the performance of the CP Ti Gr2. Yet, TO6 coating exhibited the best corrosion performance due to the lower electrochemical activity. The *in-vitro* bone-bonding ability of the studied materials, by immersion of the samples in Simulated Body Fluid (SBF) were performed. The non-reactive Ta coating presented the most hydrophobic character (100°); with increasing oxygen amount contact angles progressively decrease, down to the lowest measured value, 63°. The higher wettability was also accompanied by an increase on the surface energy. Bioactivity tests demonstrates that highest O-content coating, in good agreement with wettability and surface energy values, showed an increased affinity for apatite adhesion, with higher apatite content formation, when compared to the bare Ti substrates.

Electrochemical anodization by dissolution assisted by electric field anodization was successfully performed to prepare anodic TaO_x nanostructures. Generally, a dimple-shaped surface morphology was main topography reached, exhibiting a thickness around 5 nm. Despite of the HF capacity to dissolve and create anodic oxide nanostructures, there is also a clear dependence on the H_2SO_4 concentration to achieve well-ordered nanostructures. In fact, decreasing both HF or H_2SO_4 concentration (down to 0.125 and 7 vol.%, respectively) the arrays order quality was compromised, as well as, the dissolution rate drops down and some areas over the surface only exhibit the formation of a compact anodic oxide. Still, unstable oxide nanotubes patches were detected. The analysis of XRD and EBSD results indicates that [111] direction of Ta sheet is more resistant to the oxidation and thus, may promote a higher stability to the nanotubes patches that remained over the anodized surface. Therefore, more intensive research is required to

better understand and optimize the cyclic mechanism of nanostructures formation and hence, stabilize different types of nanostructures.

In summary, despite of globally match the performance of the market reference, $Ta_{1-x}O_x$ surfaces demonstrated to be bioactive proving that their surface chemical composition greatly promotes the bone-bonding ability. So far, it was not possible to confirm that nanotopography can further enhance the osseointegration. But knowing that nanostructures biomimetize the bone tissue, and considering the very promising results achieved, potentially interesting for the industry, a patent application was done with the reference number of PCT/IB2015/057171.

Therefore, a detailed study with a complete biological focus is proposed, in order to better understand the influence of different topographies on the osseointegration and its enhancement, as well as, to test its biocompatibility. Also, tribo-corrosion tests should be performed to evaluate the friction and wear behaviors of the optimized surfaces in a tribological contact under aggressive oral environments.

After a more detailed biological response study, sample exhibiting the best compromise between osseointegration and tribo-corrosion must be tested in conditions that mimic the dental implants, by producing prototypes. Finally, if positive results are observed in terms of biological performance and specialized tribo-corrosion test, an *in vivo* approach should be pursued.

Cristiana Filipa Almeida Alves

Annex

Annex I: Stainless steel 316L composition

Chemical composition (wt.%)

AISI SS 316L		
	Fe	66.16
	Cr	17.98
	Ni	11
	Mo	2.49
	C	0.022
	Mn	1.1
	P	0.013
	S	0.006
	Si	0.9

Annex II: Equations used for elastic constant calculations

The calculation of elastic moduli (the bulk, shear modulus) was done using the Voigt [1] and Reuss [2] averaging procedures which are expressed in terms of the stiffness constants, cij, and compliances sij, respectively. In particular, the bulk and shear modulus in the Voigt approach are:

$$B_V = \frac{1}{9}[(c_{11} + c_{22} + c_{33}) + 2(c_{12} + c_{13} + c_{23})]$$

$$G_V = \frac{1}{15}[(c_{11} + c_{22} + c_{33}) - (c_{12} + c_{13} + c_{23}) + 3(c_{44} + c_{55} + c_{66})]$$

The corresponding expressions for the Reuss averaging are:

$$B_R = [(s_{11} + s_{22} + s_{33}) + 2(s_{12} + s_{13} + s_{23})]^{-1}$$

$$G_R = 15[4(s_{11} + s_{22} + s_{33}) - (s_{12} + s_{13} + s_{23}) + 3(s_{44} + s_{55} + s_{66})]^{-1}$$

The elastic modulus, E, and Poisson ratio, ν, was obtained using the average values of Voigt and Reuss values:

$$E = \frac{9BG}{3B + G}$$

$$v = \frac{3B - 2G}{2(3B + G)}$$

It is also interesting to calculate the elastic's modulus along the three major crystallographic orientations (100, 110, 111) for structures exhibiting a high degree of crystal anisotropy, as follows:

$$E_{100} = c_{11} - 2\frac{c_{12}{}^2}{c_{11} + c_{12}}$$

$$E_{110} = 4\frac{(c_{11}{}^2 + c_{11}c_{12} - 2c_{12}{}^2)c_{44}}{2c_{11}c_{44} + c_{11}{}^2 + c_{11}c_{12} - 2c_{12}{}^2}$$

$$E_{111} = 3\frac{(c_{11} + 2c_{12})c_{44}}{c_{44} + c_{11} + 2c_{12}}$$

[1]   W. Voigt, "Lehrbuch der Kristallphysik (Leipzig: B. G. Teubner)", ed: Phys, 1928.
[2]   A. Reuss, "Berechnung der fließgrenze von mischkristallen auf grund der plastizitätsbedingung für einkristalle", *ZAMM-Journal of Applied Mathematics and Mechanics/Zeitschrift für Angewandte Mathematik und Mechanik,* vol. 9, pp. 49-58, 1929.

Anexx III: Simulated body fluid (SBF) composition

SBF chemical composition (pH: 7.25; 1L)

Compound	Quantity (g)
NaCl	7.996
NaHCO$_3$	0.350
KCl	0.224
K$_2$HPO$_4$.3H$_2$O	0.228
MgCl$_2$.6H$_2$O	0.305
1kmol/cm^3 HCl	40 cm^3
CaCl$_2$	0.278
Na$_2$SO$_4$	0.071
(Ch$_2$OH)$_3$CNH$_2$	6.057

Annex IV: Ta sheet chemical composition

	Chemical composition (ppm)	
Ta sheet	Fe	4.3
	Mo	10
	Nb	150
	Ni	40
	Si	10
	Ti	1.1
	W	29
	Zr	1.2
	C	10
	N	40
	O	79
	H	6

Anexx V: ICDD cards

Ta

Tantalum

2th	i	h	k	l
38.473	100	1	1	0
55.550	21	2	0	0
69.583	38	2	1	1
82.464	13	2	2	0
94.939	19	3	1	0
107.644	7	2	2	2
121.354	29	3	2	1
137.498	4	4	0	0

Lattice : Body-centered cubic

S.G. : Im-3m (229)

a = 3.30580

Z = 2

Mol. weight = 180.95

Volume [CD] = 36.13

Dx = 16.634

I/Icor = 4.44

Analysis: Spectroscopic analysis shows faint traces of Nb, Al, Si, Fe, Mn. Color: Gray. Sample Preparation: The material contained dissolved gases which caused broadening of diffraction peaks, and TaH, which contributed extra reflections. After annealing at 1500 C in vacuum for 30 minutes in a tantalum boat, the sample gave very sharp reflections including only traces of the hydride. Sample Source or Locality: Sample procured from Johnson Matthey Company, Ltd., London, England, UK. Temperature of Data Collection: Pattern taken at 299 K. Unit Cell Data Source: Powder Diffraction.
Data collection flag: Ambient.

Swanson, Tatge., Natl. Bur. Stand. (U.S.), Circ. 539, volume I, page 29 (1953)

CAS Number: 7440-25-7

Radiation : CuKα1

Lambda : 1.54050

SS/FOM : F8=110(0.0090,8)

Filter : Beta

d-sp : Not given

Ta

Tantalum
Also called: β-Ta

Lattice : Tetragonal

S.G. : P42/mnm (136)

a = 10.19400

c = 5.31300

Z = 30

Mol. weight = 180.95

Volume [CD] = 552.11

Dx = 16.326

Dm = 16.100

Additional Patterns: To replace 00-019-1290. Sample Preparation: Prepared as a single phase by electro-deposition from molten fluoride bath at 800 C. Unit Cell Data Source: Powder Diffraction.
Data collection flag: Ambient.

Moseley, Seabrook., Acta Crystallogr., Sec. B, volume 29, page 1170 (1973)

CAS Number: 7440-25-7

Radiation : CuKα1

Lambda : 1.54056

SS/FOM : F30= 6(0.0761,67)

Filter :

d-sp : Guinier

2th	i	h	k	l
18.785	4	1	0	1
20.786	1	1	1	1
27.681	1	3	1	0
29.889	1	2	2	1
32.388	8	3	1	1
33.692	40	0	0	2
34.785	1	4	0	0
36.282	80	4	1	0
37.393	55	3	3	0
38.201	55	2	0	2
39.241	80	2	1	2
40.209	100	4	1	1
41.187	65	3	3	1
44.052	18	3	1	2
45.187	1	5	1	0
46.815	4	3	2	2
47.622	5	5	0	1
48.514	6	5	1	1
49.440	1	4	0	2
51.100	1	5	2	1
56.783	4	4	3	2
57.559	5	6	1	1
59.388	1	3	1	3
59.854	12	6	2	1
60.546	1	5	4	1
63.590	30	6	3	1
64.678	45	4	1	3
64.982	1	6	0	2
65.341	1	3	3	3
65.755	1	6	1	2
66.710	30	7	2	0
67.143	1	7	1	1
67.973	1	6	2	2
68.596	1	6	4	1
71.031	25	5	1	3
72.224	1	1	1	4
74.817	1	6	5	1
77.030	20	8	2	0
79.551	16	8	2	1

Pattern : 03-065-6450	Radiation = 1.540600	Quality : Indexed

Ta₄O

Tantalum Oxide
Also called: β-Ta4 O

Lattice : Orthorhombic	**Mol. weight =** 739.79
S.G. : Pmmm (47)	**Volume [CD] =** 75.28
a = 7.19400	**Dx =** 16.318
b = 3.26600	
c = 3.20400	
a/b = 2.20269 **Z =** 1	**I/Icor =** 9.36
c/b = 0.98102	

NIST M&A collection code: L 50072 ST447   1. Sample Preparation: Tantalum metal powder or tantalum hydride was oxidized with stream in great excess at temperatures varying between 873K and 1173K, and for periods between one hour and about two days. Temperature Factor: TF was not given, B set to 1.000 for calc. Minor Warning: No e.s.d reported/abstracted on the cell dimension. No Rfactor reported/abstracted. Unit Cell Data Source: Powder Diffraction.
Data collection flag: Ambient.

Calculated from NIST using POWD-12++
Schonberg, N., Acta Chem. Scand., volume 8, page 240 (1954)

Radiation : CuKα1	**Filter :**
Lambda : 1.54060	**d-sp :** Calculated spacings
SS/FOM : F30=179(0.0040,35)	

2th	i	h	k	l
12.293	26	1	0	0
24.731	5	2	0	0
27.284	1	0	1	0
27.822	1	0	0	1
30.024	5	1	1	0
30.518	5	1	0	1
37.153	999	2	1	0
37.564	988	2	0	1
39.363	964	0	1	1
41.391	5	1	1	1
46.971	33	3	1	0
*46.971	33	2	1	1
47.310	32	3	0	1
50.720	170	4	0	0
55.475	35	3	1	1
56.291	142	0	2	0
57.480	131	0	0	2
58.543	2	4	1	0
58.834	2	4	0	1
59.025	1	1	0	2
62.402	1	2	2	0
63.521	1	2	0	2
63.935	1	0	2	1
64.739	9	5	0	0
*64.739	9	0	1	2
65.390	2	1	2	1
66.030	254	4	1	1
66.209	134	1	1	2
69.656	224	3	2	0
*69.656	224	2	2	1
70.450	214	2	1	2
70.657	119	3	0	2
71.610	13	5	1	0
71.872	15	5	0	1
76.526	10	3	2	1
77.293	10	3	1	2
78.469	18	5	1	1
79.158	64	4	2	0
80.171	62	4	0	2
84.688	61	0	2	2
85.843	1	4	2	1
86.373	34	6	1	0
86.622	49	4	1	2
*86.622	49	6	0	1
89.951	1	2	2	2
91.047	5	5	2	0
91.388	3	1	3	0
92.044	5	5	0	2
92.316	3	0	0	3
93.001	4	6	1	1
93.632	1	1	0	3
95.337	37	2	3	0
96.534	8	3	2	2
96.713	41	0	3	1
97.099	23	7	0	0
97.594	37	2	0	3
*97.594	37	5	2	1
98.448	10	5	1	2
98.724	40	0	1	3
100.055	1	1	1	3
101.985	2	3	3	0
*101.985	2	2	3	1
103.582	7	7	1	0
103.838	8	7	0	1
104.288	4	3	0	3
105.921	52	4	2	2
106.732	2	6	0	2
108.860	3	3	3	1
110.514	12	7	1	1
110.980	8	3	1	3
111.603	1	4	3	0
112.712	33	6	2	1
113.525	33	6	1	2
114.035	17	4	0	3
117.874	6	8	0	0
118.932	44	0	2	3
*118.932	44	4	3	1
120.555	1	1	2	3
121.235	42	4	1	3
123.739	45	2	3	2

2th	i	h	k	l
124.653	7	7	2	0
125.251	47	2	2	3
*125.251	47	8	1	0
125.873	26	7	0	2
*125.873	26	8	0	1
127.856	3	5	0	3
132.072	3	3	3	2
133.173	10	7	2	1
133.979	23	8	1	1
134.206	13	7	1	2
136.463	5	5	1	3
137.131	4	6	2	2
141.267	11	0	4	0
143.418	1	1	4	0
145.769	13	6	3	0
148.171	11	0	0	4
149.021	7	9	0	0
149.986	14	6	0	3